Dario W. Knebl

DOCTORAL THESIS

For obtaining the academic degree of

Doktor der Naturwissenschaften

Simulation of Gap Plasmonics

Supervisor: Ao.Univ.-Prof. Mag. Dr. Ulrich Hohenester

University of Graz

Institute of Physics

Department of Theoretical Physics

Graz, 2017

Abstract

A surface plasmon is a coherent electron oscillation which can be excited at the surface of a metallic nanoparticle, either optically or by an electron beam located in close proximity to the particle. By placing two nanoparticles a few nanometers apart from each other, the surface plasmon modes of the individual particles hybridize and the modes of the coupled nanoparticles strongly differ from those of the individual particles.

This thesis deals with investigations on sub-nanometer gaps of metallic dimers where quantum effects such as electron tunneling enable a new type of plasmon resonance, a tunneling electron transfer plasmon. We are especially interested in coupled silver nanocubes and on their tunneling electron transfer plasmons. Further, by inserting a self-assembled-molecule-monolayer in the gap region, we compare our results with experimental results from literature. This led to further investigations of the morphology of the gap interface where a continuous geometric transformation from nanospheres to nanocubes shows that the tunneling electron transfer plasmon shifts from low resonance-energies in the case of nanospheres to higher resonance-energies in the case of nanocubes.

An ab-initio transport theory method is applied to calculate the transmission function as well as the electric conductivity of the gap of the dimer. Additionally a method combining linear response and time dependent current-density functional theory is used for one-dimensional simulations concerning coupled nanoparticles.

Kurzzusammenfassung

Ein Oberflächen-Plasmon ist eine kohärente Elektronenoszillation, die entweder optisch oder durch einen Elektronenstrahl an der Oberfläche eines metallischen Nanoteilchens angeregt werden kann. Bei einem System aus zwei Nanoteilchen, welche nur wenige Nanometer voneinander entfernt sind, vermischen sich die Plasmon-Moden der einzelnen Nanoteilchen zu neuen sogenannten hybridisierten Moden. Diese Moden unterscheiden sich stark von den Moden der einzelnen Nanoteilchen.

In dieser Dissertation untersuchen wir gekoppelte metallische Nanoteilchen deren Abstand weniger als ein Nanometer beträgt. Bei derartig kleinen Abständen kommen quantenmechanische Effekte wie der elektronische Tunneleffekt zum tragen und es erscheinen neue Typen von Plasmonen, die Tunnelplasmonen. Speziell untersuchen wir gekoppelte Silber-Nanowürfel und deren Tunnelplasmonen. Um die Ergebnisse mit bereits dokumentierten Experimenten vergleichen zu können haben wir auch gekoppelte Nanoteilchen untersucht, zwischen denen wir eine Molekül-Monolage eingefügt haben. Bereits gut untersucht sind gekoppelte metallische Nanokugeln. Dies machen wir uns zunutze und verformen die gekoppelten Nanokugeln mittels einer kontinuierlichen morphologischen Transformation zu Nanowürfeln. Dabei zeigt es sich, dass die plasmonischen Tunnelmoden der gekoppelten Silber-Nanokugeln kleinere Resonanzenergien vorweisen als die von gekoppelten Silber-Nanowürfeln.

Um einen anderen Zugang zur Untersuchung von Tunnelplasmonen zu erreichen, kombinieren wir Linear Response mit Time Dependent Current-Density Functional Theory.

Contents

Contents

1. Introduction

Matter that we experience in our daily life is build up of atoms and molecules. An essential role plays the electron which is an elementary particle and one of the few basic components of matter in an atomistic level. Combining just different numbers of the basic components results in a big amount of different materials. The existence of many of these different materials with many different properties will lead us to concentrate on a specific type of materials - conductors. It is quite simple: Conductors are able to conduct electric current, i.e. not all electrons inside a conductor are locally confined which enables electron transport through the material. This means that a major role of this characteristic is played by the unbound electrons of a conductor. These electrons are not bound to a certain atom or molecule, they are bound to the conductor only. Getting now more into solid state science: For such (free) electrons the term 'electron gas' has been used for many years.[1]

What if something can force these (free) electrons to move to a certain direction? Since electrons possesses a charge unequal zero, it should be obvious that we are searching a force which is sensitive to charges. Hence, the basic interaction we deal with is the electromagnetic force. The origin of the electromagnetic force is simple: Repulsion by equal charges and attraction by different charges. It is astonishing how much work has already been done and how much effort has been taken for investigating systems based on that simple interaction, but the complexity lies not in the pure interaction, the complexity lies in the huge number of interacting particles (e.g. electrons), all interacting with each other. Just to mention, the number of atoms in a macroscopic particle can be estimated and determined by the Avogadro constant $N_A \approx 6.022 \cdot 10^{23}$. Each atom of a noble metal contains at least one electron that contributes to the electron gas of the metal. So most effects concerning electromagnetic interaction are generated by a huge number of interacting electrons. This applies also for plasmons.

In physics one often prefers to use the concepts of fields rather than forces. It is more general and sometimes easier to handle. In other words, if a force is acting on an electron, one can use a corresponding field instead, describing the same action. When a constant external[2] electromagnetic field is present, the electrons of the electron gas start to accelerate in a preferred direction depending on the field. Next, consider an external field consisting of sinusoidal electric and magnetic components, e.g. light. Now one could think that if one applies an external oscillating field on any conducting structure the electron gas will be forced to an oscillating behavior. But it is not that easy. One has to mention the existence of the (effective) mass inertia of each electron, which leads to a delay of the interaction. Furthermore, the geometries of the solid conductor can lead to reflections of electron motions. Also, the number of electrons will influence the behavior of the electron gas when an external oscillating field is applied. In total these and even more facts, e.g. screening effects, result that only for specific frequencies of the external field a similar

---

[1] An electron gas is similar to a box filled with classical gas: the gas particles are not confined to a certain position in the box, but they are constrained to stay within the box.

[2] External means that the origin of the force comes from outside and not from any of the particles (electrons) within the considered system.

oscillation can be induced to the electron gas. One says that at such frequencies the system is in resonance with the external field. All possible resonances of a conducting structure are determined by its geometric and material parameters.

> **Plasmon**
> A plasmon is a collective charge oscillation of electrons that can occur on the surface or in the bulk region of a conductor (surrounded by a dielectric) [1–5].

During the last decades it has become possible to investigate plasmon resonances at metallic nanoparticles, both, theoretically and experimentally. A brief overview on that is given in the list below in the section 'History of Plasmonics'.

Of great interest, especially concerning this thesis, are metallic dimers. A **dimer** is a two-particle system, each particle having the same shape and consisting of the same material. Imagine having a single particle which is excited by an external source of light. When bringing this particle and a second particle of the same shape and same material slowly together, then some of the physical quantities will start to change, some slightly, some dramatically. The separation between both particles is called gap. In the last decade recent works have demonstrated that the plasmonic behavior of a dimer starts to deviate from that of a single particle, when the gap-width is approximately a few nanometers small or even smaller [6–9].

In order to perform such experiments, dimers fits to be the best system for that, since it is easier to separate coupling effects from those of the corresponding single particle. Another benefit of dimers are that the investigated system can be kept as simple as possible. In this thesis dimers consisting of noble metals, e.g. silver or gold, which are separated by dielectrics, e.g. air or vacuum, are investigated.

1.1. History of Plasmonics

Here a brief overview of selected milestones in plasmonics is given. The following list is mainly taken from of Kik's 'Surface Plasmon Nanophotonics' [10].

4th century The Lycurgus cup, a Roman cup made of glass containing gold and silver nanoparticles, can show two different colors depending whether light passes the glass or is reflected (see Fig. 1.1). The effects are due to plasmonic resonances.

1902 A feature, known as Wood's Anomaly, which could not be explained has been observed at an optical reflection experiment with metal gratings by Robert W. Wood [11].

1904 The bright colors of metal doped glasses has been theoretically described using the Drude theory by Maxwell Garnett [12].

1908 Development of the Mie-Theory by Gustav Mie [13].

1956 First theoretical description of electron energy loss by David Pines [14]. He has introduced the term 'plasmon'.

1957 The existence of plasmons near metal surfaces has been showed by Rufus Ritchie [15].

1968 The unexplained feature of optical reflections at metal gratings could be described by Ritchie et. al. [16]

1968 New methods in order to excite surface plasmons optically on metal films has been implemented by Kretschmann, Otto, and Raether [17, 18].

1970 Description of the optical properties of metallic nanoparticles using the concept of surface plasmons by Uwe Kreibig and Peter Zacharias [19].

1974 The term 'surface-plasmon-polariton' has been introduced by Stephen Cunningham [20].

1974 Observation of Surface Enhanced Raman Scattering by Martin Fleischmann et. al. [21]

1991 Development of a commercial sensor using surface plasmons.

1997 The prediction of optical beams guiding in metallic nanowires by Junichi Takahara et. al. [22]

1998 Observation of anomalous transmission of light through metallic subwavelength apertures by Thomas Ebbesen et. al. [23]

2000 Suggestion by John Pendry that a thin metal film could represent a 'perfect lens'. [24]

In the last decade the field of plasmonics has spread to different disciplines such as chemistry, biology, biotechnology, biomedicine and material science [25].

Figure 1.1.: The Lycurgus cup [26]. When light is reflected from the outer side of the cup, the cup shines green (left). When light transmits from the inside of the cup to the outside, the cup shines red (right).

1.2. Future of Plasmonics

When talking about future in science concerning solid state physics one often drifts to talk rather about future applications than about theory. There are ideas which reach from highly speculative applications, such as treating cancer by the use of nanoparticles, to increasing the efficiency of photo-voltaic cells [27] and many other ideas.

1.3. Motivation of this Thesis

So far by now, a vague picture of plasmonics has been presented. Based on the fact that plasmonic resonances exist in the nanometer scale, not exceeding the micrometer range, a question could arise about the influence of quantum mechanics to plasmonics. Plasmonics is usually well-described by classical electrodynamics. In classical electrodynamics a solid conductors surface is clearly defined. A valence electron can only stay inside the conductor and may not leave it. In quantum mechanics the probability of finding a valence electron outside the conductor must not be zero, it decays exponentially apart the conductor. What if two conductors are placed close to each other with a gap of a few nanometers or less? In classical electrodynamics it is not possible that any electron can leave one conductor and enter the other one if both are separated by a dielectric and an external field is applied. In contrast, in quantum mechanics it is possible, where the corresponding probability depends on the gap width, on the conductor material and on the external field.

Several recent publications [6–9] deal with sub-nanometer gaps at plasmonic metallic nanoparticles. They have showed that for such small gaps a description using classical electrodynamics only is not valid. A non-local behavior of the metallic electron gas in the gap region appears which can be explained by quantum mechanics in terms of electron tunneling.

In the work of the group of Baumberg [6] two atomic force microscope (AFM) Au-coated tips are positioned nanometers apart. While the system is excited by laser light, a bias is applied on the tips in order to force a possible tunneling current between the two tips. The spectra for different separation distances of the tips reveal the existence of a new type of plasmonic resonance, a tunneling charge plasmon resonance. A sketch of the experimental setup and the spectra are shown in Fig. 1.2. The two tips can be approximately viewed as two coupled nanospheres.

In the work of Ciraci et. al. [7] an only few Ångström thick non-metallic film spaces a gold film from gold nanospheres. In Fig. 1.3 the schematic setup, a cross section of it and a comparison of the measured data with numerical simulated theories is plotted. The outcome is, that the 'local' theory which is given by a classical theory starts to deviate from the experimental data for a spacer layer thickness below 1 nm. In contrast the 'non-local' theory, for which a semi-classical hydrodynamic model is taken, is in good agreement with the experiment overall.

The group of Dionne [8] placed silver nanospheres with a diameter of 10 nm on a substrate where they investigated situations of two coupled nanospheres. For separation distances above 0.5 nm their EELS measurements are in a good agreement with simulations. For separation distances below 0.5 nm they observed a reduced intensity of the dipole peak in the EELS spectra which is not explainable with classical theories. In order to describe this feature quantum mechanics is needed which brings up electron tunneling. The left plot of Fig. 1.4 shows a density plot of two coupled silver nanospheres for different separation distances. Negative distances represent overlapping spheres. The red-shifting bonding dipole plasmon (BDP) disappears for negative distance values. Instead, a different mode appears, the so-called charge transfer plasmon (CTP) mode, where electron charges are transported between both particles.

1.4. Structure of this Thesis

This thesis is divided into three main parts, **Electrodynamic Simulations, DFT Simulations** and **Quantum Tunneling**, where each main part is sub-divided into two chapters - theory and results.

In the first chapter **Introduction** the term 'plasmon' is introduced, a brief overview of important historical milestones in the research field of plasmonics is given and a few
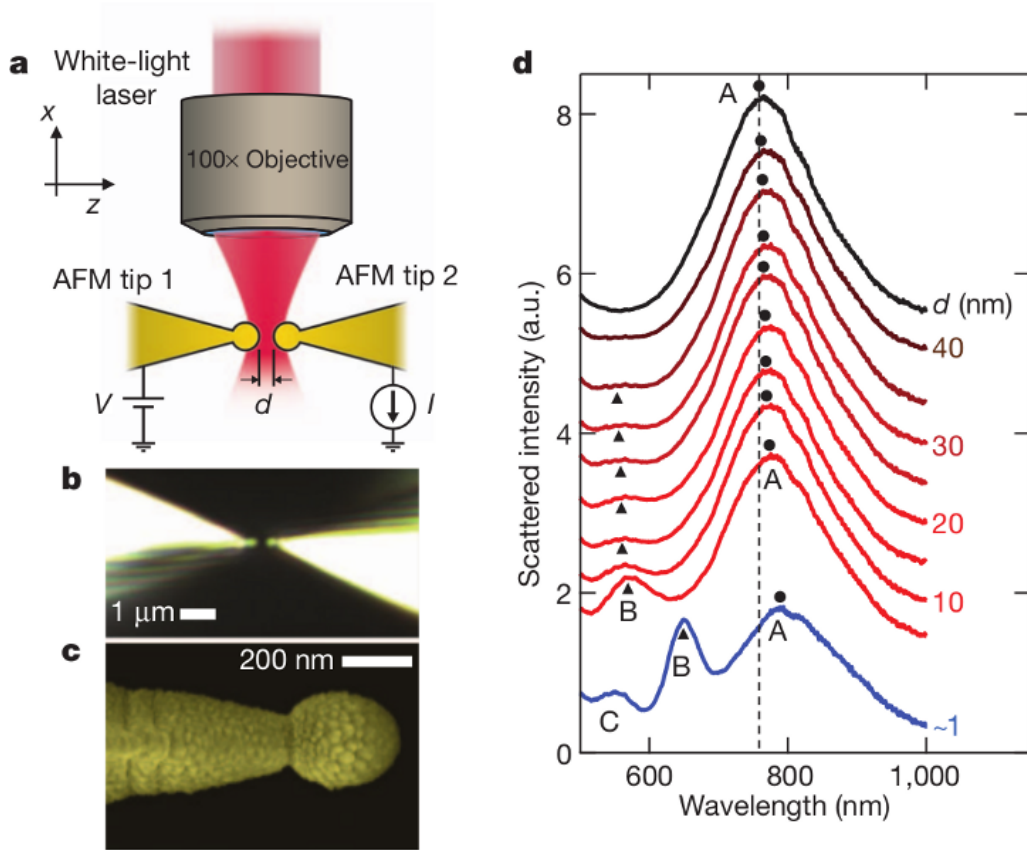
Figure 1.2.: Graphic taken from [6]. (a) Schematic experimental setup and (b) dark-field microscope image of tips. (c) Scanning electron microscope image of one tip and (d) dark field scattering spectra of two approaching Au-coated AFM tips.

selected works are brought up for motivating the topic of this thesis.

The chapter **Electrodynamic Simulations - Gap Plasmonics - Theory** introduces the basic concepts and theories on which the electrodynamic simulations of this thesis relies on. It concerns classical electrodynamics, the boundary element method, the quantum corrected model and other. In the chapter **Electrodynamic Simulations - Gap Plasmonics - Results** the outcome of the performed simulations concerning the previous theories are presented.

In the chapter **DFT Simulations - Molecular Tunnel Junction - Theory** the density functional theory and a Greens function transport theory. In the chapter **DFT Simulations - Molecular Tunnel Junction - Results** outcomes and results of electron transport through molecules inbetween noble metals are presented.

The third main part starts with chapter **Quantum Tunneling - Theory** where time-dependend current-density functional theory (TDCDFT) and linear response (LR) theory is combined in order to describe quantum tunneling from first principles. In the chapter **Quantum Tunneling - Results** outcomes of the application of LR-TDCDFT are shown.
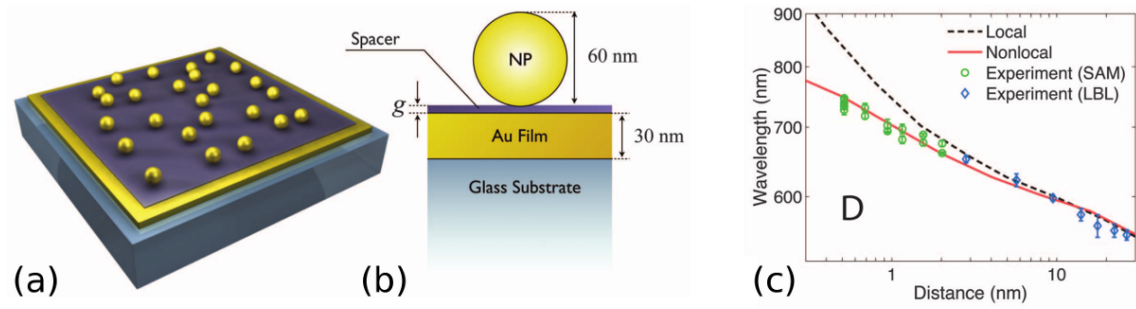
Figure 1.3.: Graphic taken from [7]. (a) Schematic experimental setup. (b) Cross-section of the setup. (c) Comparison of measured data with simulated data.
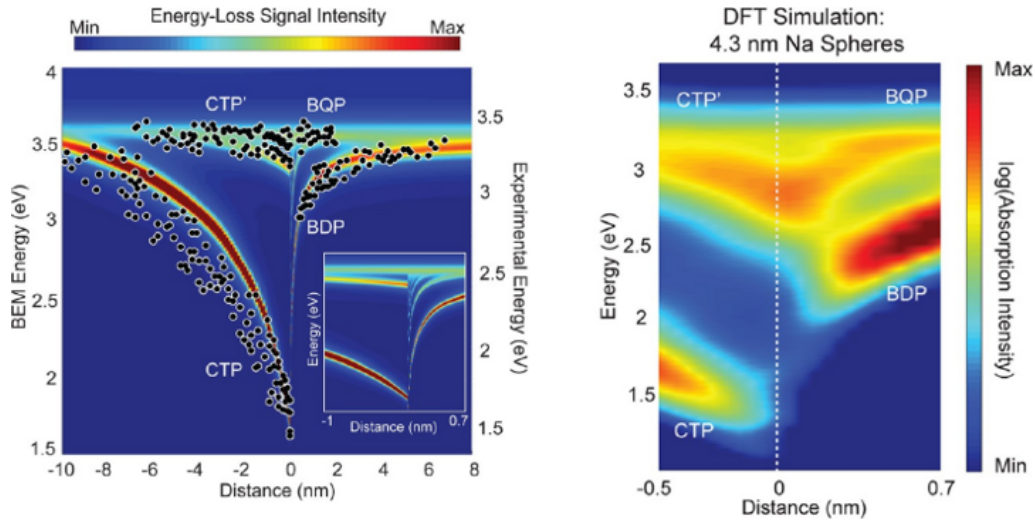
Figure 1.4.: Graphic taken from [8]. Both density plots picture EELS simulations with partially added experimental data. (Left) Classical BEM simulations with experimental data - black circles. (Right) Density Functional Theory (DFT) simulation.

2. Electrodynamic Simulations – Gap Plasmonics – Theory

> Physics has a history of synthesizing many phenomena into a few theories.
>
> Richard P. Feynman

This chapter collects the most important theories, methods and some basic ideas which have been used for the electrodynamic simulations of this thesis. It starts with an overview of different types of plasmonic resonances and how they can be excited.

In this thesis the simulations of plasmon resonances are based on the classical field theory, which can be represented by Maxwell's equations or by Helmholtz equations, respectively. In detail, a numerical method, which solves the Helmholtz equations via a Green's function technique, forms the technical framework of the simulations. For further use, the Transfer matrix method and the Drude model is also introduced.

Finally, a quantum correction concerning the classical simulations is introduced via the so-called quantum corrected model.

2.1. Types of Plasmons

In general a plasmon can be described as a collective charge density oscillation. As we will discuss later, there are different ways of exciting plasmonic resonances and not every plasmonic resonance can be excited with every kind of excitation.

Plasmon resonances can be distinguished as follows: collective charge oscillations in the volume of a metal (volume plasmons) and at the boundary between a metal and a dielectric (surface plasmons).

2.1.1. Volume Plasmon

A volume plasmon is a collective charge density oscillation in the volume of a metal. The plasma frequency[1] of the metal [28]

$$\omega_p = \sqrt{\frac{Ne^2}{m\epsilon_0}} \tag{2.1}$$

determines the resonance of a volume plasmon inside the metal, where e is the electron charge, N is the number of conducting electrons per unit volume, ϵ_0 is the permittivity of vacuum, and m is the effective electron mass.

In order to tune the resonance frequency of a volume plasmon one has to consider different materials with different parameters N and m.

---

[1]A metal will reflect most of incident light which has a frequency below the plasma frequency of the metal and transmit most of incident light which has a frequency above the plasma frequency of the metal.

2.1.2. Surface Plasmon

A surface plasmon (SP) is a delocalized, collective charge density oscillation which can appear at the interface between a conductor and a dielectric [15]. Such an oscillation propagates along the surface. A surface plasmon combined with its associated electrodynamic fields (at the dielectric side) is called surface plasmon polariton (SPP). The direction of the electric field which points into the metal and into the dielectric decays exponentially, which is called to be evanescent. Typically the evanescent part reaches a few nanometers into the metal (skin depth), while the propagation parallel to the surface is damped after a few micrometers (propagation length) [29]. Usually thin and flat metal films are used for producing such a plasmon.

The resonance frequency of a SP is determined by the material parameters (permittivity) of the conductor and the dielectric.

2.1.3. Localized Surface Plasmon

For metal structures that are confined to about 10 to 100 nanometers in all spatial directions and are embedded in a dielectric surrounding, collective charge density oscillations can be reflected at the metal boundaries. Interference of the oscillations with their reflections finally leads to stationary, collective charge density oscillations also known as localized surface plasmons.

In contrast to the previous types of resonances not only the optical parameters of the metal determine the plasmon frequency. The geometry of the structure and the optical parameters of the metal and the surrounding dielectric determine the excitation frequencies of plasmon resonances as well.

2.1.4. Tunneling Charge Transfer Plasmon

If two metal structures are separated only subnanometers by a dielectric, it has to be taken into account that electron tunneling through the gap from one metal structure to the other becomes possible [6–9]. In contrast to a localized surface plasmon, where the full plasmon oscillation happens within one metal structure, a tunneling Charge Transfer Plasmon (tCTP) is not limited to oscillate within one metallic particle anymore. As the name already indicates, charge will be transported from one metallic particle to another one and back again through tunneling.

For two particles having the same shapes and consisting of the same materials separated by a subnanometer gap, a tCTP is expected to appear at the frequency of the hypothetical monopole-mode[2] of a single particle, where one particle has opposite charge of the other one.

One difficulty of (experimentally) investigating such plasmons is, that gap distances where tCTP arise are close to the distances of ordinary lattice constants. That means that it is not always perfectly clear that two metal structures are physically separated or not. A trick to avoid this problem is to insert a molecule monolayer in the gap as a distance holder [9].

2.2. Plasmon Excitation

Next we discuss a few methods for exciting plasmon resonances.

---

[2]Since for all modes the full system needs to be charge neutral to fulfill charge conservation, the monopole-mode of a single particle cannot be excited optically.

2.2.1. Surface Plasmon Polariton Excitation

A breakthrough in plasmonics has been the implementation of the optical methods of exciting surface plasmons on metal films by Kretschmann, Otto, and Raether in 1968 [17, 18]. By using the so-called Otto-configuration or the Kretschmann-configuration it is possible to induce surface plasmon resonances on a metal film. An illustration of the
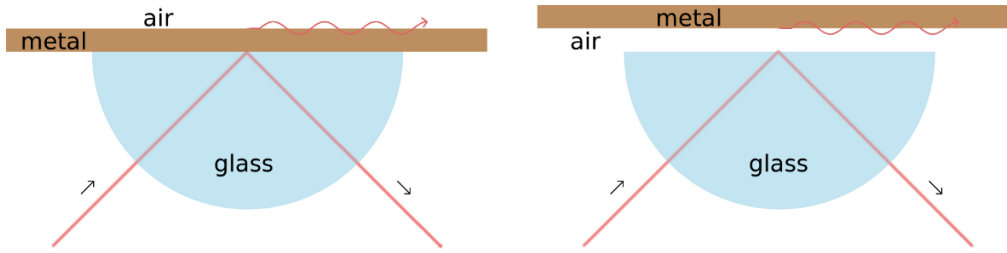
Figure 2.1.: Sketch of the (left) Kretschmann- and the (right) Otto-configuration.

Otto- and the Kretschmann-configuration is given in Fig. 2.1. At the interface glass-metal (glass-air for Otto-geometry) there can occur total internal reflection of the light if the incident angle is above a critical value, which depends on the index of refraction of the used glass. For angles above this critical angle exponentially damped waves reach into the next medium (metal for Kretschmann-geometry and air for Otto-geometry), which can excite a plasmon resonance. Such an exponentially decaying wave is called an evanescent wave.

The use of the Otto- and the Kretschmann-configurations can also be justified by the dispersion relation of a surface plasmon polariton (SPP), sketched in Fig. 2.2. The optical properties of glass (compared to vacuum) changes the light line such that it intersects with the dispersion relation of the SPP. At the intersection point an excitation of a SPP which propagates along the metal surface until it is damped is possible.
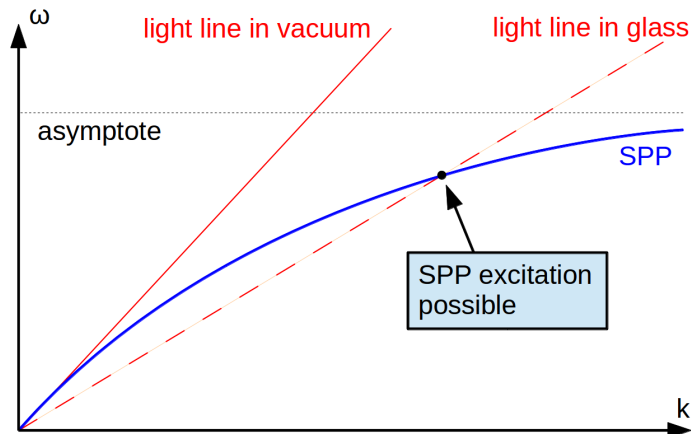
Figure 2.2.: Dispersion relation of a surface plasmon polariton (SPP). ω is called the temporal angular frequency of the SPP and describes the number of oscillations within a time unit. k is called the spatial angular frequency of the SPP and describes the number of oscillations within a space unit (it is indirect proportional to the wavelength of the SPP).

2.2.2. Electron Energy-Loss Spectroscopy (EELS)

A powerful method to excite and detect plasmonic resonances is Electron Energy-Loss Spectroscopy (EELS).
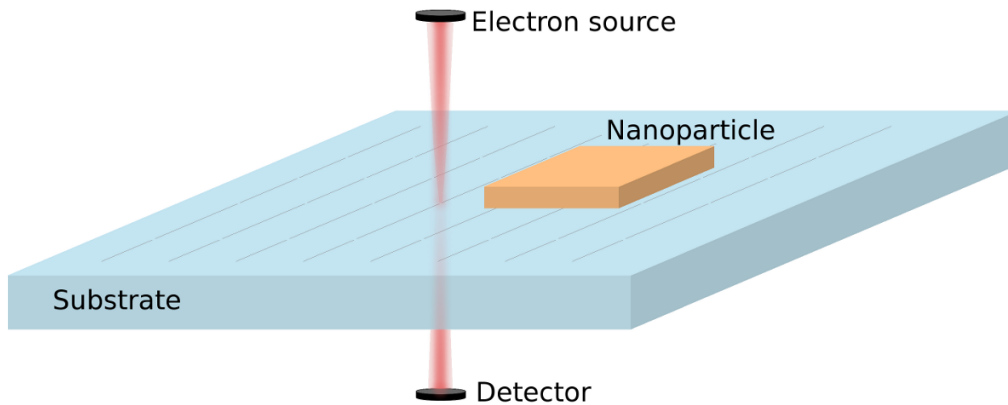
Figure 2.3.: Schematic illustration of an EELS measurement where a nanoparticle is placed on a substrate layer and an electron is traversing the nanoparticle and finally analyzed.

In an EELS measurement an electron traverses a solid nanostructure [15, 30]. Electrons of the nanostructure interact with the traversing electron. This can result in an energy-loss of the traversing electron.

An illustration of an EELS measurement is given in Fig. 2.3. The substrate where the nanoparticle is positioned is usually a thin SiN membrane. If the electron passes next to the metal nanostructure (such as in Fig. 2.3) then only surface plasmons are excited. If the electron traverses directly the metal nanostructure, such that it goes through the metal, then volume plasmon are excited in addition.

The standard EELS measurement is given by a fixed electron source position. By traversing a huge number of electrons one after another and detecting the energy-loss of each electron, a spectrum can be constructed. The peaks in the spectra (after filtering the zero loss peak) can be associated with plasmonic resonance frequencies of the metal nanostructure.

A different type of EELS measurement is given by varying the impact parameter of the electron beam. Then a rastering of the nanostructure's surface is performed, which results in two-dimensional maps.

2.2.3. Optical Excitation

Since light has a magnetic and an electric field component, one can excite a plasmon oscillation by applying monochromatic light onto a probe (nanostructure). The plasmon resonance depends on the wavelength and on the polarization of the light.

If a plasmon is excited by light, then the light is partially scattered and absorbed by the plasmon oscillation. The probability that a photon is scattered by the nanostructure is described by the scattering cross section. The probability that a photon is absorbed by the nanostructure is described by the absorption cross section. The sum of scattered and absorbed light is know as extinction. Hence, the extinction cross section is given by the sum of the scattering cross section and the absorption cross section. In the case of an optical plasmon excitation, one can detect plasmon resonance frequencies by peaks in the corresponding extinction cross section spectra.

Extinction cross section spectra and EEL spectra of the same probe can differ. There exist plasmon resonances which occur in both spectra, such as the dipole plasmon resonance.

2.3. Classical Field Theory

The electromagnetic interaction is fundamental in plasmonic physics. Although the basic interaction principle of electrodynamics, repulsion and attraction, is quite simple, the huge amount of involved electrons in a solid (even for nanoparticles) leads to complicated effects and behaviors, such as plasmonic resonances.

Classical electrodynamics uses the concept of fields. Using a field representation, the fundamental quantities are the electric field and the magnetic induction. For linear materials one can connect them to the dielectric displacement and to the magnetic field respectively by using the electric permittivity and magnetic permeability which are material dependent functions. The dielectric displacement is given by

$$\mathbf{D}(\mathbf{r}, \omega) \equiv \epsilon(\mathbf{r}, \omega)\mathbf{E}(\mathbf{r}, \omega) \tag{2.2}$$

where ϵ is the electric permittivity (dielectric function) and $\mathbf{E}$ is the electric field. Similarly one can define the magnetic induction

$$\mathbf{B}(\mathbf{r}, \omega) \equiv \mu(\mathbf{r}, \omega)\mathbf{H}(\mathbf{r}, \omega) \tag{2.3}$$

where μ is the magnetic permeability and $\mathbf{H}$ is the magnetic field.

2.3.1. Macroscopic Maxwell's Equations

Developed in the 19th century, Maxwell's[3] equations form the basis of classical electrodynamics. In electrodynamics one can operate with fields or with potentials. There are two different types of fields, the electric field and the magnetic field. Mathematically, there are two basic types of vector operations applying the nabla operator onto a vector; the scalar product and the cross product. In total there are four different types of equations, Maxwell's equations, and they read

---

Maxwell's equations

$$\nabla \cdot \mathbf{D}(\mathbf{r}, t) = \rho_f(\mathbf{r}, t) \qquad \text{(Gauss' law)} \tag{2.4}$$

$$\nabla \cdot \mathbf{B}(\mathbf{r}, t) = 0 \tag{2.5}$$

$$\nabla \times \mathbf{E}(\mathbf{r}, t) = -\frac{\partial}{\partial t}\mathbf{B}(\mathbf{r}, t) \qquad \text{(Faraday's induction law)} \tag{2.6}$$

$$\nabla \times \mathbf{H}(\mathbf{r}, t) = \mathbf{J}_f(\mathbf{r}, t) + \frac{\partial}{\partial t}\mathbf{D}(\mathbf{r}, t) \qquad \text{(Ampère's circuital law)} \tag{2.7}$$

---

where ρ_f is the free charge density and $\mathbf{J}_f$ is the free current density.

Boundary Conditions

At the boundary between two different dielectric materials, in the following denoted by the indices i and j, the fields (solutions of Maxwell's equations) need to fulfill certain criteria,

---

[3]James Clerk Maxwell, Scottish physicist, *1831, +1879.

> **Boundary Conditions**
>
> $$\mathbf{n} \times (\mathbf{E}_i - \mathbf{E}_j) = \mathbf{0} \tag{2.8}$$
> $$\mathbf{n} \times (\mathbf{H}_i - \mathbf{H}_j) = \mathbf{K}_f \tag{2.9}$$
> $$\mathbf{n} \cdot (\mathbf{D}_i - \mathbf{D}_j) = \sigma_f \tag{2.10}$$
> $$\mathbf{n} \cdot (\mathbf{B}_i - \mathbf{B}_j) = 0 \tag{2.11}$$

where $\mathbf{n}$ is the normal unit vector of the boundary surface, the vector $\mathbf{K}_f$ is the free surface current density and σ_f is the free surface charge density.

Electric Potential and Magnetic Vector Potential

By using the concept of potentials one can define the electric field via the scalar potential ϕ and the vector potential $\mathbf{A}$

$$\mathbf{E} = -\frac{\partial}{\partial t}\mathbf{A} - \nabla\phi \tag{2.12}$$

The magnetic field reads

$$\mathbf{H} = \frac{1}{\mu}\nabla \times \mathbf{A} \tag{2.13}$$

Inserting Eqn. 2.12 into Gauss' law (Eqn. 2.4) gives

$$-\nabla \cdot \epsilon \left(\frac{\partial}{\partial t}\mathbf{A} + \nabla\phi\right) = \rho_f \tag{2.14}$$

Inserting Eqn. 2.12 and Eqn. 2.13 into Ampère's circuital law (Eqn. 2.7) gives

$$\nabla \times \left(\frac{1}{\mu}\nabla \times \mathbf{A}\right) = \mathbf{J}_f - \frac{\partial}{\partial t}\epsilon\left(\frac{\partial}{\partial t}\mathbf{A} + \nabla\phi\right) \tag{2.15}$$

2.3.2. Helmholtz Equations

Assuming the electric permittivity and the magnetic permeability are constant parameters, then Eqn. 2.14 simplifies to

$$\frac{\partial}{\partial t}\nabla \cdot \mathbf{A} + \nabla^2\phi = -\frac{\rho_f}{\epsilon} \tag{2.16}$$

and Eqn. 2.15 simplifies to

$$\nabla(\nabla \cdot \mathbf{A}) - \nabla^2\mathbf{A} = \mu\mathbf{J}_f - \mu\epsilon\frac{\partial^2}{\partial t^2}\mathbf{A} - \mu\epsilon\frac{\partial}{\partial t}\nabla\phi \tag{2.17}$$

By utilizing gauge transformations[4] one can decouple these differential equations. By using the Lorenz[5] gauge, $\nabla \cdot \mathbf{A} = -\mu\epsilon\frac{\partial}{\partial t}\phi$, we obtain

$$\nabla^2\phi - \mu\epsilon\frac{\partial^2}{\partial t^2}\phi = -\frac{\rho_f}{\epsilon} \tag{2.18}$$

$$\nabla^2\mathbf{A} - \mu\epsilon\frac{\partial^2}{\partial t^2}\mathbf{A} = -\mu\mathbf{J}_f \tag{2.19}$$

---

[4] In order to simplify one of the differential equations one usually takes either the Coulomb gauge, $\nabla \cdot \mathbf{A} = 0$, or the Lorenz gauge, $\nabla \cdot \mathbf{A} = -\mu\epsilon\frac{\partial}{\partial t}\phi$, depending on the physical problem.
[5] Ludvig Valentin Lorenz, Danish physicist, *1829, +1891.

Assuming the potentials can be written as

$$\phi(\mathbf{r}, t) = \phi(\mathbf{r})e^{-i\omega t} \tag{2.20}$$

$$\mathbf{A}(\mathbf{r}, t) = \mathbf{A}(\mathbf{r})e^{-i\omega t} \tag{2.21}$$

then one can eliminate the time derivatives

$$\nabla^2 \phi + \mu\epsilon\omega^2\phi = -\frac{\rho_f}{\epsilon} \tag{2.22}$$

$$\nabla^2 \mathbf{A} + \mu\epsilon\omega^2\mathbf{A} = -\mu\mathbf{J}_f \tag{2.23}$$

Using $k = \omega\sqrt{\mu\epsilon} = \frac{n}{c}\omega$ we obtain the Helmholtz[6] equations for the scalar potential and vector potential

> **Helmholtz equations**
>
> $$\left(\nabla^2 + k^2\right)\phi(\mathbf{r}) = -\frac{\rho_f}{\epsilon} \qquad (2.24)$$
> $$\left(\nabla^2 + k^2\right)\mathbf{A}(\mathbf{r}) = -\mu\mathbf{J}_f \qquad (2.25)$$

2.3.3. Green Function Technique

In order to solve the Poisson[7] equation

$$\nabla^2 \phi(\mathbf{r}) = -f(\mathbf{r}) \tag{2.26}$$

one can use the Green[8] function technique [31]. The Green function G for the Poisson equation can be defined by

$$\nabla^2 G(\mathbf{r}, \mathbf{r}') = -4\pi\delta(\mathbf{r} - \mathbf{r}') \tag{2.27}$$

where $\delta(\mathbf{r} - \mathbf{r}')$ is the delta functional. The multiplication of both sides with the inhomogeneous term $f(\mathbf{r}')$ gives

$$\nabla^2 G(\mathbf{r}, \mathbf{r}')f(\mathbf{r}') = -4\pi\delta(\mathbf{r} - \mathbf{r}')f(\mathbf{r}') \tag{2.28}$$

The integration over the volume Ω results in

$$\int_\Omega \nabla^2 G(\mathbf{r}, \mathbf{r}')f(\mathbf{r}')d^3r' = -4\pi \int_\Omega \delta(\mathbf{r} - \mathbf{r}')f(\mathbf{r}')d^3r' \tag{2.29}$$

$$= -4\pi f(\mathbf{r}) \tag{2.30}$$

$$= 4\pi\nabla^2\phi(\mathbf{r}) \tag{2.31}$$

By interchanging the integral and Laplace[9] operator we get

$$\phi(\mathbf{r}) = \frac{1}{4\pi} \int_\Omega G(\mathbf{r}, \mathbf{r}')f(\mathbf{r}')d^3r'. \tag{2.32}$$

---

[6] Hermann Ludwig Ferdinand von Helmholtz, German physicist, *1821, +1894.
[7] Siméon Denis Poisson, French mathematician and physicist, *1781, +1840.
[8] George Green, British mathematical physicist, *1793, +1841.
[9] Pierre-Simon Laplace, French mathematician, physicist and astronomer, *1749, +1827.

2.3.4. Quasistatic Approximation

The Helmholtz equations provide a description of an electromagnetic system which is equivalent to the Maxwell equations [1,32]. We start with the wave equation for the scalar potential (Eqn. 2.24).

$$\left(\nabla^2 + k^2\right)\phi = -\frac{\rho_f}{4\pi\epsilon} \tag{2.33}$$

For sufficiently small particles we can neglect k and Eqn. 2.33 reduces to the Poisson equation

$$\nabla^2\phi = -\frac{\rho_f}{4\pi\epsilon} \tag{2.34}$$

In order to solve this differential equation we apply the concepts of Green functions. The Green function of this system which satisfies [1, 4, 32]

$$\nabla^2 G(\mathbf{r}, \mathbf{r}') = -4\pi\delta(\mathbf{r} - \mathbf{r}') \tag{2.35}$$

reads

$$G(\mathbf{r}, \mathbf{r}') = \frac{1}{|\mathbf{r} - \mathbf{r}'|} \tag{2.36}$$

Using Eqn. 2.32 we get

$$\phi(\mathbf{r}) = \int_\Omega G(\mathbf{r}, \mathbf{r}')\frac{\rho_f(\mathbf{r}')}{4\pi\epsilon(\mathbf{r}')}d^3r'. \tag{2.37}$$

We are interested in systems without free charges. For such systems sources can only appear at the boundaries $\partial\Omega$ of the (nano)particles. Consequently, one can use surface terms instead of volume terms, e.g. $\rho_f \to \tilde{\sigma}$. By using an alternative definition of the surface charge density $\sigma(\mathbf{r}) = \frac{\tilde{\sigma}(\mathbf{r})}{4\pi\epsilon(\mathbf{r})}$ one can write the scalar potential as [33]

$$\phi(\mathbf{r}) = \int_{\partial\Omega} G(\mathbf{r}, \mathbf{r}')\sigma(\mathbf{r}')da' + \phi_{\text{ext}}(\mathbf{r}) \tag{2.38}$$

where $\phi_{\text{ext}}(\mathbf{r})$ is the external excitation. The full potential needs to fulfill the boundary conditions

$$\phi_1\bigg|_{\partial\Omega} = \phi_2\bigg|_{\partial\Omega} \tag{2.39}$$

$$\epsilon_1\phi_1'\bigg|_{\partial\Omega} = \epsilon_2\phi_2'\bigg|_{\partial\Omega} \tag{2.40}$$

where ϕ' is the normal derivation of the potential perpendicular to the surface. The indices 1 and 2 denote each side of the surface. From the first boundary condition it follows that $\sigma_1 = \sigma_2$.

Considering the second boundary condition, the normal derivation perpendicular to the surface is given by $\frac{\partial\phi}{\partial n} = \hat{\mathbf{n}} \cdot \nabla\phi(\mathbf{r})$. Using the definition $F(\mathbf{s}, \mathbf{s}') = (\hat{\mathbf{n}} \cdot \nabla)G(\mathbf{s}, \mathbf{s}')$ the directional derivative perpendicular to the surface of the potential is given by [34]

$$\frac{\partial\phi(\mathbf{s})}{\partial n} = \int_{\partial\Omega} F(\mathbf{s}, \mathbf{s}')\sigma(\mathbf{s}')da' \pm 2\pi\sigma(\mathbf{s}) + \frac{\partial\phi_{\text{ext}}}{\partial n}. \tag{2.41}$$

The limit $\lim_{\mathbf{r}\to\mathbf{s}} \hat{\mathbf{n}} \cdot \nabla \int G\sigma da'$ describes the approach to a surface point $\mathbf{s}$. The sign of the term $\pm 2\pi\sigma(\mathbf{s})$ depends from which side one approaches to the surface.

Inserting these results into the second boundary condition gives [34]

$$\epsilon_1 \left(F\sigma - 2\pi\sigma + \frac{\partial\phi_{\text{ext}}}{\partial n} \right) = \epsilon_2 \left(F\sigma + 2\pi\sigma + \frac{\partial\phi_{\text{ext}}}{\partial n} \right) \tag{2.42}$$

$$2\pi\sigma(\epsilon_2 + \epsilon_1) + F\sigma(\epsilon_2 - \epsilon_1) = -(\epsilon_2 - \epsilon_1)\frac{\partial\phi_{\text{ext}}}{\partial n} \tag{2.43}$$

The surface charge density of the quasistatic approximation reads

$$\sigma = -(\Lambda + F)^{-1}\frac{\partial\phi_{\text{ext}}}{\partial n} \tag{2.44}$$

where all material information are given in $\Lambda = 2\pi\frac{\epsilon_2 + \epsilon_1}{\epsilon_2 - \epsilon_1}$ and all geometric information of the system are given in F [4].

2.3.5. Retarded Solution

The Green function technique introduced above can be generalized to linear operators replacing the Laplace operator in Eqn. 2.26. The retarded Green function of Eqn. 2.33 reads [4, 32, 35]

$$G(\mathbf{r}, \mathbf{r}') = \frac{e^{ik|\mathbf{r} - \mathbf{r}'|}}{|\mathbf{r} - \mathbf{r}'|} \tag{2.45}$$

Since k depends on ϵ, $k = \omega\sqrt{\mu\epsilon}$, for homogeneous materials we introduce indices j for each medium. Then the retarded Green function has to fulfill

$$\left(\nabla^2 + k_j^2\right)G_j(\mathbf{r}, \mathbf{r}') = -4\pi\delta(\mathbf{r} - \mathbf{r}). \tag{2.46}$$

The scalar potential and the vector potential read

$$\phi(\mathbf{r}) = \int_{\partial\Omega_j} G_j(\mathbf{r} - \mathbf{r}')\sigma_j(\mathbf{r}')da' + \phi_{\text{ext}}(\mathbf{r}) \tag{2.47}$$

$$\mathbf{A}(\mathbf{r}) = \int_{\partial\Omega_j} G_j(\mathbf{r} - \mathbf{r}')\mathbf{h}_j(\mathbf{r}')da' + \mathbf{A}_{\text{ext}}(\mathbf{r}). \tag{2.48}$$

2.3.6. Boundary Element Method

Eqn. 2.41 can be solved analytically for highly symmetric boundary geometrics only, e.g. spherically symmetric structures by Mie theory [13]. For arbitrary geometrics one needs to use a numerical method, e.g. the Boundary Element Method (BEM) [4, 34]. In order to apply this method one has to discretize the boundaries to so-called boundary elements. An example is given in Fig. 3.2. The boundary is represented by a finite set of boundary elements. Here we introduced the index i, which runs over all boundary elements. Each boundary element can be defined by its vertices (corner points) and a flat surface connecting them. One can further compute for each boundary element i a center point $\mathbf{s}_i$. All boundary elements together, namely the set $\{\mathbf{s}_i\}$, approximate the full boundary.

The integral in Eqn. 2.41 can be substituted by a sum over i. The equation reads [35, 36]

$$\left(\frac{\partial\phi(\mathbf{s})}{\partial n} \right)_i = \left(\sum_j F_{ij}\sigma(\mathbf{s}_j) \right) \pm 2\pi\sigma(\mathbf{s}_i) + \left(\frac{\partial\phi_{\text{ext}}(\mathbf{s})}{\partial n} \right)\Big|_{\mathbf{s} = \mathbf{s}_i}. \tag{2.49}$$
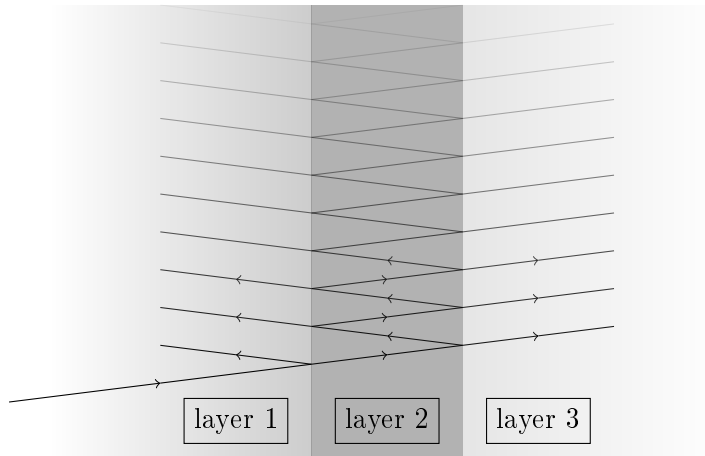
Figure 2.4.: Three layer system. An incoming light wave from the left side which is reflected and transmitted multiple times.

2.3.7. Transfer Matrix Method

In order to theoretically investigate surface plasmon polaritons which propagate along plane surfaces one can use the so-called Transfer Matrix Method. This method provides a solution of the transmission and reflection coefficients of a multi-layer system [37]. In Fig. 2.4 such a system build up of a layer and of two half-infinite layers is sketched. In this figure one can notice the sub-reflections and sub-transmissions. The astonishing fact is that the Transfer Matrix Method includes these sub-terms of reflection and transmission automatically. The boundary conditions of Maxwell's equations forms the basis of this method.

Fresnel Coefficients

It is very helpful to introduce the concept of transversal electric (TE) and transversal magnetic (TM) polarizations. An electromagnetic plane wave can always be described as a superposition of TE and TM waves [1, 32]. In order to derive boundary conditions for TE polarized waves, the direction of the propagation of the wave is set into the xy-plane. Since we deal with TE waves the electric field has a contribution only along the y-direction $\mathbf{E}(\mathbf{r}, t) = E_y(\mathbf{r})\hat{\mathbf{e}}_y e^{-i\omega t}$. By utilizing Gauss' law (Eqn. 2.4) for media with $\rho_f = 0$

$$\nabla \cdot \epsilon(z)\mathbf{E}(\mathbf{r}, t) = 0 \tag{2.50}$$

$$\frac{\partial}{\partial y}\epsilon(z)E_y(\mathbf{r}) = 0 \tag{2.51}$$

$$\epsilon(z)\frac{\partial}{\partial y}E_y(\mathbf{r}) = 0 \tag{2.52}$$

Here we have used that the surfaces of the homogeneous material layers are perpendicular to the xy-plane, hence $\epsilon = \epsilon(z)$. Further by using $\mathbf{H}(\mathbf{r}, t) = \mathbf{H}(\mathbf{r})e^{-i\omega t}$, utilizing Ampère's circuital law (Eqn. 2.7) for media with $\mathbf{J}_f = 0$

$$\nabla \times \mathbf{H}(\mathbf{r}, t) = \frac{\partial}{\partial t}\mathbf{D}(\mathbf{r}, t) \tag{2.53}$$

$$\nabla \times \mathbf{H}(\mathbf{r}) = -i\omega\epsilon(z)\mathbf{E}(\mathbf{r}) \tag{2.54}$$

and applying the curl operator onto Faraday's law (Eqn. 2.6) one gets

$$\nabla \times \mathbf{E}(\mathbf{r}, t) = -\frac{\partial}{\partial t}\mu(z)\mathbf{H}(\mathbf{r}, t) \tag{2.55}$$

$$\frac{1}{\mu(z)}\nabla \times \mathbf{E}(\mathbf{r}) = i\omega\mathbf{H}(\mathbf{r}) \tag{2.56}$$

$$\nabla \times \frac{1}{\mu(z)}\nabla \times \mathbf{E}(\mathbf{r}) = i\omega\nabla \times \mathbf{H}(\mathbf{r}) \tag{2.57}$$

$$\nabla \times \frac{1}{\mu(z)}\nabla \times \mathbf{E}(\mathbf{r}) = i\omega\big(-i\omega\epsilon(z)\mathbf{E}(\mathbf{r})\big) \tag{2.58}$$

$$\mu(z)\nabla \times \frac{1}{\mu(z)}\nabla \times \mathbf{E}(\mathbf{r}) = \omega^2\mu(z)\epsilon(z)\mathbf{E}(\mathbf{r}) \tag{2.59}$$

$$\Big(-\partial_x^2 - \mu(z)\partial_z\frac{1}{\mu(z)}\partial_z\Big)E_y(\mathbf{r}) = \omega^2\mu(z)\epsilon(z)E_y(\mathbf{r}) \tag{2.60}$$

With the ansatz $E_y(\mathbf{r}) = e_y(z)e^{\pm ik_x x}$ the differential equation can be separated.

$$\Big(\mu(z)\partial_z\frac{1}{\mu(z)}\partial_z + \omega^2\mu(z)\epsilon(z) - k_x^2\Big)e_y(z) = 0 \tag{2.61}$$

From this equation one gets two boundary conditions

$$e_{iy} = e_{jy} \tag{2.62}$$

$$\frac{1}{\mu_i(z)}\partial_z e_{iy} = \frac{1}{\mu_j(z)}\partial_z e_{jy} \tag{2.63}$$

where i and j are the indices of two layers next to each other.

In order to find the Fresnel coefficients we consider a system consisting of two different layers where the interface is at $z = 0$ [1]. An incoming TE wave with a field amplitude e_0 will then be partially reflected and transmitted at the boundary. The resulting field in the first medium is then

$$e_{1y}(z) = e_0 e^{ik_{1z}z} + e_0 R e^{-ik_{1z}z} \tag{2.64}$$

where the first term describes the incoming wave and the second term the reflected part introducing the parameter R. The resulting field in the second medium consists of the transmitted wave

$$e_{2y}(z) = e_0 T e^{ik_{2z}z} \tag{2.65}$$

where the parameter T for describing the transmitted part is introduced. The wave vector component in z-direction is $k_{iz} = \sqrt{k_i^2 - k_x^2}$ with $k_i = \omega\sqrt{\mu_i\epsilon_i}$. Applying the first boundary condition (Eqn. 2.62) at $z = 0$ gives

$$e_{1y}\Big|_{z=0} = e_{2y}\Big|_{z=0}$$
$$1 + R = T \tag{2.66}$$

The second boundary condition (Eqn. 2.63) gives

$$\frac{1}{\mu_1}\partial_z e_{1y}\Big|_{z=0} = \frac{1}{\mu_2}\partial_z e_{2y}\Big|_{z=0}$$
$$\frac{k_{1z}}{\mu_1}(1 - R) = \frac{k_{2z}}{\mu_2}T \tag{2.67}$$

The Fresnel coefficients for TE polarized waves are obtained by solving the linear system consisting of Eqs. 2.66 and 2.67. Analogously[10], the Fresnel coefficients for TM polarized waves can be derived [1].

Fresnel Coefficients

$$R_{TE} = \frac{\mu_2 k_{1z} - \mu_1 k_{2z}}{\mu_2 k_{1z} + \mu_1 k_{2z}} \qquad (2.68)$$

$$T_{TE} = \frac{2\mu_2 k_{1z}}{\mu_2 k_{1z} + \mu_1 k_{2z}} \qquad (2.69)$$

$$R_{TM} = \frac{\epsilon_2 k_{1z} - \epsilon_1 k_{2z}}{\epsilon_2 k_{1z} + \epsilon_1 k_{2z}} \qquad (2.70)$$

$$T_{TM} = \frac{2\epsilon_2 k_{1z}}{\epsilon_2 k_{1z} + \epsilon_1 k_{2z}} \qquad (2.71)$$

Transfer Matrix

Let us introduce a two-component-vector notation of the vector field amplitudes, the first component corresponds to the incoming wave and the second one to the outgoing wave [38]. For a multilayer structure, such as in Fig. 2.4, in each layer the field can be noted by the two-vector $\begin{pmatrix} e_i^+ \\ e_i^- \end{pmatrix}$ where '+' stands for 'right-' and '−' for 'left-propagating'. One can construct a matrix $\mathbf{T}_{i,i+1}$ which connects two layers $i, i+1$.

$$\begin{pmatrix} e_i^+ \\ e_i^- \end{pmatrix} = \mathbf{T}_{i,i+1} \begin{pmatrix} e_{i+1}^+ \\ e_{i+1}^- \end{pmatrix} \qquad (2.72)$$

By using the Fresnel coefficients $T_{i,i+1}$ and $R_{i,i+1}$

$$\mathbf{T}_{i,i+1} = \frac{1}{T_{i,i+1}} \begin{pmatrix} 1 & R_{i,i+1} \\ R_{i,i+1} & 1 \end{pmatrix} \qquad (2.73)$$

For the case that there are more than two layers, one needs to take into account the phase shift $e^{\pm i k_{iz} d_i}$ where d_i is the thickness of the i-th layer. This is achieved by the propagation matrix

$$\mathbf{P}_i = \begin{pmatrix} e^{-i k_{iz} d_i} & 0 \\ 0 & e^{i k_{iz} d_i} \end{pmatrix} \qquad (2.74)$$

Transfer Matrix Method

For multilayer systems the field amplitudes of the n-th layer can be connected to the first layer via

$$\begin{pmatrix} e_1^+ \\ e_1^- \end{pmatrix} = \mathbf{T}_{12} \mathbf{P}_2 \mathbf{T}_{23} \mathbf{P}_3 \mathbf{T}_{34} \mathbf{P}_4 \cdot ... \cdot \mathbf{P}_{n-1} \mathbf{T}_{n-1,n} \begin{pmatrix} e_n^+ \\ e_n^- \end{pmatrix} \qquad (2.75)$$

The matrix product $\mathbf{T}_{12} \mathbf{P}_2 \mathbf{T}_{23} \mathbf{P}_3 \cdot ... \cdot \mathbf{P}_{n-1} \mathbf{T}_{n-1,n}$ is called **transfer matrix**.

---

[10]The Fresnel coefficients for TM polarized waves can be derived by applying the curl onto Ampère's circuital law (Eqn. 2.7) and by inserting the second Maxwell equation (Eqn. 2.5).

The relative reflection R and transmission T parts of the whole system can be achieved by the equation

$$\begin{pmatrix} 1 \\ R \end{pmatrix} = \mathbf{M} \begin{pmatrix} T \\ 0 \end{pmatrix} = \begin{pmatrix} m_{11} & m_{12} \\ m_{21} & m_{22} \end{pmatrix} \begin{pmatrix} T \\ 0 \end{pmatrix} = \begin{pmatrix} m_{11}T \\ m_{21}T \end{pmatrix} \tag{2.76}$$

where $\mathbf{M}$ is the transfer matrix. The relative reflection reads $R = \frac{m_{21}}{m_{11}}$ and the relative transmission reads $T = \frac{1}{m_{11}}$ [38].

2.3.8. Drude Model

The Drude model, proposed in 1900 by Paul Drude[11], is a simple approach of classically describing the dynamics of the valence electrons of a solid as an electron gas [39]. The theory came up shortly after Thompson[12] discovered the electron - a milestone in physics history. Although the Drude model is quite a simple model and has its limits[13] it has emerged to be a workhorse in solid state physics. The positive charge contribution of the metal (given by the atomic nuclei) is considered as a uniform distributed background, known as the jellium model, being superimposed by an electron gas which is formed by the conducting electrons (valence electrons) of the metal.

The probability that a collision during a time interval dt takes place is dt/τ, where τ is the mean free time between two collisions (usually in the order of a few fs). The reciprocal value of τ is proportional to the so-called damping term. Lorentz[14] utilized kinetic theory and the Maxwell–Boltzmann distribution in order to generalize the Drude theory.

Finally, after quantum mechanics was conceived, Sommerfeld[15] and Bethe[16] introduced the Sommerfeld[17] model by treating the Drude model quantum mechanically and replacing the Maxwell–Boltzmann distribution by the Fermi-Dirac distribution.

Next we utilize the Drude model to investigate the conductivity of a metal when a constant and an alternating electric field is applied.

DC conductivity

Consider an electron gas of a metal. When applying a constant electric field $\mathbf{E}$, the velocity v of an arbitrary electron at the elapsed time t since its last collision at t_0 reads [41]

$$\mathbf{v} = \mathbf{v}_0 - e\mathbf{E}t/m \tag{2.77}$$

where $e \approx -1.602 \cdot 10^{-19}C$ is the electron charge and $m \approx 9.109 \cdot 10^{-31}kg$ is the electron mass. The mean value of the velocity is $\langle \mathbf{v} \rangle = -e\mathbf{E}\tau/m$, since $\langle \mathbf{v}_0 \rangle = 0$ and $\langle t \rangle = \tau$. The current density $\mathbf{j}$ can be obtained by using the mean value of the electron velocity and the number of electrons n passing a normalized section.

$$\mathbf{j} = -ne\langle \mathbf{v} \rangle = \frac{ne^2\mathbf{E}\tau}{m} \tag{2.78}$$

The proportionality factor of the current density and the electric field equals the DC conductivity

$$\sigma_0 = \frac{ne^2\tau}{m}. \tag{2.79}$$

---

[11] Paul Karl Ludwig Drude, German physicist, *1863, +1906.
[12] Sir Joseph John Thomson, English physicist, *1856, +1940.
[13] The Drude model fails in describing the electronic heat capacity of metals.
[14] Hendrik Antoon Lorentz, Dutch physicist, *1853, +1928.
[15] Arnold Johannes Wilhelm Sommerfeld, German physicist, *1868, +1951.
[16] Hans Albrecht Bethe, German physicist, *1906, +2005.
[17] The Sommerfeld model estimates the electronic heat capacity of metals in good agreement with experiments [40]. This is mainly caused by the usage of the Fermi-Dirac distribution function.

AC conductivity

Consider an alternating electric field

$$\mathbf{E}(t) = \mathbf{E}_0 e^{-i\omega t} \tag{2.80}$$

that is applied on a metal [41]. Using the general classical equation of motion

$$\frac{d\mathbf{p}(t)}{dt} = \frac{\mathbf{p}(t)}{\tau} + \mathbf{f}(t), \tag{2.81}$$

the force $\mathbf{f}(t)$ acting on an arbitrary electron is $-e\mathbf{E}(t)$. The solution of the differential equation is $\mathbf{p}(t) = \mathbf{p}_0 e^{-i\omega t}$. The current density reads

$$\mathbf{j} = -ne\langle \mathbf{p}\rangle/m = \frac{\sigma_0}{1 - i\omega\tau}\mathbf{E} \tag{2.82}$$

The AC conductivity reads

$$\sigma(\omega) = \frac{\sigma_0}{1 - i\omega\tau} \tag{2.83}$$

Dielectric function

The Drude model describes a free electron gas in a metal. If an electric field $\mathbf{E}_0 e^{-i\omega t}$ is applied the dynamics of a single electron can be described by [4]

$$m_e \frac{\partial^2 \mathbf{r}}{\partial t^2} + m_e \gamma_d \frac{\partial \mathbf{r}}{\partial t} = -e\mathbf{E}_0 e^{-i\omega t} \tag{2.84}$$

where γ_d is a damping term and m_e is the effective mass of the electron. The solution of this differential equation reads

$$\mathbf{r}(t) = \frac{e}{m_e}\frac{1}{\omega^2 + i\gamma_d\omega}\mathbf{E}_0 e^{-i\omega t} \tag{2.85}$$

The dielectric function of a linear and homogeneous medium[18] can be derived using the polarization $\mathbf{P}$ of the material and the expression of the dielectric displacement

$$\mathbf{D} = \epsilon\mathbf{E} = \epsilon_0\mathbf{E} + \mathbf{P} = \epsilon_0\left(1 - \frac{\omega_p^2}{\omega^2 + i\gamma_d\omega}\right)\mathbf{E} \tag{2.86}$$

where ω_p is the plasma frequency. The dielectric function which characterizes the material reads

$$\epsilon_r(\omega) = 1 - \frac{\omega_p^2}{\omega^2 + i\gamma_d\omega} \tag{2.87}$$

Due to screening caused by electrons bound to the positive ion cores this equation generalizes to

$$\epsilon_r(\omega) = \epsilon_\infty - \frac{\omega_p^2}{\omega^2 + i\gamma_d\omega} \tag{2.88}$$

where ϵ_∞ is the permittivity due to ionic background as a result of the screening effect. An improvement of the dielectric function is given by the Lorentz oscillator where an additional restoring force is inserted in the differential equation of the electron's dynamics.

$$m_e \frac{\partial^2 \mathbf{r}}{\partial t^2} + m_e\gamma_d\frac{\partial\mathbf{r}}{\partial t} + m_e\omega_0^2\mathbf{r} = -e\mathbf{E}_0 e^{-i\omega t} \tag{2.89}$$

The corresponding dielectric function reads

$$\epsilon_r(\omega) = 1 - \frac{\omega_p^2}{(\omega^2 - \omega_0^2) + i\gamma_d\omega} \tag{2.90}$$

In Fig. 2.5 the real and imaginary part of a dielectric function of silver using Drude theory and of a dielectric function of silver extracted from experiment [42] is plotted.

---

[18] In general the dielectric function is a tensor of rank 2.
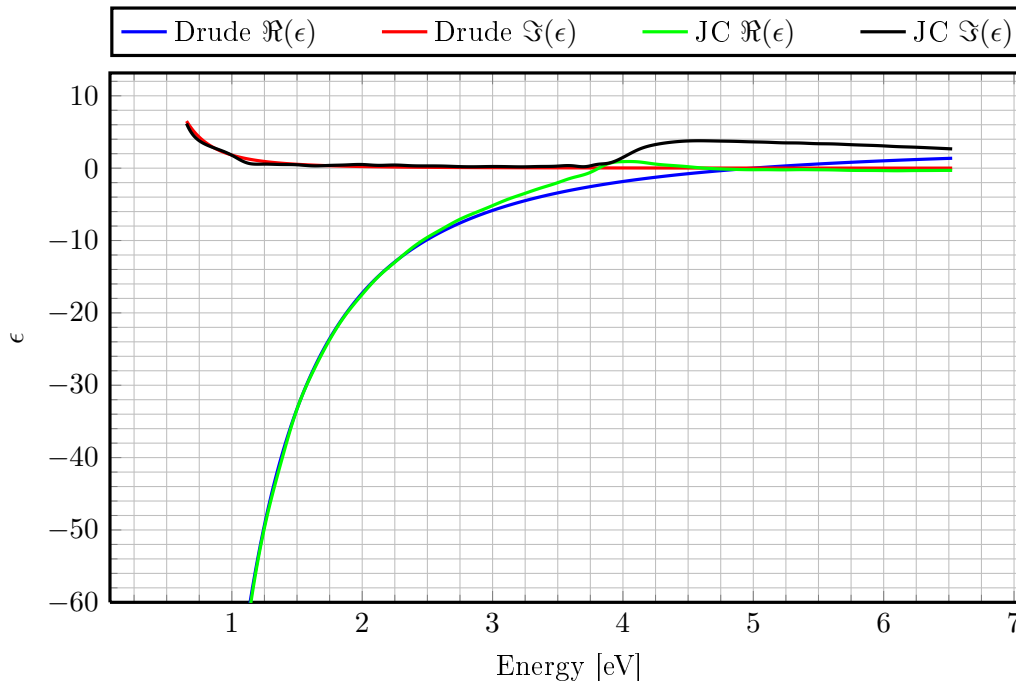
Figure 2.5.: Drude versus experiment (Johnson and Christy [42]) for the
real and imaginary part of the dielectric function of silver.

2.4. Quantum Corrected Model

The above described Boundary Element Method (BEM) provides a solution scheme for the classical electrodynamic equations. For many systems the results of this classical method are in good agreement with experiments. Even for most particles in the nanometer regime. For instance Ag particles with a diameter of approximately 10 nm or more are described in a good agreement by classical electrodynamics [43]. A major question throughout this thesis is about the principal behavior of plasmonic resonances when two metallic nanoparticles approach closer than a distance where electrodynamics fails.

One possibility to include quantum effects to the Boundary Element Method is by using the so-called Quantum Corrected Model (QCM) [44]. The idea of this model is to insert an effective material in the gap between the particles and to find its optical properties, e.g. the dielectric function.

In the following two different types of the QCM are considered.

2.4.1. Quantum Corrected Model

The geometric structure of a nanoparticle can be numerically described by a discretization of the structure into volume (or boundary) elements. For each volume element one defines an electric permittivity and a magnetic permeability according to the given nanostructure. When considering two metallic nanoparticles, which are separated by less than one nanometer, it becomes important to include quantum effects such as electron tunneling. The QCM provides a simple approach to implement quantum effects as follows [44]: One inserts an additional, fictitious material into regions where quantum effects are expected, e.g. gap regions. The difficulty is to find an appropriate conductivity for such a tunneling-imitating material.

The implementation of the QCM can be achieved by additional volume elements in relevant regions. For each additional volume element, suitable optical properties have to be declared, which depend on the gap width l, on the frequency ω and on the material of

the nanoparticles. For instance the Drude model can be used, in particular Eqn. 2.88, to obtain the permittivity of the fictitious material

$$\epsilon(l,\omega) = \epsilon_\infty - \frac{\omega_g^2}{\omega^2 + i\gamma_g(l)\omega} \tag{2.91}$$

where ω_g is the plasma frequency and $\gamma_g(l)$ is the tunneling damping parameter of the additional material [44]. Usually the plasma frequency of the fictitious material is assumed to be equal to the plasma frequency ω_p of the surrounding nanoparticles. The same assumption is made for ϵ_∞. The tunneling damping $\gamma_g(l)$ can be calculated for $\omega \ll \gamma_g$ by

$$\gamma_g(l) = \frac{\omega_g^2}{4\pi\sigma_g(l)} \tag{2.92}$$

where σ_g is the conductivity of the additional material [44, 45].

2.4.2. Boundary Quantum Corrected Model

Since the previously introduced standard QCM uses volume elements and the BEM uses boundary elements, it is not a proper way to combine standard QCM with BEM. The so-called boundary QCM is an alternative specific version of the standard QCM and has been developed [46] for the usage with BEM. It can be used for coupled (nano)particles, especially to enable the process of electron tunneling between the coupled particles. The assumption of the model is, that if an electron leaves a (nano)particle it has to enter the other (nano)particle. Note that such a behavior is non-local.

Let us start with Ohm's law corresponding the tunnel current. A tunnel current $\mathbf{J}_t$ can flow if an electric field $\mathbf{E}$ is applied in the gap region. According to Ohm's law, the current scales linear with the electric field

$$\mathbf{J}_t = \sigma_t \mathbf{E} \tag{2.93}$$

where σ_t is the gap conductivity. By using the continuity equation

$$\partial_t \rho = -\nabla \cdot \mathbf{J}_t \tag{2.94}$$

with the charge density $\rho(\mathbf{r}, t) = \rho(\mathbf{r})e^{-i\omega t}$ and Gauss law one can write

$$\oint \mathbf{D} \cdot d\mathbf{a} = \int \nabla \cdot \mathbf{D}d\tau = 4\pi \int \rho d\tau$$
$$= \frac{4\pi}{i\omega} \int \nabla \cdot \mathbf{J}_t d\tau$$
$$= \frac{4\pi}{i\omega} \oint \mathbf{J}_t \cdot d\mathbf{a}. \tag{2.95}$$

This leads to modified boundary conditions [46].

$$D_{2a}^\perp - D_{1a}^\perp = -\frac{4\pi i}{\omega}J_t^\perp \tag{2.96}$$

$$D_{3b}^\perp - D_{2b}^\perp = \frac{4\pi i}{\omega}J_t^\perp \tag{2.97}$$

By making the assumption [46]

$$\mathbf{J}_t = \sigma_t \frac{\mathbf{E}_{2a} - \mathbf{E}_{2b}}{2} \tag{2.98}$$

the boundary conditions read [46]

QCM Boundary Conditions

$$D_{2a}^{\perp} - D_{1a}^{\perp} = -\frac{4\pi i \sigma_t}{\omega}\frac{E_{2a}^{\perp} - E_{2b}^{\perp}}{2} \qquad (2.99)$$

$$D_{3b}^{\perp} - D_{2b}^{\perp} = -\frac{4\pi i \sigma_t}{\omega}\frac{E_{2b}^{\perp} - E_{2a}^{\perp}}{2} \qquad (2.100)$$

---

where σ_t is the gap conductivity which usually strongly depends on the gap width. The indices of the equations are depicted in Fig. 2.6. The alignment of the boundary can be arbitrary, it must not be planar. Notice the **non-local** characteristic of the altered boundary conditions. When using a method which only takes boundary elements into

Figure 2.6.: A three layer interface for introducing the boundary QCM.

account, the boundary QCM should be preferred instead of the volume QCM. For the application in the boundary element method one of the benefits is that no additional boundary element has to be constructed. This leads to a faster convergence of the spectra compared to the usage of the volume QCM. Another great benefit is that there are no ohmic losses for electron transmission through the gap region.

2.4.3. Optical Properties of Gaps Within the QCM

One of the difficulties of QCM is to find the optical properties, i.e. the dielectric function, of the effective gap material. When investigating tunnel resonances of coupled metallic nanoparticles, the demanded functionality of the gap in between is to be an isolating layer such that the probability of electron tunneling from one to the other particle is not negligibly small. In principle any material could be inserted into the gap unless it is not a conductor. One simple reason should justify this point: When using a conductor as a gap material then electron transport through the gap can be described by classical physics which implies that QCM is not needed for this case.

Next, simple models for vacuum gaps and material-filled gaps are introduced.

Vacuum Gap

One of the simplest types of gaps in the classical sense is a vacuum gap. A simple model for the dielectric function in the gap is [47]

$$\epsilon(l) = 1 + i\frac{\sigma(l)}{\epsilon_0 \omega} \qquad (2.101)$$

where the gap-width-dependent conductivity reads

$$\sigma(l) = -\mathfrak{Im}\left[\frac{\omega_p^2}{\omega^2 + i\omega\gamma_p e^{l/l_c}}\right] \qquad (2.102)$$

The exponential behavior of the damping term corresponding to the gap-width l connects the damping term of the surrounding media γ_p with the damping term of the fictitious gap

material γ_g via

$$\gamma_g(l) = \gamma_p e^{l/l_c} \qquad (2.103)$$

where l_c is a tunneling length scale which depends on the surrounding nanoparticles [47,48].

Material Gap

A material gap is here considered to be a gap filled with (non-conducting) material. One benefit of material-filled gaps is that they can have the functionality of keeping the coupled metallic nanoparticles apart. Another benefit of a material-filled gap is that the metallic nanoparticles can be separated by larger gaps, where the probability of electron tunneling is not yet negligibly small.

It should be quite clear, particularly when regarding investigations of electron tunneling through the gap, that the gap material must not be a (Drude) conductor. In this thesis a self-assembled monolayer (SAM) of a molecule type is considered. Although the gap material is non-metallic, the highest occupied energy levels of the gap material will naturally lead to a smaller potential well for a tunneling event. The dielectric function of a non-metallic gap reads

$$\epsilon(\omega) = 1 + i\frac{\sigma_0}{\epsilon_0 \omega} \qquad (2.104)$$

where σ_0 is the static conductivity of the gap material and can be calculated from first principles by using quantum theories such as the Landauer-Büttiker formalism, introduced in Sec. 4.3.

In contrast, the dielectric function of a metallic gap reads

$$\epsilon(\omega) = 1 + i\frac{\sigma(\omega)}{\epsilon_0 \omega} \qquad (2.105)$$

where for instance Eqn. 2.83 could be applied to calculate the conductivity $\sigma(\omega)$. As mentioned before, (Drude) conductors as gap materials should be avoided when investigating electron tunneling.

3. Electrodynamic Simulations - Gap Plasmonics - Results

3.1. MNPBEM Toolbox

In order to simulate metallic nanoparticles one can apply the Boundary Element Method (BEM). In this thesis an implementation of BEM, the Metallic Nano Particle Boundary Element (MNPBEM) Matlab toolbox [49–51], has been used. It is based on the BEM of Garcia de Abajo, Howie and Aizpurua [34, 35]. One can solve the Helmholtz equations of interface systems consisting of homogeneous and isotropic optical particle properties. The MNPBEM toolbox provides routines to solve quasi-static and retarded systems when excited optically or by an electron beam.
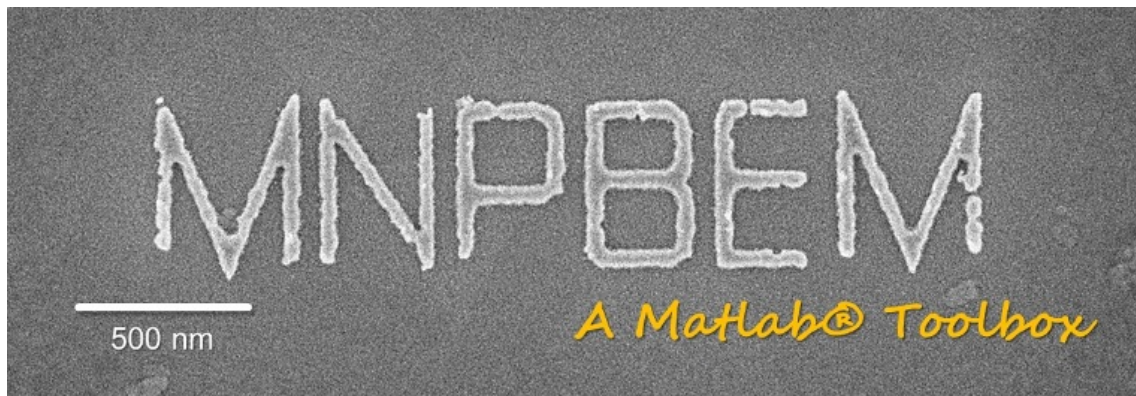
Figure 3.1.: Metallic Nano Particle Boundary Element Method (MNPBEM) logo.

3.2. Boundary Element Structures

In order to perform simulations using the Boundary Element Method, the boundary of the particles of the investigated system needs to be discretized. The particle's boundary is separated into so-called boundary elements as sketched in Fig. 3.2. The sizes of the boundary elements determine the convergence and the duration of a BEM calculation. It is clear that a larger number of boundary elements would lead to a longer calculation time. Consequently, keeping the number of boundary elements as small as possible and obtaining converged BEM results at the same time, arises to be a great challenge of this method.

Usually the problematic areas of a surface are curved or even edged. For strong curved or edged surfaces one usually needs much more elements than for comparable weakly curved or smooth surfaces. However, it should be avoided to use sharply edged structures within the BEM.
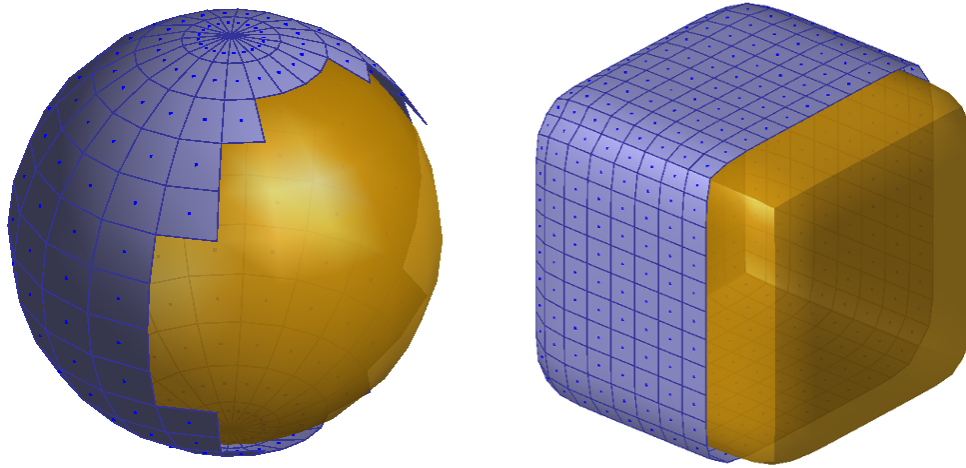
Figure 3.2.: Examples of boundary elements (sphere and cube).

3.2.1. Dimers

The structures which are of most interest in this thesis are coupled metallic nanoparticles, e.g. two coupled silver nanocubes, where the particles have identical shapes. A system of such two coupled particles is called a dimer.

Going back to the problem of constructing the boundary elements of a particle system, we consider coupled particles. For two coupled particles, there might be a region of the boundary of each particle, which is relatively close to the boundary of the other particle. At such regions the boundary needs to be discretized into smaller boundary elements as it would be for investigating the single particle.
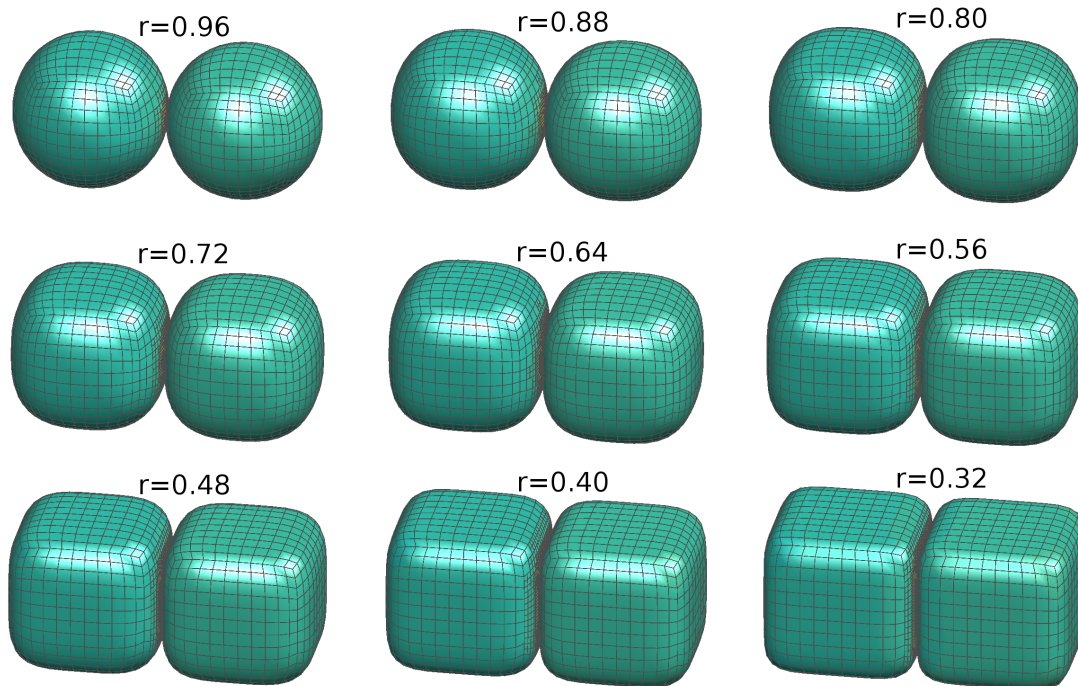
Figure 3.3.: Super-ellipsoid shapes for different rounding parameters r.

3.2.2. Morphing

In order to compare coupled cubes and coupled spheres one can perform a continuous transition between those shapes [52]. One can use different methods to describe such a continuous transition. Here the concept of super-ellipsoids is introduced to enable the morphing of a sphere into a cube. In detail each of the particles of the dimer is represented by a super-ellipsoid. A super-ellipsoid can be defined by

$$\mathbf{r}(\theta, \phi, r) = \frac{d}{2} \begin{pmatrix} s(\theta, r)c(\phi, r) \\ s(\theta, r)s(\phi, r) \\ c(\theta, r) \end{pmatrix} \tag{3.1}$$

where $s(\xi, r) = \text{sign}(\sin\xi)|\sin\xi|^r$, $c(\xi, r) = \text{sign}(\cos\xi)|\cos\xi|^r$, 'sign' is the signum function, d is the diameter of one particle and $r \in [0, 1]$ is a rounding parameter. For $r = 1$ the super-ellipsoid forms a sphere, for $r = 0$ it forms a cube. Fig. 3.3 shows a set of coupled super-ellipsoids for different rounding parameters.

3.3. Optical Properties

For the simulation of EEL spectra and extinction cross sections using the MNPBEM toolbox, the geometric structure and the material properties are the input parameters. The geometric structure of the nanoparticles is represented by the boundary elements. The material properties of the nanoparticles are represented by their dielectric functions.

Additionally, a tunnel conductivity has to be used for the implementation of the boundary QCM.

For the dielectric function of silver and gold we used experimental data of Johnson and Christy [42] and the Drude model in our simulations. A comparison of those dielectric functions is given in Fig. 2.5. An overall good agreement is found between the Drude model and the experimental data within the plotted range.

3.4. Parameters of the Drude Dielectric Functions

We also used the Drude dielectric function for silver and gold by utilizing Eqn. 2.88

$$\epsilon_r(\omega) = \epsilon_\infty - \frac{\omega_p^2}{\omega^2 + i\gamma_d\omega} \tag{3.2}$$

For gold the parameters $\epsilon_\infty = 10$, $\omega_p = 13.08$ eV and $\gamma_d = 0.066$ eV have been used. For silver the parameters $\epsilon_\infty = 3.3$, $\omega_p = 13.08$ eV and $\gamma_d = 0.022$ eV have been used.

3.5. Kretschmann and Otto Configurations

In this section we apply the Transfer-Matrix-Method in order to investigate surface plasmon polaritons. We investigate the Kretschmann and the Otto configuration.

3.5.1. Kretschmann Configuration

We consider a system consisting of three layers: glass, silver and air (see illustration on the left side of Fig. 2.1). The silver layer has a thickness of 50 nm and the glass has a constant dielectric function of $2.25 = 1.5^2$ (refractive index $n = 1.5$). An incoming transverse magnetic (TM) plane wave comes from the glass layer side. In Fig. 3.4 a density plot of the simulated absolute value of the electric field of a Kretschmann geometry has been plotted in dependence of angles and energies of an incoming plane wave. Experimental

data from Johnson and Christy [42] have been used for the dielectric function of silver. The layer-setup is glass - air (thickness 50 nm) - metal (thickness 50 nm) - air.

In the left plot the electric field at the glass-metal interface (corresponds to $z = 0$ nm in Fig. 3.5) and in the right plot the electric field at the metal-air interface (corresponds to $z = 50$ nm in Fig. 3.5) has been plotted. In the right plot one can see a plasmon resonance appear at an angle $\omega_1 = 41.8°$ of the incoming plane wave (for value of angle - see appendix A.6). The white line is positioned at $\omega_1 = 41.8°$.

The right plot of Fig. 3.4 highlights parameter configurations for which a surface plasmon polariton (SPP) can be excited for the Kretschmann geometry (see illustration on the left side of Fig. 2.1). This resonance curve states that below a certain energy of the incident plane wave, no SPP can be excited. For an increasing energy the resonance angle approaches asymptotically to a certain constant angle. In Fig. 3.5 the simulated absolute
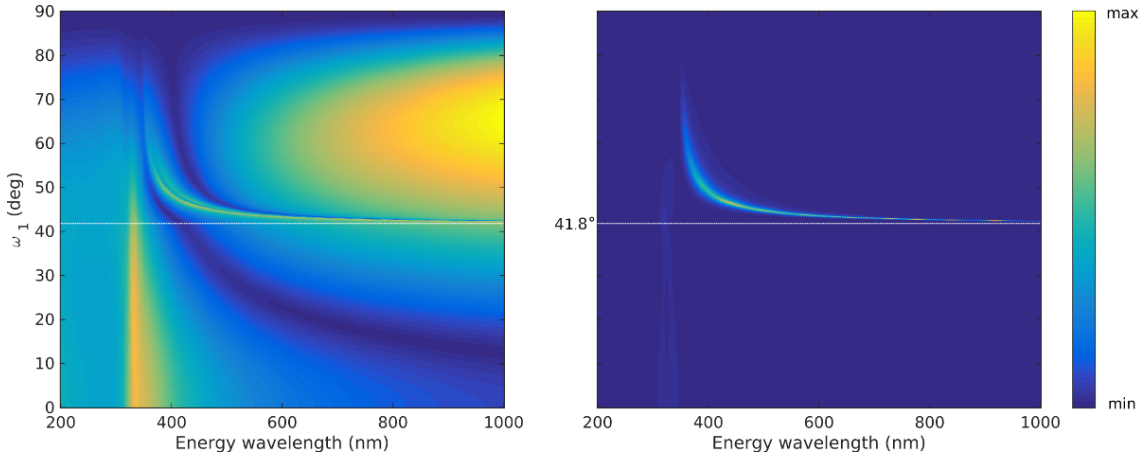
Figure 3.4.: Simulated absolute value of the electric field of a Kretschmann geometry (glass-silver-air). Left: Total energy at the glass-metal interface ($z = 0$ nm). Right: Total energy at the metal-air interface ($z = 50$ nm).

value of the electric field of a Kretschmann geometry for a fixed angle of $31°$ has been plotted.
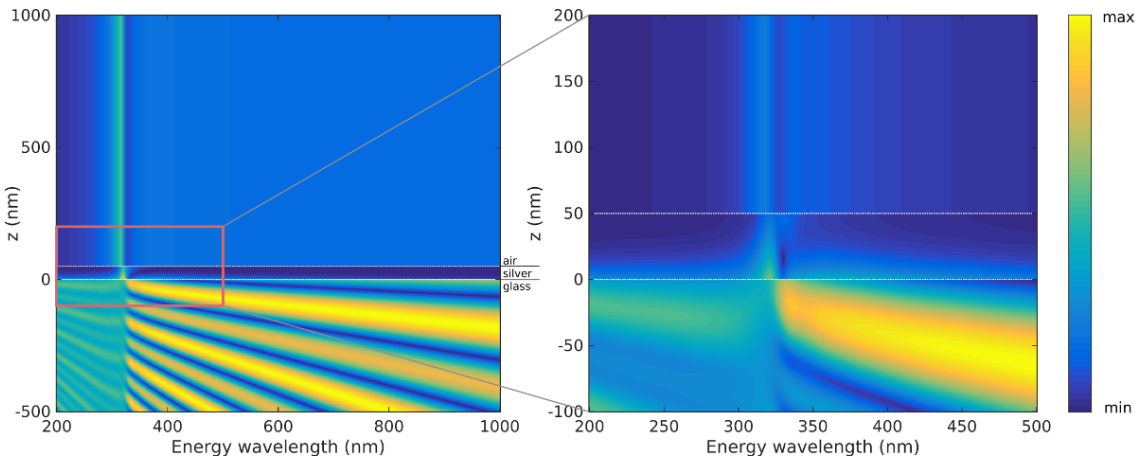
Figure 3.5.: Simulated absolute value of the electric field of a Kretschmann geometry (glass-silver-air) for an incoming plane wave with an angle of $41.8°$.

3.5.2. Otto Configuration

We consider a system consisting of four layers: glass, air, silver and air (see illustration on the right side of Fig. 2.1). The first air layer and the silver layer has both a thickness of 50 nm. The glass has a constant dielectric function of $2.25 = 1.5^2$ (refractive index $n = 1.5$). As in the Kretschmann geometry, an incoming transverse magnetic (TM) plane wave comes from the glass layer side. In Fig. 3.6 a density plot of the simulated absolute value of the electric field of an Otto geometry has been plotted in dependence of angles and energies of an incoming plane wave. Experimental data from Johnson and Christy [42] have been used for the dielectric function of silver. The layer-setup is glass - air (thickness 100 nm) - metal (thickness 50 nm) - air.

The glass-air interface is located at $z = 0$ nm. In the left plot the electric field at the air-metal interface (corresponds to $z = 100$ nm in Fig. 3.7) and in the right plot the electric field at the metal-air interface (corresponds to $z = 150$ nm in Fig. 3.7) has been plotted. In the right plot one can see a plasmon resonance appear at an angle $\omega_1 = 41.8°$ of the incoming plane wave. In Fig. 3.7 the simulated absolute value of the electric field of an
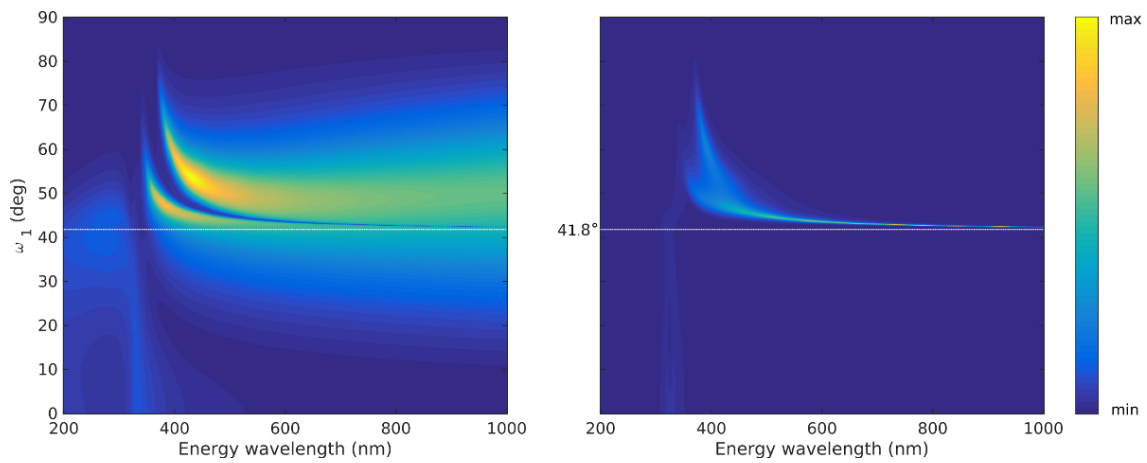
Figure 3.6.: Simulated absolute value of the electric field of an Otto geometry (glass-air-silver-air). Left: Total energy at the air-metal interface ($z = 100$ nm). Right: Total energy at the metal-air interface ($z = 150$ nm). The thickness of the air gap is 100 nm.

Otto geometry for a fixed angle of 41.8° has been plotted.
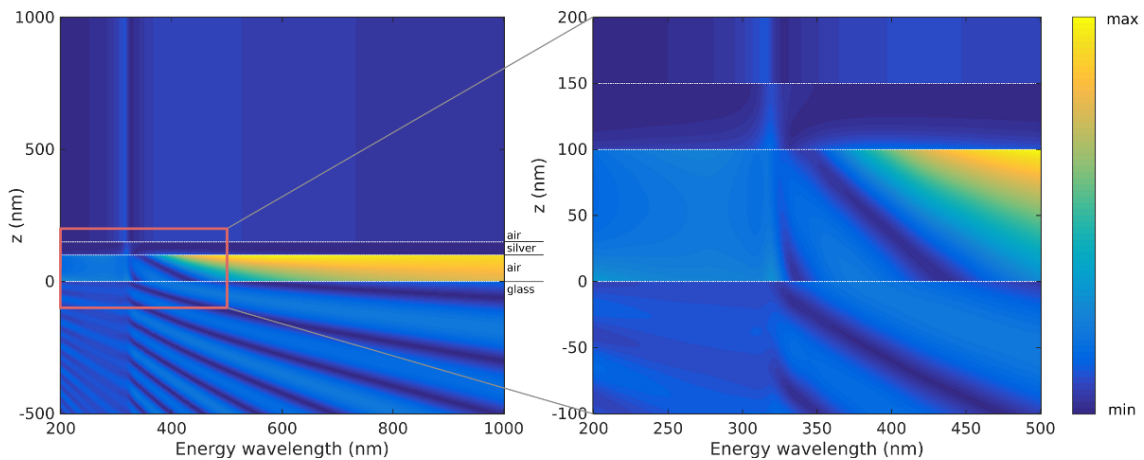
Figure 3.7.: Simulated absolute value of the electric field of an Otto geometry (glass-air-silver-air) for an incoming plane wave with an angle of 41.8°.

3.6. Electron Energy Loss and Extinction Simulations

Since numerical *ab-initio* calculations are very limited with respect to the particle size, we have also performed calculations using classical and semi-classical electromagnetic theories. For visualizing plasmonic resonances the BEM has been applied. As already pointed out in chapter 3.1, for that the Matlab toolbox MNPBEM has been used.

Our main interest is to investigate two coupled nanocubes and tunneling transfer plasmon oscillations. Nevertheless, we start with coupled nanospheres. There are several reasons. Beside the easier implementation of spheres compared to cubes and faster computational times, it has already been shown, that a tunneling transfer plasmon oscillation exists for two coupled nanospheres in reference [48]. Next, coupled nanocubes are simulated where rounded corners and edges are taken. In order to investigate the tunneling transfer plasmon oscillations, the gap conductivity has been treated as a parameter while a morphing of the nanoparticles has been considered.

3.6.1. Coupled Nanospheres

Sub-nanometer gaps of coupled Na and Au nanospheres have been theoretically investigated by Esteban et. al. in 2012 [44]. In order to compare this work with our results we start with coupled nanospheres and not directly with coupled nanocubes.

After checking convergence calculations with respect to the number of boundary elements for this system, we performed EEL and optical simulations of two approaching silver nanospheres each with a diameter of 35 nm. In Fig. 3.8 classical calculations are compared to semi-classical calculations where the boundary QCM has been applied. The parameters $\epsilon_\infty = 3.3$, $\omega_p = 9.175$ eV, $\gamma_p = 0.0212$ eV and $l_c = 0.042$ nm have been used for the dielectric function (Equ. 2.101) of the gap region (air/vacuum) between coupled silver spheres [47]. One can consider the classical simulations in the left column labeled with (a) as two coupled spheres with turned off electron tunneling and the semi-classical simulations in the right column labeled with (b) as two coupled spheres with turned on electron tunneling. In both columns the first three plots (1-3) are EEL simulated spectra. The insets in the plots show the impact position of the electron beam, highlighted by the red points. The plots labeled with (4) are optical extinction spectra. In the EEL simulations the simulated electron beam has a width of 0.5 nm. For the extinction plots the system is excited by a polarized plane wave, where the polarization is along the connection of the nanoparticles. In all subplots the Drude model has been used for the dielectric function of silver. The color corresponds to the energy loss probability of the electron beam or the optical excitation respectively. Regions with almost no energy loss (or extinction) are highlighted by the blue color. For regions with finite energy loss probability of the electron beam or the optical extinction the missing part of the energy has been adsorbed by the dimer and has excited a surface plasmon. In panel (2b) of Fig. 3.8 the separation distance of 0.20 nm has been highlighted, where electron tunneling starts to change the spectra drastically. In panel (2c) of Fig. 3.8 at an electron energy of 0.87 eV a new low-energy loss peak occurs in the short-separation distance regime. The plots labeled with (1) do not show the characteristic red-shifts of the other subplots in this figure, since the corresponding impact position lies in the symmetry plane between both particles [53].

Fig. 3.10 shows results of a QCM simulation where two coupled silver spheres are surrounded by a vacuum. In contrast to the previous figure the dielectric function of silver has been taken from experimental data measured by Johnson and Christy [42]. The difference of the Drude dielectric function and of the experimental dielectric function which has been taken can be viewed in Fig. 2.5.

In Fig. 3.9 simulated classical and QCM EEL and extinction spectra of two coupled gold nanospheres for different gap separation distances are plotted. Each of the spheres has a diameter of 35 nm. The Drude model has been used for the dielectric function of gold.
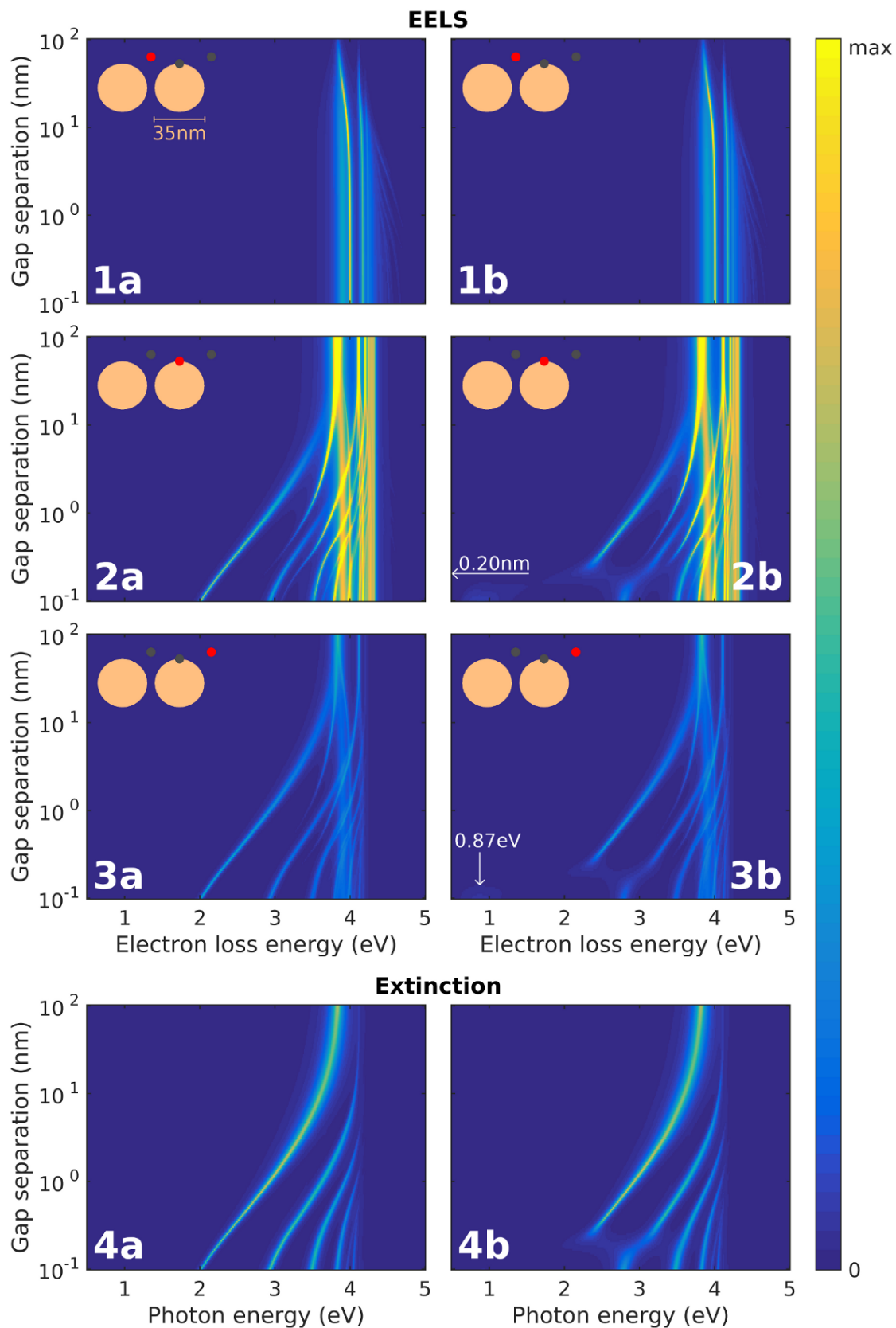
Figure 3.8.: (a) Classical and (b) QCM simulations of (1-3) EEL and (4) extinction spectra of two coupled **silver** spheres each with a diameter of 35 nm. For the dielectric function of silver the Drude model has been used. The surrounding medium and gap medium is vacuum. The inset figures in (1-3) highlight the impact positions of the electron beam.
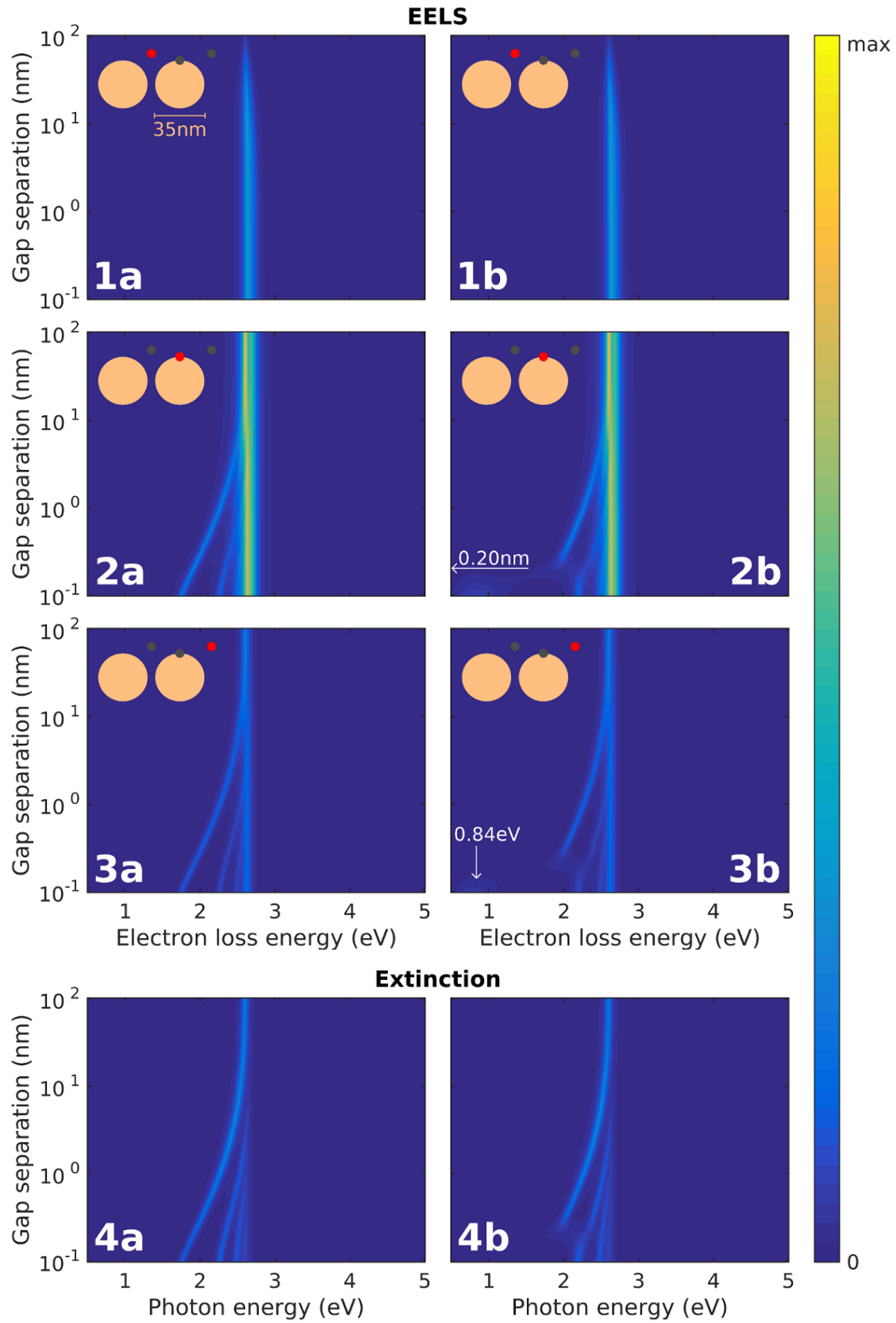
Figure 3.9.: Same as Fig. 3.8, but with gold spheres instead of silver spheres.
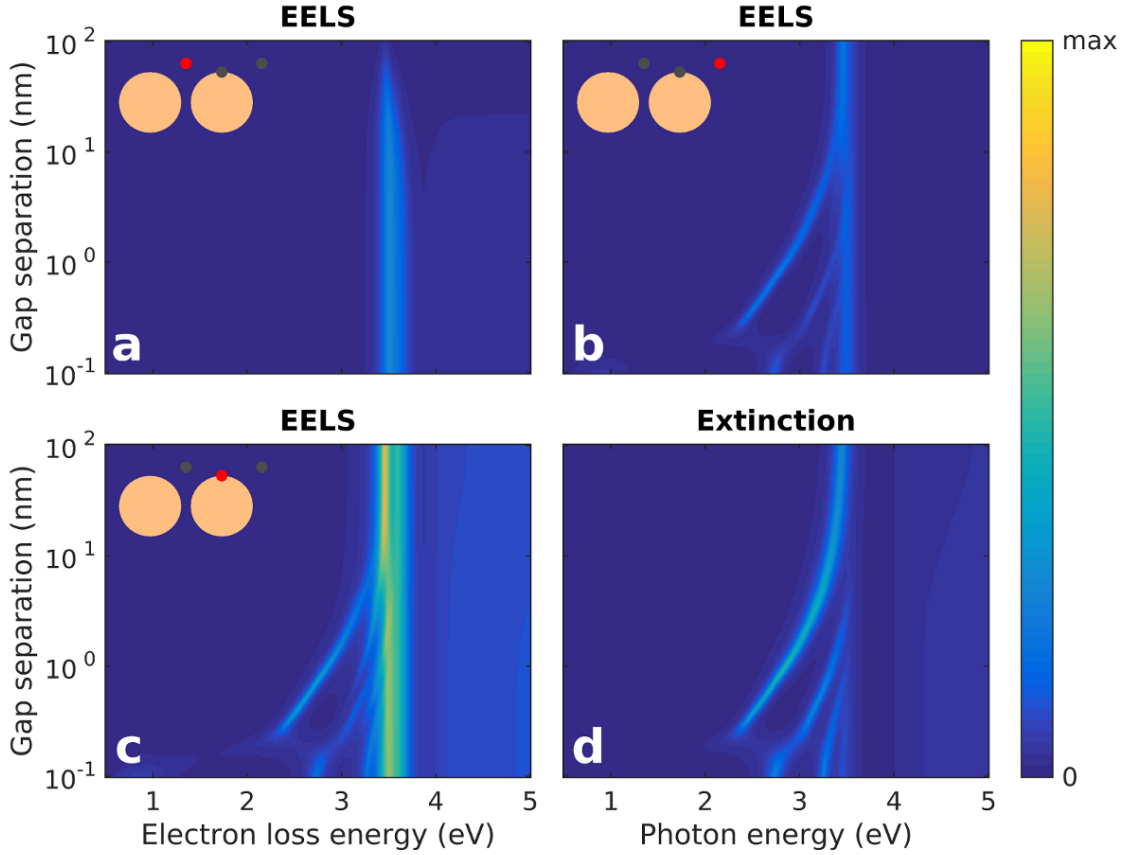
Figure 3.10.: QCM-simulation of (a-c) EEL and (d) extinction spectra of a dimer consisting of two **silver** cubes with a side length of 35 nm. Experimental data from Johnson and Christy [42] has been used for the dielectric function of silver. The surrounding medium and gap medium is vacuum. The inset figures in (a-c) highlight the impact positions of the electron beam.

The parameters $\epsilon_\infty = 10$, $\omega_p = 9.065$ eV, $\gamma_p = 0.0708$ eV and $l_c = 0.04$ nm have been used for the dielectric function (Equ. 2.101) of the gap region (air/vacuum) between coupled gold spheres [47]. In panel (2c) of Fig. 3.9 at an electron energy of 0.84 eV a new low-energy loss peak occurs at the short-separation distance region.

For gap widths larger than the diameter of a nanosphere the optical spectra and the EEL spectra of the coupled nanoparticles are in good agreement with those of a single nanosphere. Hence as expected, when comparing the classical calculations with those which are quantum corrected, for larger gaps, there is hardly any difference. The spectra start to differ at gap separation distances of 0.2 nm and below. For gap separation distances below 0.2 nm a resonance appears at an energy of 0.87 eV. This resonance can be identified as a tunneling charge transfer plasmon.

3.6.2. Coupled Nanocubes

For the next investigations we change the setup by switching from nanospheres to nanocubes. If not explicitly noted, each nanocube has a side length of 35 nm and a rounding parameter of 0.25.

Fig. 3.11 shows a comparison of classical and semi-classical simulations of two approaching silver nanocubes. For the dielectric function of silver the Drude model has been used. The boundary QCM has been implemented for the semi-classical simulations. The surrounding and gap medium is vacuum.
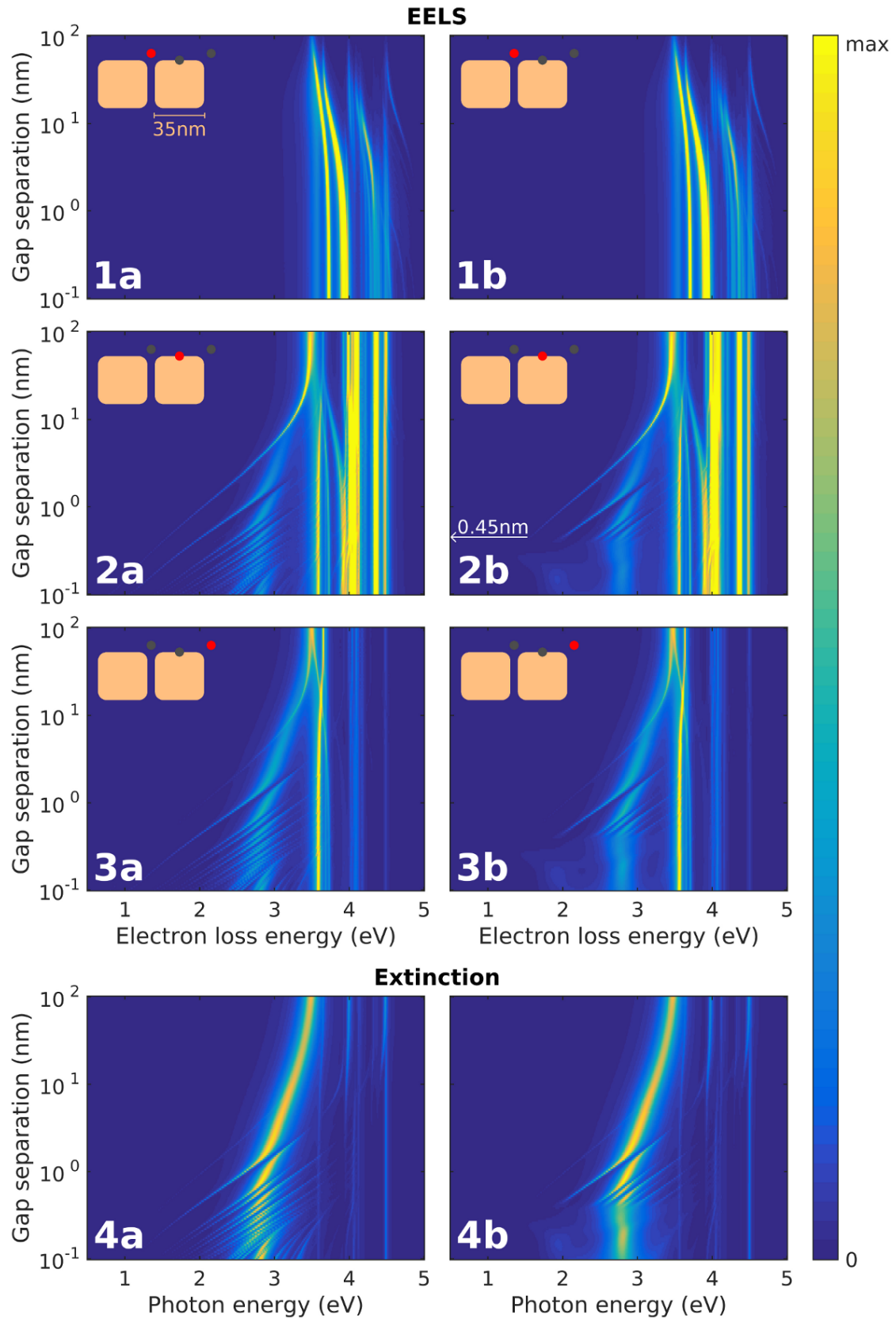
Figure 3.11.: Same as Fig. 3.8, but with silver cubes instead of silver spheres. The plots of panel (a) has been taken from [54].
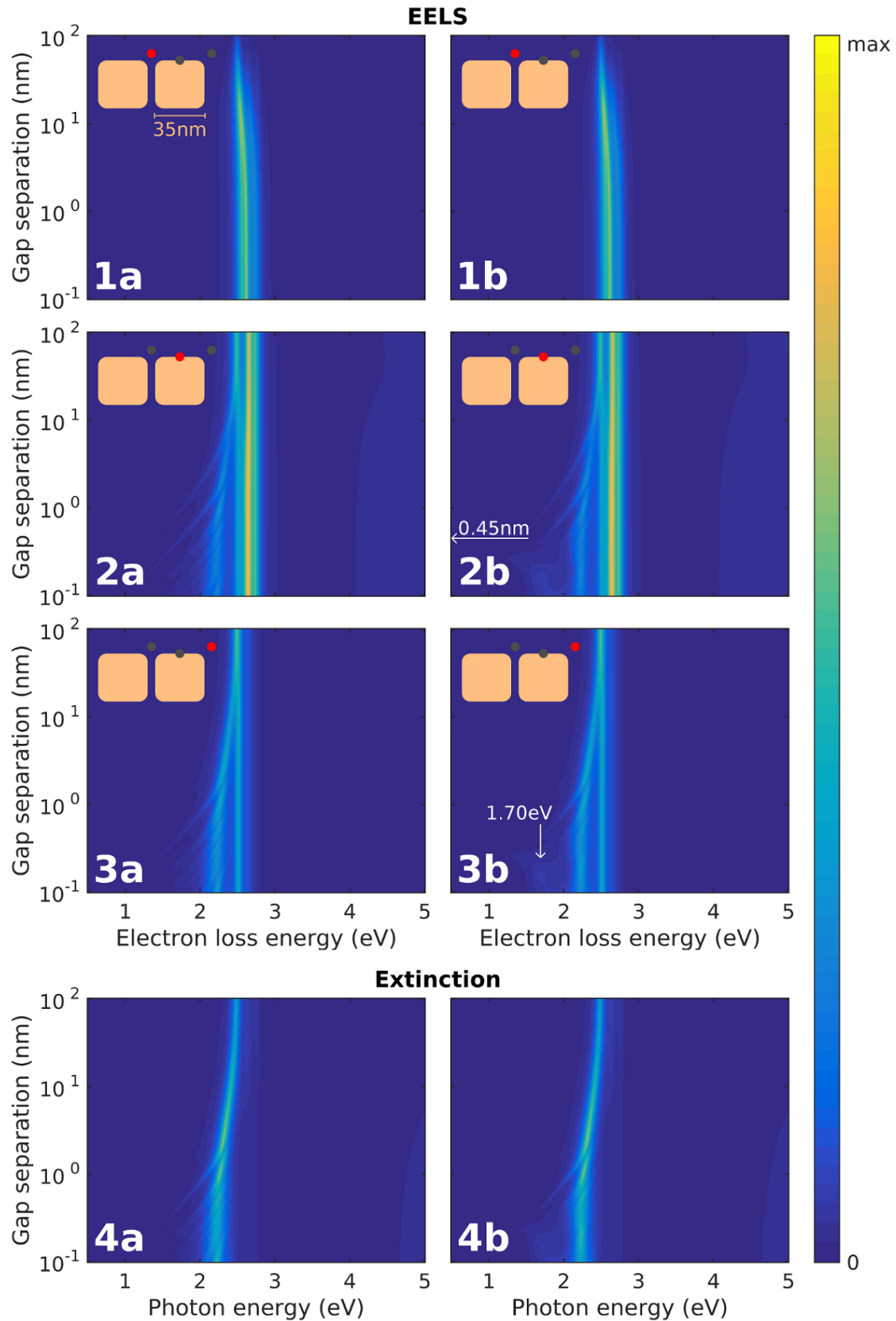
Figure 3.12.: Same as Fig. 3.8, but with gold cubes instead of silver spheres.

The parameters $\epsilon_\infty = 3.3$, $\omega_p = 9.175$ eV, $\gamma_p = 0.0212$ eV and $l_c = 0.042$ nm have been used for the dielectric function (Equ. 2.101) of the gap region (air/vacuum) between coupled silver cubes [47].

In panel (2b) of Fig. 3.11 the separation distance of 0.45 nm has been highlighted, where electron tunneling starts to change the spectra drastically.

Fig. 3.12 shows a comparison of classical and semi-classical simulations of two approaching gold nanocubes. For the dielectric function of gold the Drude model has been used. The parameters $\epsilon_\infty = 10$, $\omega_p = 9.065$ eV, $\gamma_p = 0.0708$ eV and $l_c = 0.04$ nm have been used for the dielectric function (Equ. 2.101) of the gap region (air/vacuum) between coupled gold cubes [47].

In panel (2b) of Fig. 3.12 the separation distance of 0.45 nm has been highlighted, where electron tunneling starts to change the spectra drastically. For separation distances larger than 0.45 nm there is no difference visible in the spectra of the classical and the QCM calculations. In panel (3b) of Fig. 3.12 a peak occurs at 1.70 eV for separation distances smaller than 0.45 nm in QCM calculated spectra.

3.6.3. Discussion

Since sharp edges can cause problems and inaccurate results when applying classical electrodynamic solvers, the corners and edges of the investigated nanocubes are rounded. The used geometrics of the nanocubes are described mathematically in Section 3.2.2. In detail, a super-ellipsoid with a rounding parameter $r = 0.25$ has been used for the simulated nanocubes.

Consider Fig. 3.11: For gap widths larger than the side length of a nanocube the optical spectra and the EEL spectra of the coupled nanoparticles are in good agreement with those of a single nanocube [55,56].

A red-shift of the longitudinal antenna plasmon (LAP) mode is given for a decreasing gap width [57].

For gap widths larger than 0.45 nm there is almost no difference in the spectra of the classical calculations and in the spectra of the quantum corrected calculations. For gap widths smaller than 0.45 nm a resonance appears at an energy of 1.9 eV. This resonance can be identified as a tunneling charge transfer plasmon, the same as for the coupled nanospheres, but at a higher energy.

In Fig. 3.11 (panel 2-4) anti-crossing of the red-shifted modes can be observed [54]. Notice that for two coupled nanospheres no obvious anti-crossing appears.

3.6.4. Gap Conductivity Variation

In order to simulate a class of different gap materials, in the next simulation the gap conductivity has been varied over a broad range from values below 10^2 S/m to values above 10^8 S/m. As a reference, the conductivity of aromatic 1,4-benzenedithiolates (BDT) is $2.49 \cdot 10^5$ S/m and the conductivity of saturated aliphatic 1,2-ethanedithiolates (EDT) is $9.16 \cdot 10^4$ S/m. Notice that the conductivity of silver is about $6 \cdot 10^7$ S/m.

In Fig. 3.13 EEL spectra of two coupled silver spheres and of two coupled silver cubes has been plotted. The gap conductivity has been set as a parameter. Throughout this simulation the gap separation distance has been set to 0.6 nm. The white areas in the insets of the Figure sketch the region where electron tunneling is possible. The Drude model has been used for the dielectric function of silver. Additionally selected charge surface distributions at specific energies are plotted, denoted with the capital letters (A-E). Here, the blue color denotes negative charge distributions and the yellow color denotes positive charge distributions. A transverse cavity mode [47] is present for mode **A**. The modes **B**, **C** and **D** are of higher order. Modes **B** and **C** are so-called transverse cavity modes. Mode
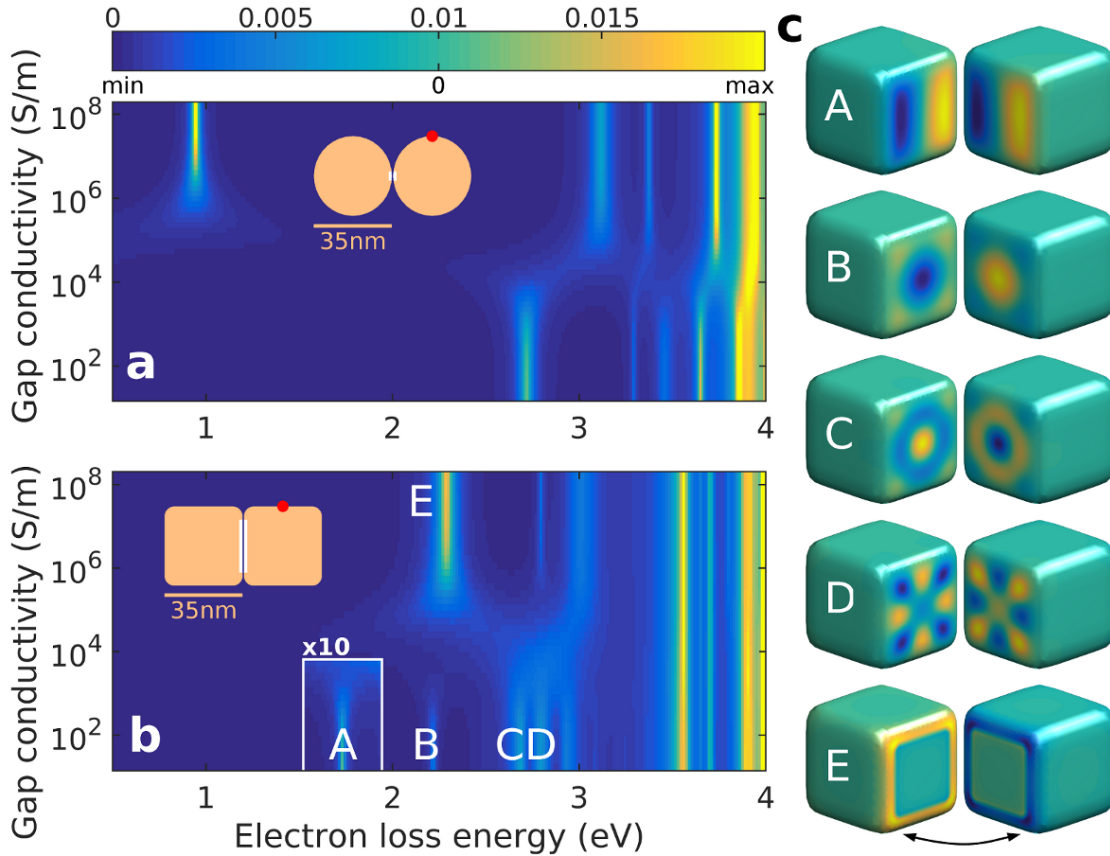
Figure 3.13.: Taken from reference [54]. Simulated density plots for EELS of **silver** (a) nanospheres and (b) nanocubes separated by a 0.6 nm gap. (c) Surface electron charge distribution plots corresponding to modes (A-E).

E can be identified as a tunneling Charge Transfer Plasmon (tCTP) resonance. It can be classified to be a longitudinal antenna mode [47].

In Fig. 3.14 the total charge of one sphere and the total charge of one cube, respectively, has been plotted. The total charge of the full system must be zero. As in the previous simulation the gap separation distance has been set to 0.6 nm and electron tunneling has been implemented by using the QCM for selected boundary elements in the gap region, highlighted by the white area in the insets of the Figure. Notice that for calculations without electron tunneling each nanoparticle's total charge is equal to zero. Hence by implementing electron tunneling one can detect plasmon resonances where electron tunneling is crucial. For comparable large conductivities the lowest-energy plasmon mode shows the most prominent peak in the density plot. For comparable small conductivities there is no noticeable point in the density plot. Since for such small conductivities electron tunneling is suppressed, a classical behavior is expected. In Fig. 3.15 EEL spectra for different gap conductivities of (a) two coupled gold spheres and of (b) two coupled gold cubes have been plotted. Two different electron beam impact positions, for each plot sketched in the inset, has been simulated. The impact position used in the sub-figures (a) and (c) is asymmetric in the direction perpendicular to the gap surface and symmetric in the direction parallel to the gap surface. The impact position used in the sub-figures (b) and (d) is asymmetric, both, in the direction perpendicular to the gap surface and in the direction parallel to the gap surface. A constant gap separation distance of 0.6 nm has been used. The white area in the insets of the figure sketches the region where electron tunneling is possible.
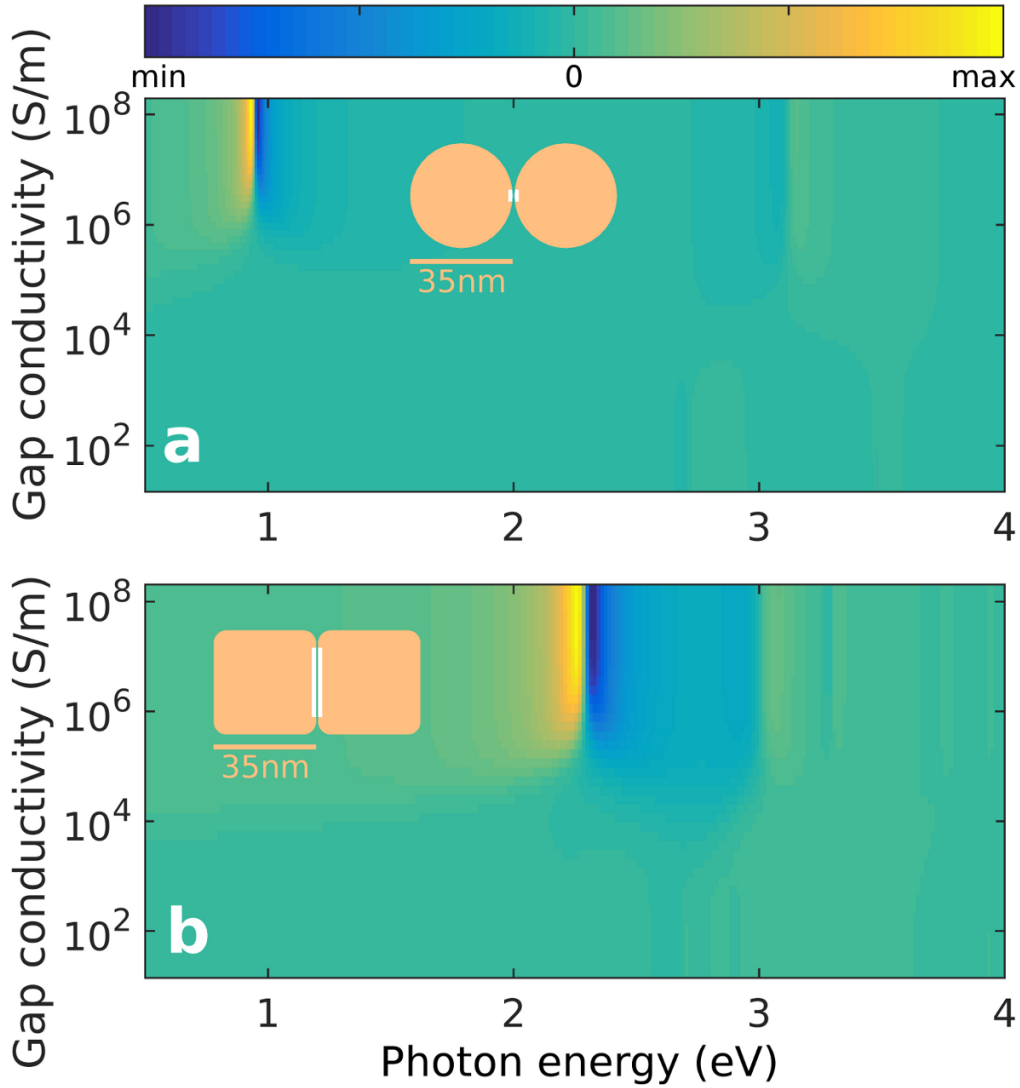
Figure 3.14.: Simulated density plots of two coupled **silver** (a) nanospheres and (b) nano-cubes separated by a 0.6 nm gap. The density denotes the total charge of the left nanoparticle (colorbar). Optical plane wave excitation has been used.

3.6.5. Discussion

The transverse cavity mode, highlighted in panel (c) of Fig. 3.13 by the label **A** can only occur for electron beam impact positions which are asymmetrical in the direction perpendicular to the gap surface. In accordance, the EEL spectra in panel (d) of Fig. 3.15 does show such a resonance, while the EEL spectra in panel (c) of Fig. 3.15 does not show such a resonance.

Additionally, the total charge of one particle has been plotted in Fig. 3.14. The density plot highlights the plasmon mode where electron charge tunneling takes place.

While the tCTP mode is the most prominent peak, also higher modes have small contributions of electron tunneling.
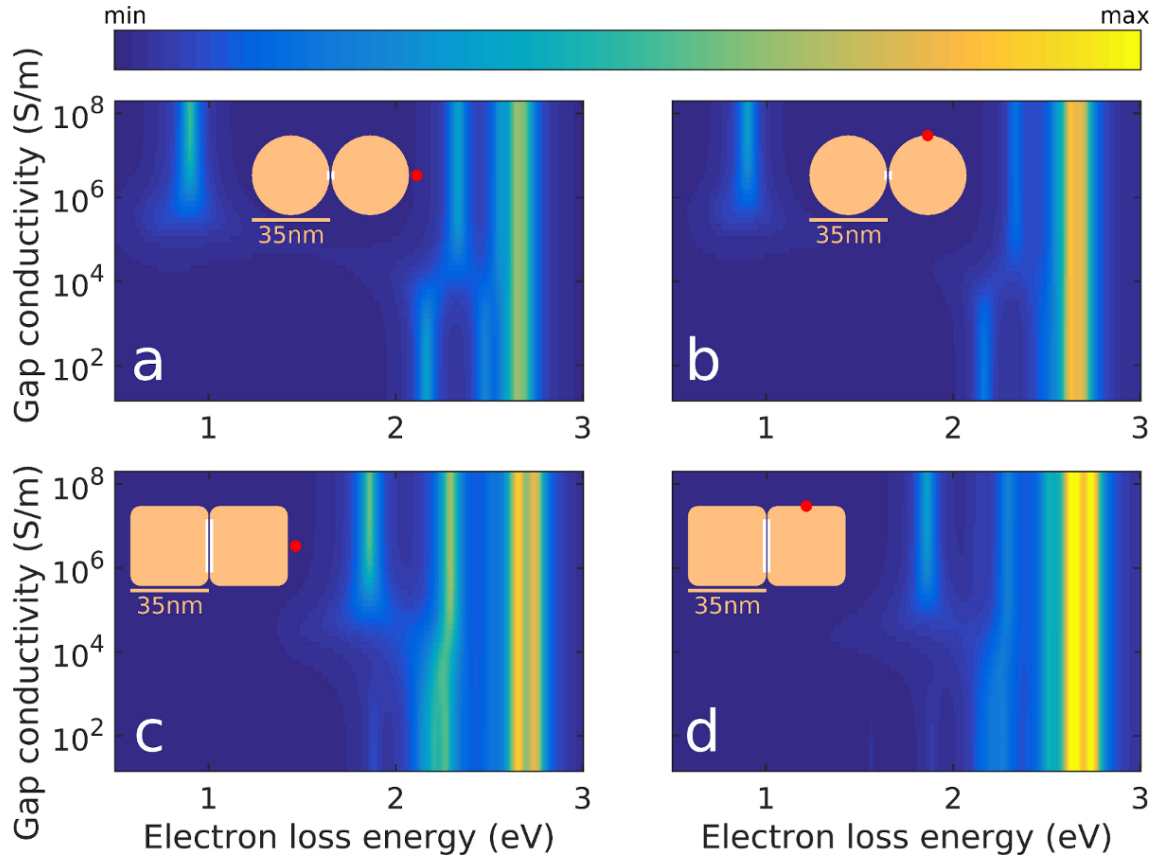
Figure 3.15.: Simulated density plots for EELS of **gold** (a-b) nanospheres and (c-d) nano-cubes separated by a 0.6 nm gap.

3.6.6. Morphing

The previously plotted EEL spectra and extinction spectra of the investigated dimers show differences concerning tunneling charge plasmons. For nanospheres there occurs a low-energy peak in the spectra, but not for nanocubes. In order to investigate the absence of a low-energy tunneling charge plasmonic resonance, we perform a continuous transition from two coupled spheres to two coupled cubes and study the low-energy resonance. We exploit the concept of super-ellipsoids discussed in Chapter 3.2.2 for the morphic transition. Hence, to shape continuously from spheres to cubes we decrease the rounding parameter from $r = 1$ to about $r = 0.25$. In panel (a) of Fig. 3.16 a simulated extinction spectrum for a rounding parameter variation of two coupled silver super-ellipsoids having each a diameter of 35 nm has been plotted. The boundary elements in the gap region has been enabled for electron tunneling by applying boundary QCM. In panel (b) of Fig. 3.16 a simulated extinction spectrum for a single nano-cuboid with a long-side of 70 nm and a short-side of 35 nm is plotted. The particle of panel (b) can be viewed as two connected nanocubes where each has a side length of 35 nm. The prominent peak positioned at approximately 2.7 eV is caused by a plasmonic dipole mode. In both panels of the figure the Drude model has been used for the dielectric function of silver. The material placed in the gap region consist of BDT. It has approximately the thickness of one layer of BDT, namely 0.6 nm, which has been taken from reference [9]. For the gap conductivity $\sigma = 2.49 \cdot 10^5$ S/m has been used, also taken from reference [9].

One of the most important results of Fig. 3.16 concerning the tunneling transfer plasmon resonances is the blue-shift of the tunneling mode for a decreasing rounding parameter. Another important result is that there does not occur a plasmon resonance at energies smaller than this tunneling plasmon mode. We performed the same simulation for gold
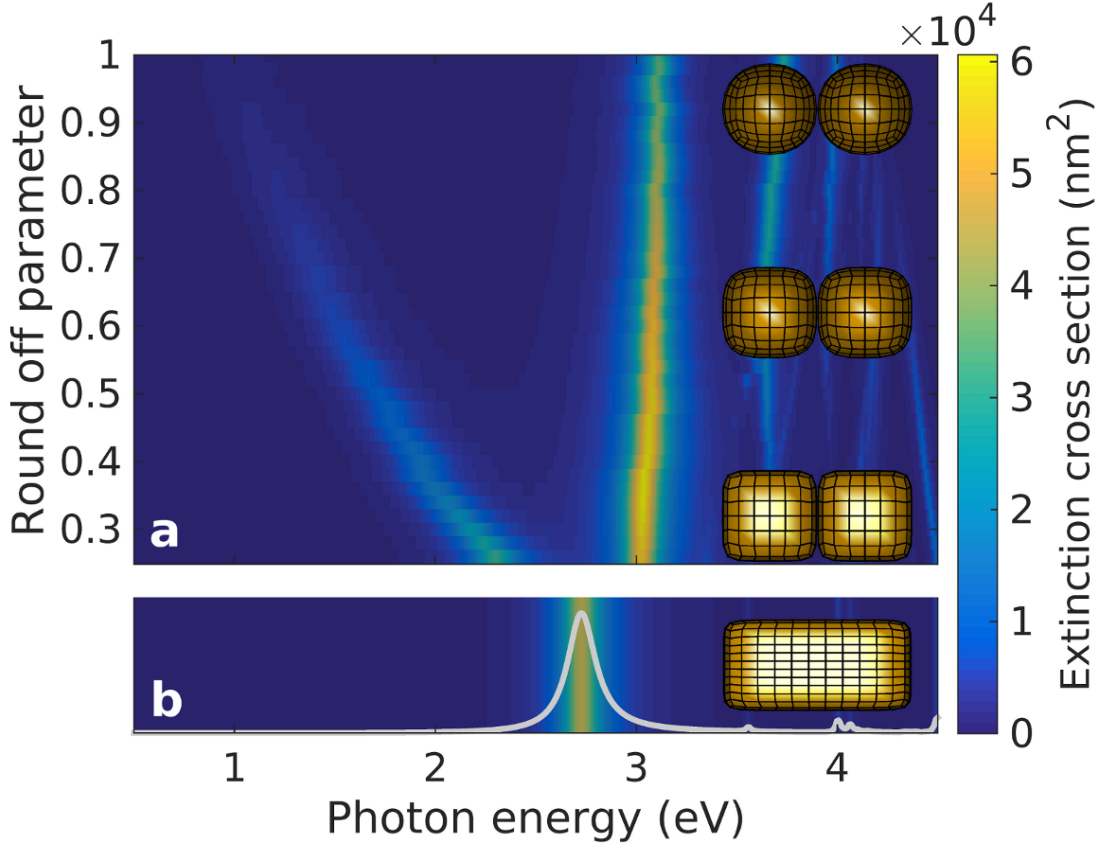
Figure 3.16.: Taken from reference [54]. (a) Simulated extinction density plot. A morphic transition from two spheres (round off parameter = 1) to two cubes. The coupled **silver** nanoparticles are separated by a distance of 0.6 nm. The gap conductivity is $2.49 \cdot 10^5$ S/m representing BDT molecules. (b) Simulated extinction spectrum for a **silver** cuboid with side length 70 nm.

particles instead of silver particles, where all other parameters are the same. The results of the gold particles are plotted in Fig. 3.17. Panel (a) of Fig. 3.17 shows a simulated EEL spectrum for a rounding parameter variation of two coupled gold super-ellipsoids. Each super-ellipsoid has a diameter of 35 nm. In panel (b) of Fig. 3.17 a simulated EEL spectrum for a single gold nano-cuboid with a long-side of 70 nm and a short-side of 35 nm is plotted.

In contrast to the results of Tan et. al [9], there is no tunneling charge plasmon resonance in the low-energy range at coupled nanocubes in our simulations. In order to point out (theoretical) possibilities when such low-energy resonances could occur we first consider a Drude-like gap-conductivity. In Fig. 3.18 a density plot of an EEL simulation of a morphic transition from spheres to cubes is shown where a non-constant Drude-like gap-conductivity $\sigma(\omega) = \frac{\sigma_0}{1 - i\omega\tau}$ (see Eqn. 2.83) has been taken. The static conductivity has been set to $\sigma_0 = 2.49 \cdot 10^5$ S/m and the relaxation time has been set to $\tau = 30$ fs. The diameter of the super-ellipsoids has been set to constant 35 nm. As in previous simulations, the coupled particles are separated by a distance of 0.6 nm. In Fig. 3.19 a simulated extinction cross section plot is plotted corresponding to the same setup as in Fig. 3.18.

3.6.7. Discussion

Since for coupled nanospheres low-energy plasmon modes exists, but not for flat gap boundaries, a morphic transition has been performed to demonstrate that the low-energy mode blue-shifts for morphing the spheres to cubes.
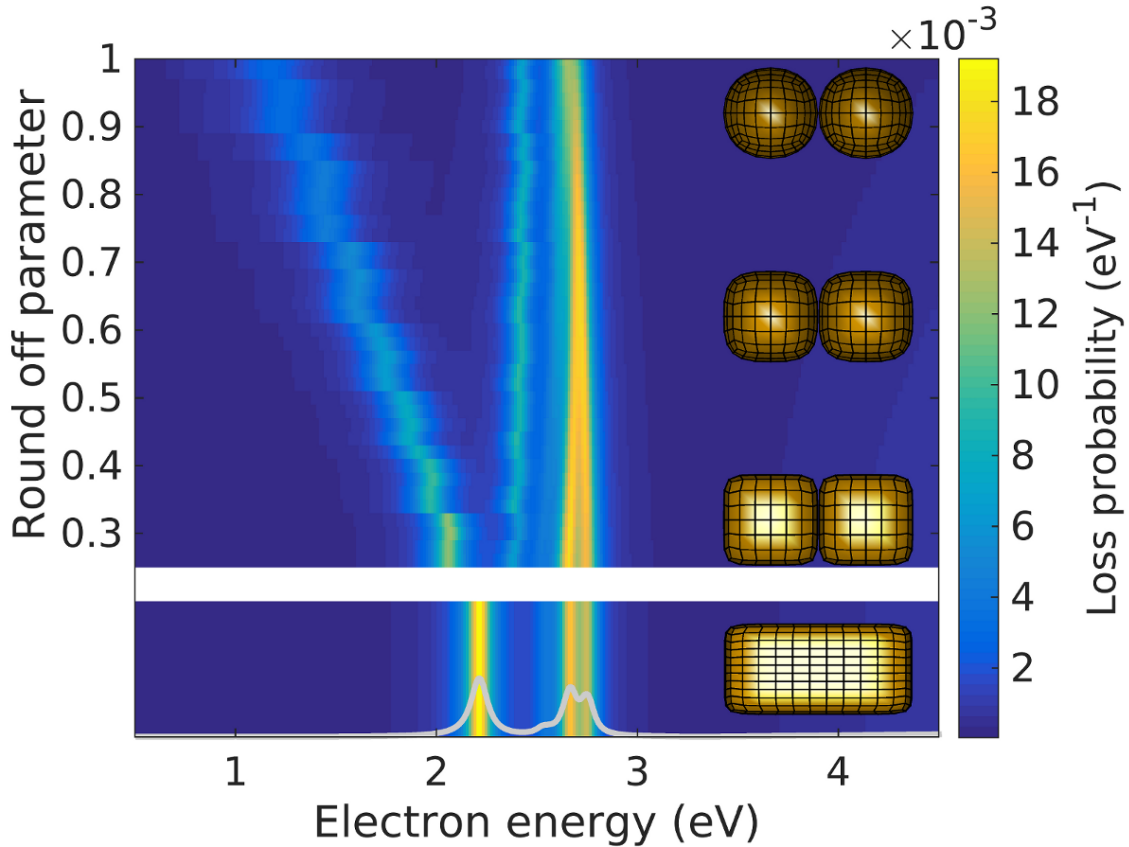
Figure 3.17.: Same as Fig. 3.16, but with **gold** nanoparticles.

Additionally, instead of a static conductivity a frequency-dependent conductivity that corresponds to a Drude-like dielectric function has been used in Fig. 3.18. There are several reasons [54] that the usage of a frequency-dependent conductivity is wrong for such a system [54]. The gap-material is not a metal or a conductor. Hence it should not be described by a Drude model. Another reason is the usage of the collision time τ. Since in a tunnel process there is no collision expected, it is not justified to use this parameter. Further, for the case that the gap-conductivity would be frequency-dependent, we showed in Fig. 3.13 that a change of the gap-conductivity would not have an impact to the energy of a plasmon peak. A change of the gap-conductivity determines the occurrence of a peak but does not affect its resonance frequency.
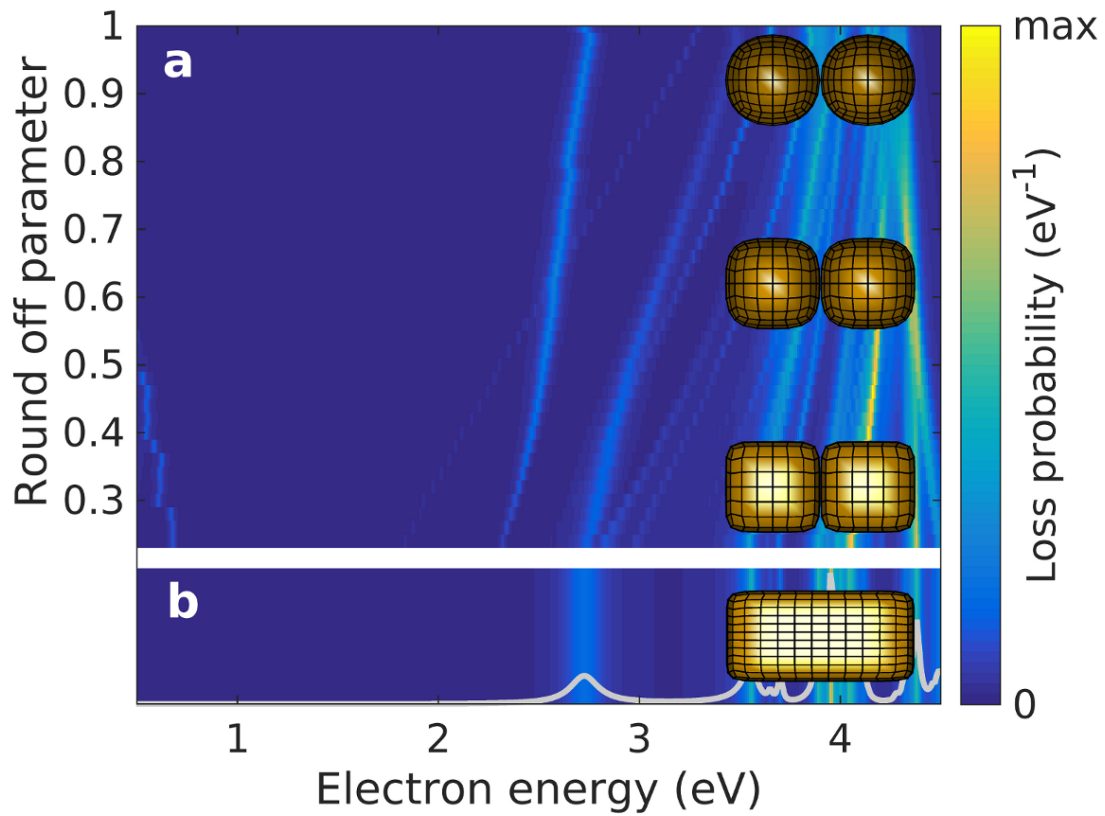
Figure 3.18.: (a) Simulated EEL spectra for a morphic transition from coupled nanospheres to coupled nanocubes. The silver nanoparticles are separated by a distance of 0.6 nm. A non-constant Drude-like gap-conductivity has been taken. (b) Simulated EEL spectrum for a **silver** cuboid with side length 70 nm.
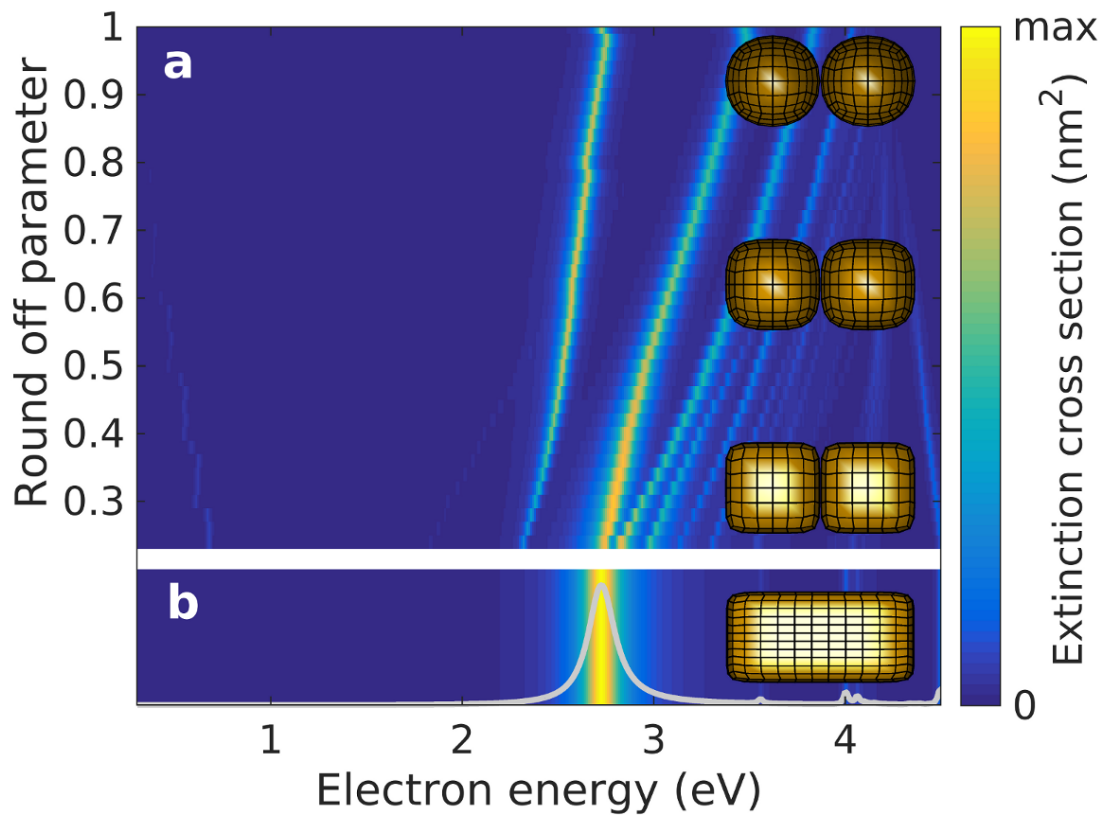
Figure 3.19.: Same as Fig.3.18, but showing the extinction spectra instead of the EEL spectra.

3.6.8. Roughness

In order to investigate another possible reason for a low-energy tunneling charge transfer plasmon, a rough surface of the silver nanocubes in the gap region is simulated. A roughness of a surface can be described via a two-dimensional height-function [4,58]

$$h(x,y) = \frac{\sigma^2}{2\pi} \operatorname{Re} \left\{ \mathcal{F}^{-1} \left(e^{-\frac{\sigma^2}{2}(k_x^2 + k_y^2)} e^{i2\pi\phi} \right) - \frac{1}{2} \right\} \tag{3.3}$$

where $\mathcal{F}^{-1}$ is the inverse Fourier-Transformation, σ is a parameter to control the strength of the roughness, ϕ is a random number, and the wave vector components are $k_x = \frac{2\pi}{x}$ and $k_y = \frac{2\pi}{y}$. The variables x and y are the coordinates of the surface position. The height-function represents the z coordinate of the randomly generated surface. The case of an overall $h = 0$ corresponds to a surface with no roughness. One can add such a height-function on top of an existing surface, e.g. to one side of a nanocube.

In Fig. 3.20 an extinction cross section plot of two coupled silver nanocubes with a rough gap conductivity is given. For the random numbers ϕ the Matlab function *rand* has been used.
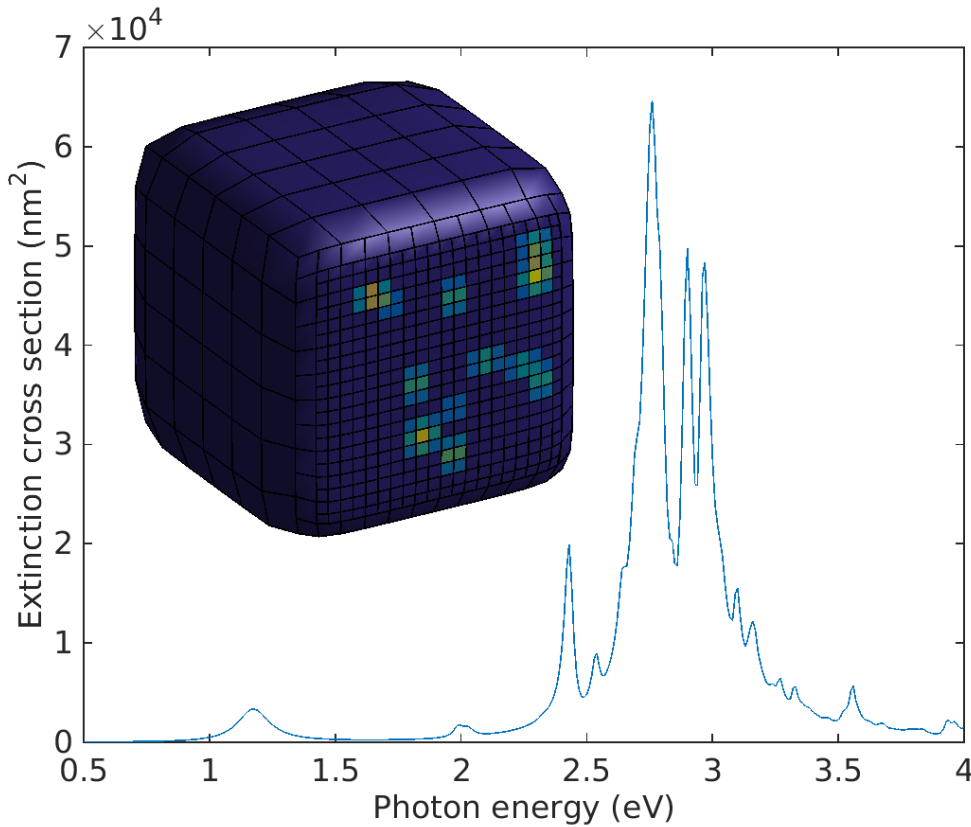
Figure 3.20.: Extinction cross section plot of two coupled **silver** nanocubes. A gap conductivity with simulated roughness has been taken by utilizing Eqn. 3.3.

The energy position of the low-energy plasmon mode depends on the size of the roughness peaks.

3.6.9. Normal distributed Gap Conductivity

In Fig. 3.21 simulated extinction spectra of a normal distributed gap conductivity for varied peak positions are plotted. It shows that the position of a roughness peak can change the
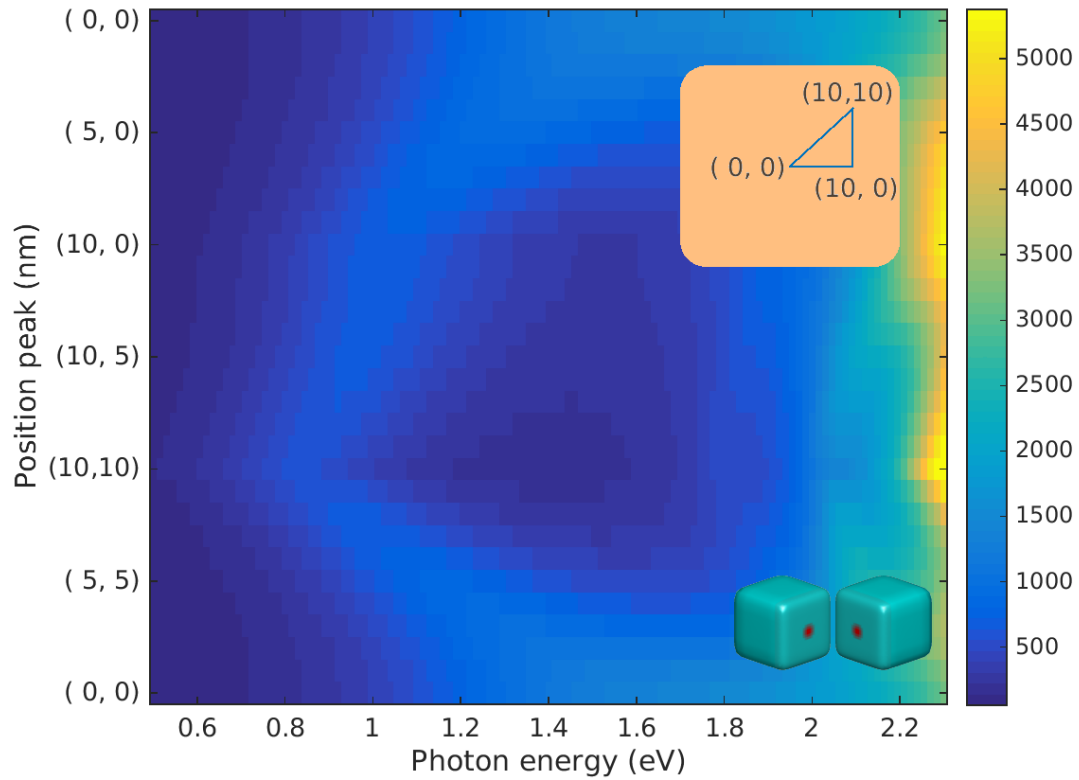
Figure 3.21.: Simulated extinction spectra for a normally distributed gap conductivity with varied distribution peak locations of two coupled **silver** nanocubes.

resonance frequency of the low-energy plasmon mode. A peak in the center of the gap surface has a higher energy position than a peak outside the center.

4. DFT Simulations - Molecular Tunnel Junction - Theory

This chapter collects the most important theories, methods and some basic ideas which have been used for the quantum transport based simulations in this thesis. Starting with a brief introduction to quantum mechanics regarding the Schrödinger equation leading to density functional theory. Further transport theory is introduced by the usage of a non-equilibrium Green's function technique.

4.1. Quantum Mechanics

Quantum mechanics is a theory based on a few principles to describe properties of small particles (nanoparticles). One of the most important properties of nanoparticles are the dynamics of electrons. Physical properties of ordinary matter is determined by interactions between constitutional atomic nuclei and electrons, by interactions between nuclei and nuclei, and by interactions between electrons and electrons. Since masses of atomic nuclei are considerably larger than masses of electrons, it is common to apply the Born-Oppenheimer approximation which allows to consider electronic dynamics separately by fixing the positions of the atomic nuclei [59]. In quantum mechanics, the electron dynamics is described by the Schrödinger[1] equation [60].

$$i\hbar\frac{\partial}{\partial t}\Psi = \hat{H}\Psi \tag{4.1}$$

The Hamiltonian[2] of the Schrödinger equation of a many-electron system reads [61,62]

$$\hat{H} = -\frac{\hbar^2}{2m}\sum_{i=1}^{N}\bigtriangledown_i^2 + \frac{e^2}{2}\sum_{i=1}^{N}\sum_{j\neq i}^{N}\frac{1}{|\mathbf{r}_i - \mathbf{r}_j|} + \sum_{i=1}^{N}v(\mathbf{r}_i) \tag{4.2}$$

where the first term is the kinetic part, the second term is the electron-electron interaction part, and the third term is the external potential, which contains the electric charges of the (fix-positioned) atomic nuclei. With the ansatz

$$\Psi(\mathbf{r}_1,\mathbf{r}_2,...,\mathbf{r}_N,t) = \psi(\mathbf{r}_1,\mathbf{r}_2,...,\mathbf{r}_N)e^{-iEt/\hbar} \tag{4.3}$$

one can separate the N-electron-wavefunction into a spatial part and a temporal part. The stationary Schrödinger equation corresponds to the spatial part and is given by

$$\hat{H}\psi(\mathbf{r}_1,\mathbf{r}_2,...,\mathbf{r}_N) = E\psi(\mathbf{r}_1,\mathbf{r}_2,...,\mathbf{r}_N). \tag{4.4}$$

where the spatial N-electron-wavefunction ψ is the fundamental quantity of a stationary quantum system.

---

[1]Erwin Rudolf Josef Alexander Schrödinger, Austrian physicist, *1887, +1961.
[2]Sir William Rowan Hamilton, Irish physicist, astronomer, and mathematician, *1805, +1865.

4.2. Density Functional Theory

For a stationary, quantum mechanical N-electron system, which can be usually described by the stationary Schrödinger equation, the corresponding N-electron-wavefunction ψ consists of $3N$ spatial parameters, being the coordinate parameters of all N electrons. $3N$ becomes quite a huge number for a usual solid - remember the Avogadro constant - even for a nanoparticle.

In contrast the electron density of such a N-electron system

$$
\begin{aligned}
n(\mathbf{r}) &= \frac{1}{(N-1)!} \int_{\mathbb{R}^{3(N-1)}} N! |\psi(\mathbf{r}, \mathbf{r}_2, ..., \mathbf{r}_N)|^2 d^3 r_2 \ldots d^3 r_N \\
&= N \int_{\mathbb{R}^{3(N-1)}} |\psi(\mathbf{r}, \mathbf{r}_2, ..., \mathbf{r}_N)|^2 d^3 r_2 \ldots d^3 r_N
\end{aligned} \tag{4.5}
$$

has only 3 coordinate parameters. The factorial numbers from the previous equation arise from fermion statistics.

The Density Functional Theory (DFT) uses the electron density as the fundamental quantity rather than the wavefunctions (as it is usually the case when solving the stationary Schrödinger equation). This leads to a reduction of the number of parameters from $3N$ to 3, regarded as a great benefit of the DFT.

The total energy of the many-electron system is a functional of the electron density [63].

$$
E = E[n] \tag{4.6}
$$

4.2.1. First and Second Hohenberg-Kohn Theorems

The following two theorems, the Hohenberg[3]-Kohn[4]-theorems, form the basis on which DFT relies on. Usually a potential of a quantum mechanical system determines the wavefunction which determines the electron density. Could it be vice versa?

> **1st Hohenberg-Kohn theorem**
>
> Aside from an additional constant the potential is uniquely determined by a given electron density [63].
>
> $$ n(\mathbf{r}) \Longrightarrow v(\mathbf{r}) \tag{4.7} $$

The original proof of this theorem is performed by *Proof by contradiction*, a standard technique for showing uniqueness.

We consider the set $\{\psi \to n\}$, containing all N-electron wavefunctions that correspond to the same electron density n. When minimizing the term $\langle \psi | \hat{H} | \psi \rangle$ by varying over all wavefunctions of this set, one gets the total energy $E[n]$ [64].

$$
E[n] = \min_{\{\psi \to n\}} \langle \psi | \hat{H} | \psi \rangle \tag{4.8}
$$

By using $\hat{H} = \hat{T} + \hat{V}_{ee} + \hat{V}_{ext}$ one usually splits the total energy into a universal and a specific part. The universal part reads [64]

$$
F[n] = \min_{\{\psi \to n\}} \langle \psi | \hat{T} + \hat{V}_{ee} | \psi \rangle \tag{4.9}
$$

---

[3] Pierre C. Hohenberg, French-American physicist, *1934.
[4] Walter Kohn, Austrian-born American physicist, *1923, +2016.

and the specific part reads

$$\min_{\{\psi \to n\}} \langle \psi | \hat{V}_{ext} | \psi \rangle = \min_{\{\psi \to n\}} \int v(\mathbf{r}) n(\mathbf{r}) d^3 r. \tag{4.10}$$

When minimizing the total energy one gets the ground state energy [64]

$$E_0 = \min_n E[n] = \min_n \left(F[n] + \int v(\mathbf{r}) n(\mathbf{r}) d^3 r \right) \tag{4.11}$$

> **2nd Hohenberg-Kohn theorem**
>
> The total energy of the many particle system is minimized by the ground state density [63].

4.2.2. Kohn-Sham Equations

Both Hohenberg-Kohn theorems do not provide a scheme to solve the Schrödinger equation, more precisely, finding the ground state energy. In order to obtain a scheme one can introduce a set of (mathematically) non interacting electrons [65]. Since the electrons are not interacting, the total density is simply the sum of the squares of the absolute values of all occupied one-electron waves functions.

$$n(\mathbf{r}) = \sum_i f_i^{\text{occ}} |\phi_i(\mathbf{r})|^2 \tag{4.12}$$

The occupation function f_i^{occ} is usually a step function [62]. For the case of non-interacting particles the Schrödinger equation can be separated into stationary one-electron Schrödinger equations, the so-called Kohn-Sham[5] equations [62,65]

$$\hat{H}_{KS} \phi_i(\mathbf{r}) = \epsilon_i \phi_i(\mathbf{r}) \tag{4.13}$$

where the Hamiltonian reads

$$\hat{H}_{KS} = -\frac{\hbar^2}{2m} \bigtriangledown_i^2 + v_{KS}(\mathbf{r}). \tag{4.14}$$

The Kohn-Sham potential reads

$$v_{KS}(\mathbf{r}) = v_{ext}(\mathbf{r}) + v_H(\mathbf{r}) + v_{xc}(\mathbf{r}) \tag{4.15}$$

where the first term is the external contribution $v_{ext}(\mathbf{r})$, given at least by the electron-nuclei interaction. The second term is the Hartree potential

$$v_H(\mathbf{r}) = \int \frac{n(\mathbf{r}')}{|\mathbf{r} - \mathbf{r}'|} d^3 r' \tag{4.16}$$

accounting for the classical electron-electron interaction. The third term is the exchange-correlation potential given by the functional derivative of the exchange-correlation energy E_{xc}

$$v_{xc}(\mathbf{r}) = \frac{\delta E_{xc}}{\delta n(\mathbf{r})}. \tag{4.17}$$

A consistent theory is achieved by using effective potentials for each one-electron equation such that the whole system leads to the same results as the physical one. Hence the way of incorporating electron-electron interactions is by including it in the (effective) potentials.

---

[5]Lu Jeu Sham, Chinese-American physicist, *1938.

4.2.3. Exchange-Correlation Approximations

All parts of the energy functional except the exchange-correlation energy are known. Hence for practical calculations, approximations of the exchange-correlation contribution are needed to solve the Kohn-Sham equations.

One of the simplest approximations is the local density approximation (LDA) [62,65,66]. In this approximation the electrons are considered to form an electron gas having a uniform distributed electron density.

$$E_{xc}^{LDA}[n] = \int n(\mathbf{r}) \cdot e_{xc}(\mathbf{r}) d^3 r \tag{4.18}$$

where $e_{xc}(\mathbf{r})$ is the exchange-correlation energy per electron [62,67–69].

A more accurate approximation (or better type of approximation), which is widely used, is given by the generalized gradient approximation (GGA) [70–73].

$$E_{xc}^{GGA}[n] = \int f_{xc}(n, \nabla n) d^3 r \tag{4.19}$$

where the approximated function f depends on the density and on the gradient of the density ∇n.

4.2.4. Kohn-Sham Algorithm
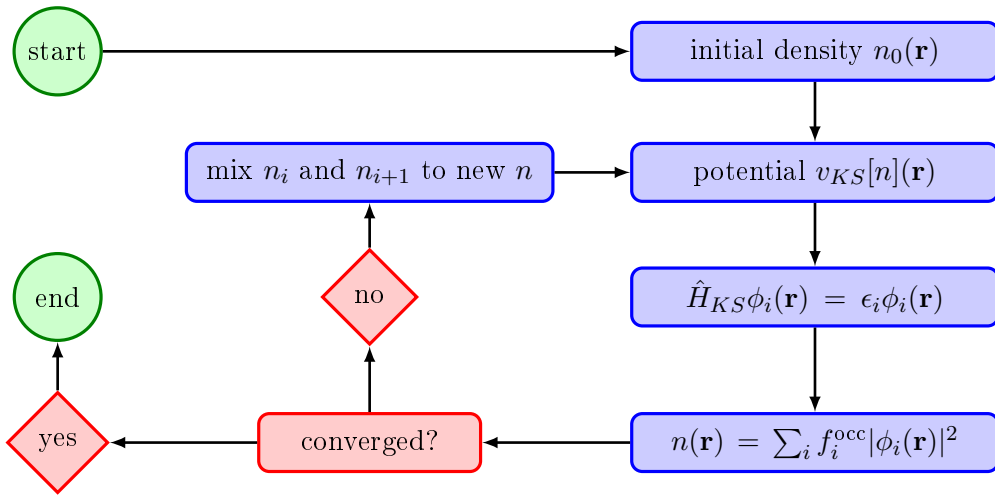
Figure 4.1.: The self-consistent Kohn-Sham Algorithm solving the stationary Schrödinger equation of a many electron system.

The Kohn-Sham equations can be solved in a self-consistent manner which is known as the Kohn-Sham algorithm, depicted in Fig. 4.1. The algorithm scheme goes as follows: One starts with an initial guess of the electron density. For a given density one can compute the effective Kohn-Sham potential $v_{KS}[n](\mathbf{r})$. Next the Hamiltonian according to the initial electron density can be formulated. By using a basis set of wavefunctions, e.g. plane waves, and a few approximations, such as energy cut-offs, the Kohn-Sham equations can be solved. The solutions which are known as the Kohn-Sham orbitals $\phi_i(\mathbf{r})$ can be taken to compute the corresponding electron density. By mixing the new and the initial electron density one can further repeat this procedure. Usually the criteria of stopping this iterative algorithm is by looking on the convergence of the total energy of the system. If the total energy has not changed compared to previous loops of the algorithm, then the calculation can be stopped. The final charge density is then approximately the ground density of the system and the final total energy is the ground state energy.

4.3. Transport Theory

In classical electrodynamics electron transfer only takes place within conductors. As long as two conductors are not connected, there will be no electron moving from one conductor to the other one. Quantum mechanics predicts that there is a non-vanishing probability that an electron can tunnel through a potential well, e.g. a gap between two conductors. In order to obey physics in the well-proven classical regime it is necessary that such a probability will be negligible small for sufficiently large gaps. For comparable small gaps electron transport through the gap could become important. In this section we want to introduce a method based on a Green's function technique, which enables the calculation of such an electron transport probability through an arbitrary interface, e.g. a molecule. In this method the corresponding system is divided into three parts: two half-infinity leads
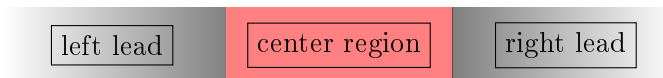
Figure 4.2.: Division of the system into three regions within the NEGF method.

which are connected via a center region (see Fig. 4.2). The center region represents the interface of which we want to know the electron transport probability.

The two leads need to behave like bulk material. In order to fulfill this constraint, the center region needs to contain additional material of the leads on both sides to screen the interface. The thickness of the additional material is determined by the screening length of the interface.

4.3.1. Landauer-Büttiker Formalism

The electronic transport through a specified region can be evaluated via the Landauer[6]-Büttiker[7] Formalism (for a detailed introduction see Appendix A.1)

> **Landauer-Büttiker Formalism**
>
> $$I(V) = \frac{2e}{h} \int T(E)\Big(f(E - \mu_L) - f(E - \mu_R)\Big)dE \qquad (4.20)$$

where $f(x) = \frac{1}{1+\exp\{\frac{x}{k_B T}\}}$ is the Fermi[8]-Dirac[9] distribution and $\mu_L = E_F + \frac{e}{2}V$ and $\mu_R = E_F - \frac{e}{2}V$ are the chemical potentials of the left and right electrode, respectively. The transmission function $T(E)$ describes the probability of transporting an electron with energy E from the left to the right electrode.

4.4. Electron Tunneling

In this section the process of electron tunneling due to electron transport through molecules will be discussed. The standard tunneling process is described by an exponential decrease of the probability of presence.

---

[6]Rolf William Landauer, German-American physicist, *1927, +1999.
[7]Markus Büttiker, Swiss physicist, *1950, +2013.
[8]Enrico Fermi, Italian physicist, *1901, +1954.
[9]Paul Adrien Maurice Dirac, English theoretical physicist, *1902, +1984.

4.4.1. Tunneling at Molecule Junctions

In order to understand at least parts of the (quantum) mechanism of tunneling through molecular junctions there is hardly a way around a concept using the highest occupied molecule orbital (HOMO) and the lowest unoccupied molecule orbital (LUMO). One can consider these energy levels as transfer channels, but they must have different transport mechanisms because the LUMO channel is unoccupied and the HOMO channel is occupied. In other words, when using the LUMO channel direct transport is possible, but for the HOMO channel only indirect transport is possible. Hence tunneling via the HOMO channel can be viewed as a hole tunneling in opposite direction. A schematic visualization of such transport processes is given in Fig. 4.3 and 4.4. Additional help to some insights into the

(a) Step 1: An electron at the left electrode is excited.

(b) Step 2: It partially occupies the LUMO.

(c) Step 3: It switches to the right electrode.
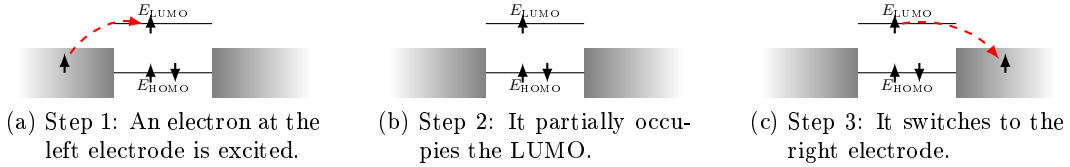
Figure 4.3.: Direct electron transport via the LUMO of the embedded molecule.

(a) Step 1: An electron at the HOMO is excited.

(b) Step 2: It switches to the right electrode.

(c) Step 3: An electron at the left electrode switches to the HOMO.
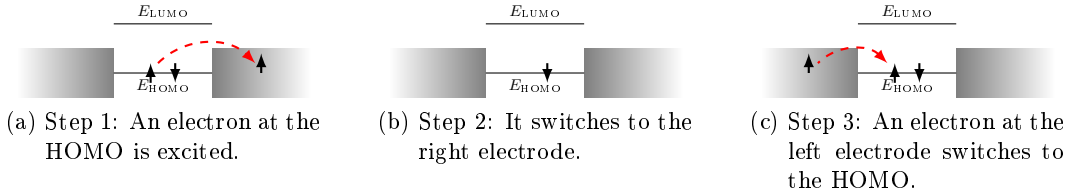
Figure 4.4.: Indirect electron transport via the HOMO of the embedded molecule.

mechanism is offered by the Landauer-Büttiker Formalism. Behold $h(E) \equiv f(E - \mu_L) - f(E - \mu_R)$ of Eqn. 4.20. Let the left and the right electrode consist of the same material. Then, for an arbitrary bias V, which is applied onto the system, the chemical potentials of the left and right lead are $\mu_L = E_F + \frac{e}{2}V$ and $\mu_R = E_F - \frac{e}{2}V$ respectively. The function h is centered symmetrically around the Fermi energy. This implies that in the Landauer-Büttiker formula the transmission function is integrated symmetrically around the Fermi level. That means further that a peak in the transmission function below the Fermi energy will give the same effect as the same peak above the Fermi energy as long as the energy distance of the peak to the Fermi level keeps the same. Hence there are contributions both from transport channels below and above the Fermi energy depending on the applied bias. This indicates that at least for systems where the HOMO of the isolated molecule keeps occupied and the LUMO of the isolated molecule keeps unoccupied when the molecule is adsorbed, both mechanisms, direct and indirect electron transport via molecule energy levels, are equally important.

5. DFT Simulations - Molecular Tunnel Junction - Results

> It is nice to know that the computer understands the problem. But I would like to understand it too.
>
> Eugene Wigner

5.1. Simulation Tools

5.1.1. VASP

The standard DFT calculations have been performed using the Vienna *Ab-Initio* Simulation Package (VASP) [74, 75] which is a Fortran 90 program for first-principle molecular dynamics simulations of molecules and solids. It is based on the Kohn-Sham algorithm, described in the subsection 4.2.4. In VASP the Kohn-Sham orbitals are represented by a plane wave basis set expansion. In order to minimize the taken number of plane waves the projector augmented wave method and ultra soft Vanderbilt pseudo-potentials are used. The most time consuming step is a matrix diagonalization, where different algorithms are available, e.g. a conjugate gradient scheme. For the mixing of the electron density a Pulay-Broyden mixing is implemented. Additionally, the Hellmann-Feynmann theorem is applied to enable the calculation of the forces on each atom core. Hence a relaxation concerning the position of the cores can be performed. The positions of the ions are set up in a so-called supercell with periodic boundary conditions.

5.1.2. TranSIESTA

In this thesis electron transport calculations have been performed using the computer program Transport Spanish Initiative for Electronic Simulations with Thousands of Atoms (TranSIESTA) [76, 77]. TranSIESTA is based on the program SIESTA (Spanish Initiative for Electronic Simulations with Thousands of Atoms). SIESTA is like VASP a computer program that performs first-principle calculations of molecules and solids. As VASP it uses pseudo-potentials for the electron-ion interaction. The most markable difference of VASP and SIESTA is the choice of the basis set. While VASP uses a plane wave basis set, SIESTA uses pseudo-atomic orbital basis sets. Atomic orbital basis states are localized basis sets. All basis sets that can be used within SIESTA need to be radial functions multiplied by spherical harmonics. The implemented basis sets in SIESTA are the single-ζ (SZ), the single-ζ polarized (SZP), the double-ζ (DZ), and the double-ζ polarized (DZP) basis sets. ζ is here a parameter for the radial function. A single-ζ basis set uses one parameter for the radial function per angular momentum. The SZP and DZP includes additional polarization orbitals, which are constructed from perturbation theory. While the SZ basis set is not very accurate and is usually used for obtaining qualitative results, the DZP gives (high) accurate results. More information about pseudo-atomic orbital basis sets is given in reference [78].

In order to calculate the electron transmission function through a certain region the Tran-SIESTA code can be used. TranSIESTA is an implementation of the Landauer-Büttiker

Formalism, introduced in chapter 4.3. The Landauer-Büttiker Formalism needs the input of the energy eigenvalues and wavefunctions of the system, which is provided by SIESTA.

5.2. Adsorption Position

We investigate silver, a metal given in the face-centered cubic (fcc) structure and consider a possible fcc(111) surface. Since we are interested in sub-nanometer gaps we distinctly discuss the term 'gap' within a quantum mechanic picture. We further concentrate on self assembled monolayer in such gaps. For the molecule adsorption positions on the silver (111) surface the fcc and hcp three-fold hollow sites are assumed [79]. In Fig. 5.1 four high symmetry points are shown, the top site (T), the bridge site (B), the fcc (F) and hcp (H) three-fold hollow site.
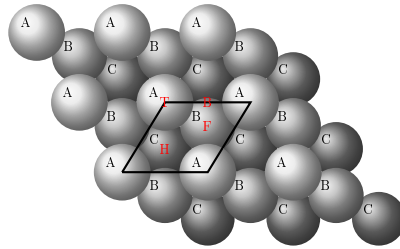
Figure 5.1.: Top view onto a fcc(111) surface. The black capitals A, B and C label the topmost, second and third layer of the surface. The red capitals label high symmetry adsorption positions: the top site (T), the bridge site (B), the fcc (F) and hcp (H) three-fold hollow site.

5.3. Vacuum Gap Between Two Silver Surfaces

By keeping the assumption that the facing area in the gap region of the silver cubes are build up of fcc(111) layers we sketch the vacuum gap between such two cubes. In Fig. 5.2 a bulk silver structure is given which is further extended by inserting a vacuum gap along a fcc(111) layer, sketched in Fig. 5.3.
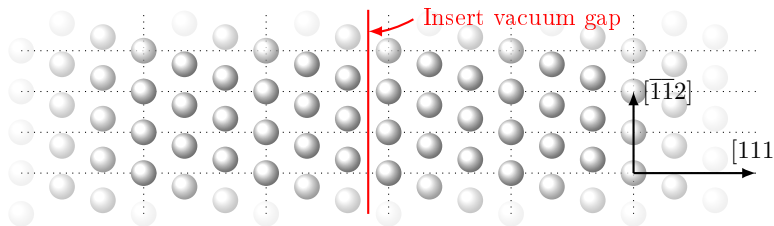
Figure 5.2.: Bulk Ag(111).
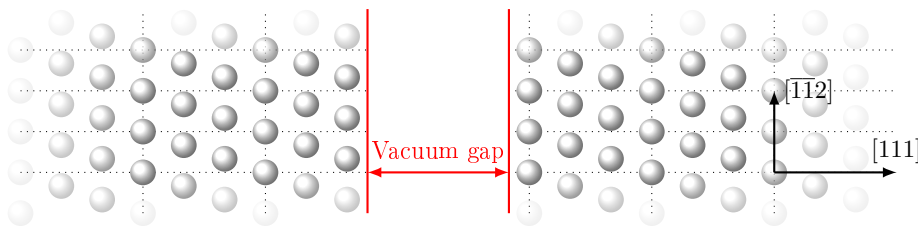
Figure 5.3.: Ag(111) with inserted vacuum.

5.4. Self Assembled Monolayer

By keeping the assumption that the facing area in the gap region of the silver cubes are build up of fcc(111) layers we sketch how a self assembled monolayer could be positioned within such two cubes instead of a vacuum. The investigated metal-molecule-metal interfaces are Ag(111)-BDT-Ag(111) and Ag(111)-EDT-Ag(111) where the self assembled monolayer (SAM) consists of aromatic 1,4-benzenedithiolates (BDT) and of saturated aliphatic 1,2-ethanedithiolates (EDT) molecules, respectively. For the structure of the molecules see Fig. 5.4. Both molecules are build up of carbon, hydrogen and sulfur atoms. In Fig. 5.4 hydrogen atoms are represented by small white spheres, carbon atoms are represented by brown spheres and sulfur atoms are represented by large yellow spheres. Notice, when the

(a) BDT   (b) EDT
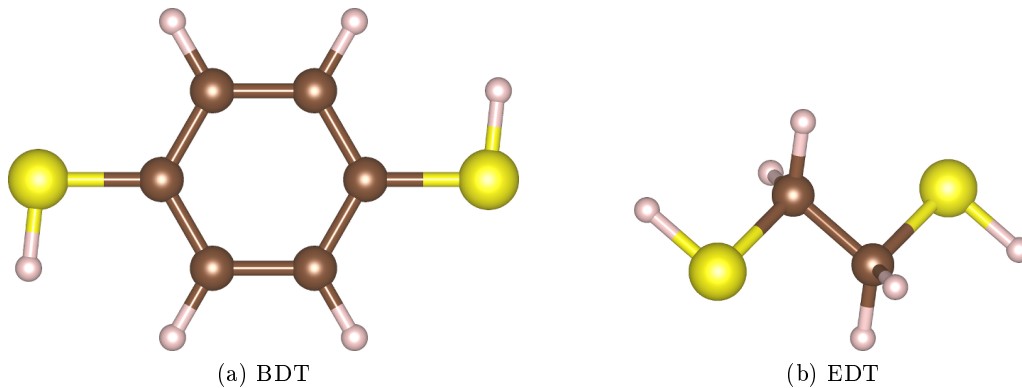
Figure 5.4.: **Left: B**enzene**dit**hiol (BDT). **Right: E**thane**dit**hiol (EDT).

BDT/EDT molecule is bonded to a structure the hydrogen atoms bonded to the sulfur atoms get apart in order to conserve charge neutrality. A side view of the atomistic structure of a BDT molecule placed between Ag(111) surfaces is sketched in Fig. 5.5. Analogously, a side view of the atomistic structure of a EDT molecule placed between Ag(111) surfaces is sketched in Fig. 5.6. Although experiments [9] have shown that the BDT/EDT molecules can appear both in tilted positions and in well aligned positions w.r.t. the silver cube facet, in this work well aligned molecules are assumed only. In reference [9]
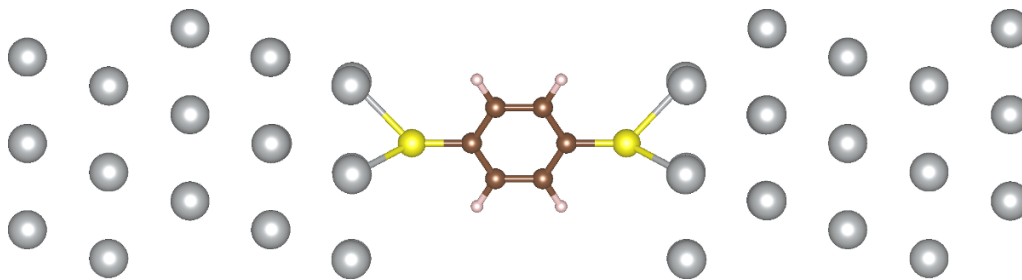
Figure 5.5.: Side view of the atomistic structure of Ag(111)-BDT-Ag(111).

one has shown that the probability for electron transmission through gap molecules does depend most on the length and type of the molecule, but not so much on its alignment to the metal surface, which could rectify our assumption on the alignment. Our main aspect of performing *ab-initio* calculations within the framework of this thesis, is to investigate electron transmission through a self assembled monolayer between two conductors.
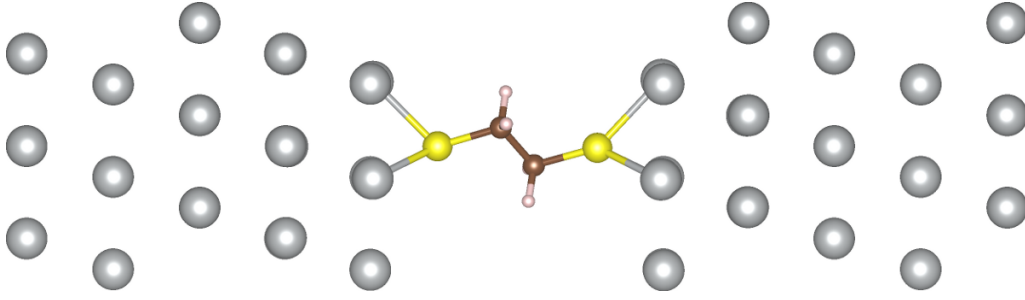
Figure 5.6.: Side view of the atomistic structure of Ag(111)-EDT-Ag(111).

5.5. DFT-Optimized Gap Width

First we start with isolated molecules, i.e. the molecule is placed into vacuum and a DFT calculation using VASP is applied. This allows to calculate the energy levels, especially the HOMO and LUMO level, the density of states and more. This has been performed on the molecules BDT and EDT. Their structures are sketched in Fig. 5.4. Then, an uncovered surface of Ag(111), Fig. 5.3, has been investigated with VASP. Afterwards, a covered silver surface has been simulated, where a hcp three-fold hollow site adsorption position has been assumed, see Fig. 5.1. Finally the molecules are placed between two silver surfaces, sketched in Fig. 5.5 and in Fig. 5.6. This calculation has been repeated several times with different molecule lengths. The optimization of the molecule lengths of BDT and EDT between two silver surfaces is plotted in Fig. 5.7. This has been realized using the Hellmann-Feynman-Theorem which offers a scheme to compute the forces on each ion in a solid system. By applying the theorem within VASP, the equilibrium positions of the ions of the molecules between the conductors have been determined iteratively. Additionally, the positions of the ions of the first two topmost layers of the conductors are optimized. The bulk positions of the other layers has been kept throughout the relaxation calculation. This procedure has been performed for several separation distances of the conductors. Fig. 5.7 shows two parabolic curves with minimums at approximately 7.4 Å for BDT and 5.6 Å for EDT. These separation distances, where the total energies of the supercells are minimized, are called DFT-optimized separation distances.
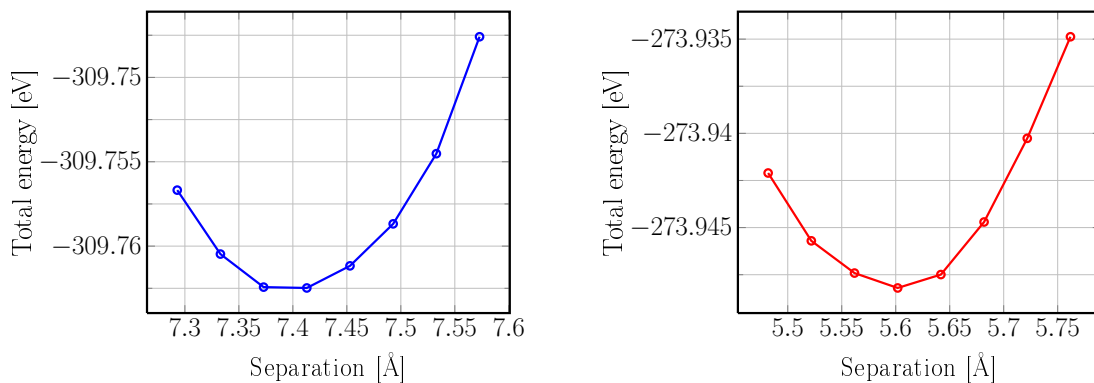
Figure 5.7.: Molecule filled gap width between the hypothetically unre-laxed topmost silver surface layer [111]-positions against the total energy of the supercell of Ag(111)-molecule-Ag(111). **Left:** BDT. **Right:** EDT.

5.6. Electron Charge Density

In Fig. 5.8 the plane averaged electron density along a cross section of the Ag(111) layers is plotted. The positive ionic background is approximated by a constant contribution, i.e. jellium model. Since the z-position of the unrelaxed surface layer is set to $z = 0$, the positive ionic jellium background reaches half a (111)-layer-interval into positive z-direction. The electron density has been computed in order to give an insight of its spill out. For the simulation the software package VASP has been used.

In fact, by inserting a vacuum gap between two silver (111)-layers, as pictured in Fig. 5.3, on each surface the electron density reaches into the vacuum. The overlap of both corresponding wavefunctions determines the electron transmission probability through the gap. Since the spill out decreases exponentially into the vacuum, the overlap decreases exponentially with an increasing vacuum gap. This results in an exponentially decreasing electron transmission through a vacuum gap between two conductors.
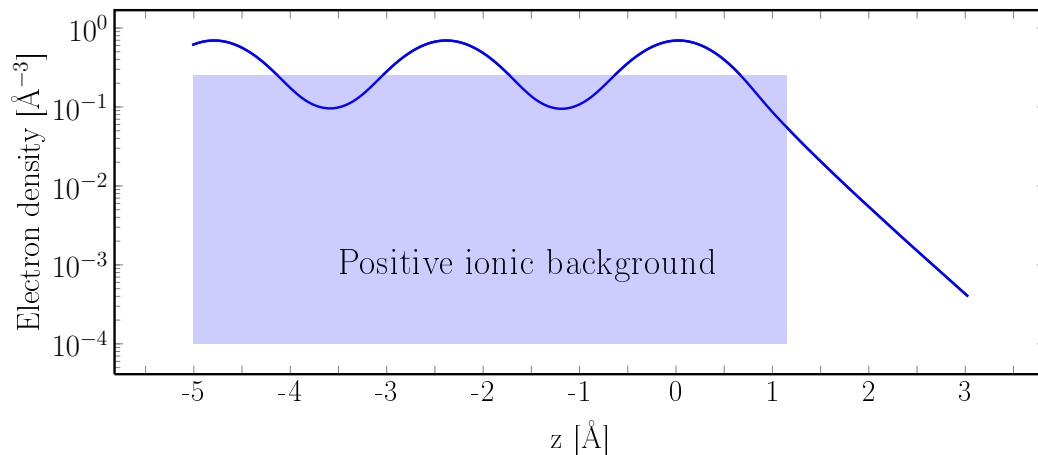
Figure 5.8.: Plane averaged electron charge density of a (111) silver slab, consisting of 10 layers, with jellium background.

5.7. Density of States

The energy positions of the HOMO and LUMO level of the SAM and their energy difference determines the behavior of electron transmission through SAM. They determine the probability that an electron with a certain energy transmits the center region. In Fig. 5.9
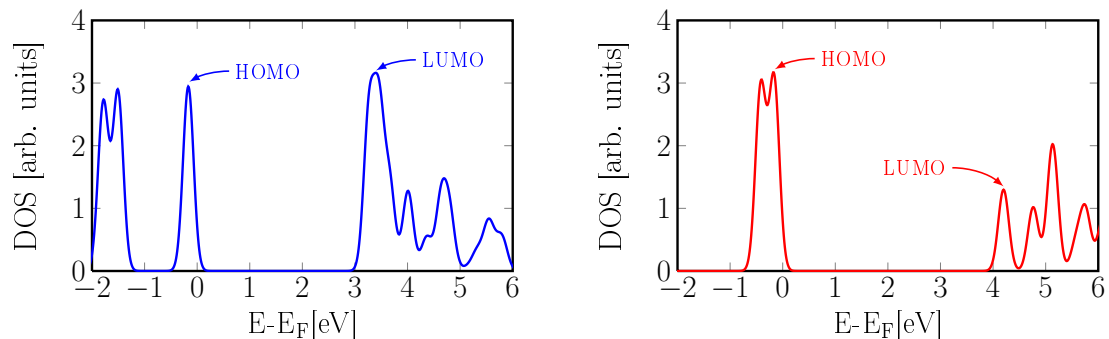
Figure 5.9.: Simulated density of states of isolated molecules.
Left: BDT. **Right:** EDT.

the simulated DOS of the isolated molecule is plotted. The HOMO and LUMO peaks

are highlighted in the figure. The simulations have been performed using VASP. A GGA exchange-correlation functional has been used. In Fig. 5.10 the simulated energy levels
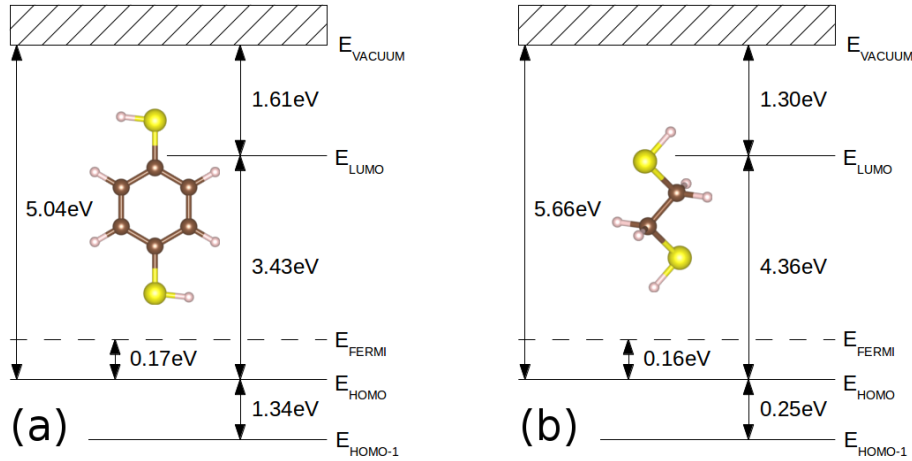
Figure 5.10.: Simulated energy levels of the isolated molecules (a) BDT and (b) EDT.

of the isolated molecules BDT and EDT are sketched. The energy levels and the Fermi level have been taken from the OUTCAR file of the corresponding VASP simulation. The vacuum level has been computed from the data of the LOCPOT file. A characteristic quantity is the HOMO-LUMO energy gap. For electron transport through the molecule the energy gap determines the potential barrier for an electron. The HOMO-LUMO gap of BDT is 3.43 eV, the HOMO-LUMO gap of EDT is 4.36 eV. In Fig. 5.11 the Molecule Orbital Projected Density of States (MOPDOS) of the Ag(111)-BDT interface and the MOPDOS of the Ag(111)-EDT interface have been plotted. The main concept of MOPDOS underlies the projection of the molecule orbital of the isolated molecule onto the full interface system. This can be achieved by selecting the corresponding Kohn-Sham orbitals in VASP and performing a projection onto all orbitals of the full interface system. Due to coupling of the silver layers with the molecule a hybridization of the orbital can occur. In both investigated systems the projection of the HOMO and LUMO of the isolated molecule are visualized by red and blue colors, respectively. In Fig. 5.12 the MOPDOS of the Ag(111)-BDT-Ag(111) interface and the MOPDOS of the Ag(111)-EDT-Ag(111) interface have been plotted.
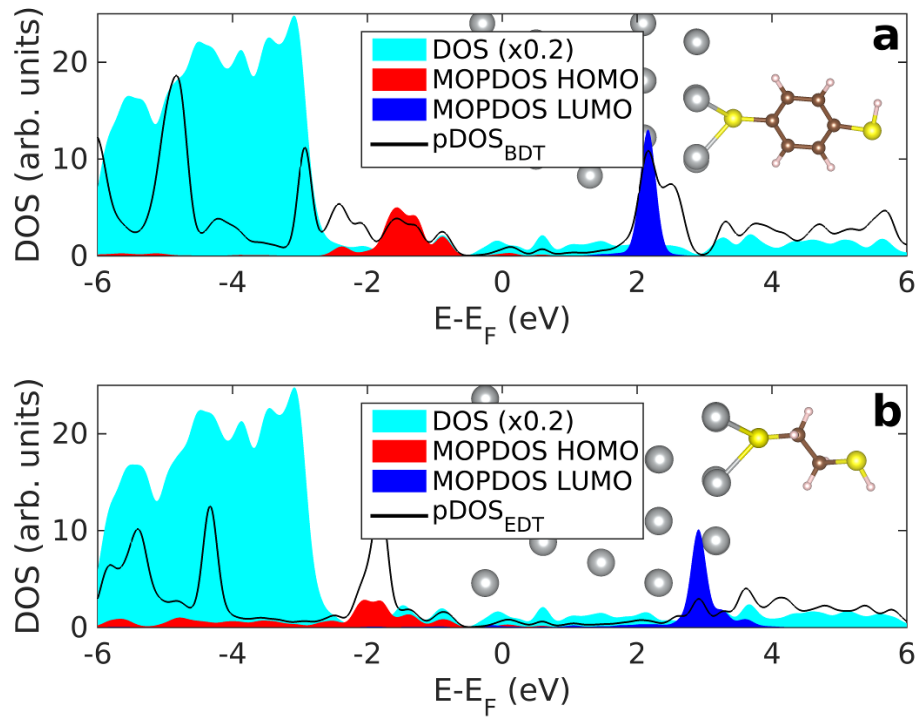
Figure 5.11.: Simulated Molecule Orbital Projected Density of States (MOPDOS) of the (a) Ag(111)-BDT interface and of the (b) Ag(111)-EDT interface.
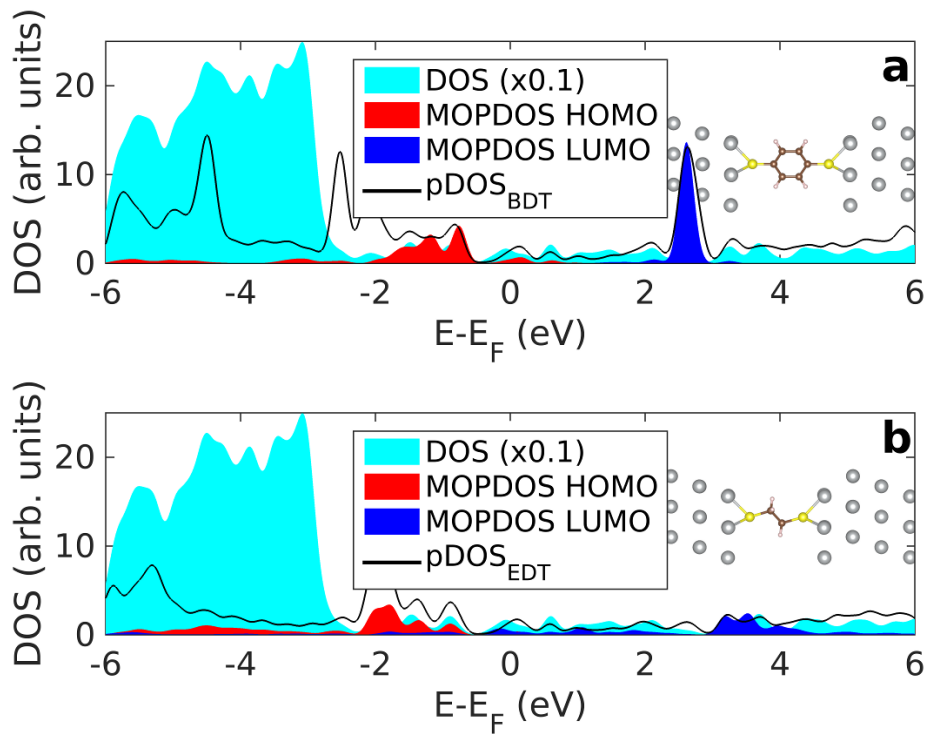
Figure 5.12.: Simulated Molecule Orbital Projected Density of States (MOPDOS) of the (a) Ag(111)-BDT-Ag(111) interface and of the (b) Ag(111)-EDT-Ag(111) interface. Data are partially taken from reference [54].

5.7.1. Discussion

For systems containing material gaps, the electron gap tunneling probability is (aside the nanoparticles geometrics and material parameters) not purely determined by the gap width. The phenomenological description of electron transport through a self assembled molecule layer, given in Subsection 4.4.1 where a direct and indirect transport has been discussed (see also Fig. 4.3 and Fig. 4.4), leads to the expectation that the HOMO and LUMO has a great impact on the electron tunneling probability.

In Fig. 5.9 the HOMO and LUMO energy positions of the isolated molecules BDT and EDT are plotted. It is clear that a smaller molecule length will result in a higher electron tunneling probability. Additionally, the description of the electron transport through a self assembled molecule layer states that a smaller LUMO-HOMO energy gap leads to a higher electron tunneling probability. The molecule length of BDT is larger than that of EDT. The LUMO-HOMO energy difference of BDT (3.43eV) is smaller than that of EDT (4.36eV).

One reason of performing pDOS and molecule orbital projected density of states (MOPDOS) calculations of the HOMO and LUMO of the molecules BDT and EDT is to uncover possible hybridization effects. In Fig. 5.11 the MOPDOS of the silver-molecule are plotted. Compared to Fig. 5.9 the most hybridization is given for the HOMO of the EDT molecule.

In Fig. 5.12 the MOPDOS of the silver-molecule-silver interfaces are plotted. One can recognize a hybridization of the LUMO of the EDT molecule, while the BDT molecule keeps almost unhybridized. By comparing the 'Ag-Mol'-system with the 'Ag-Mol-Ag'-system one can see that the projection of the LUMO keeps almost the same for the molecule BDT, but changes drastically for the molecule EDT. Explanations to these results can be given by the band decomposed electron charge densities.

5.8. Band Decomposed Electron Charge Density
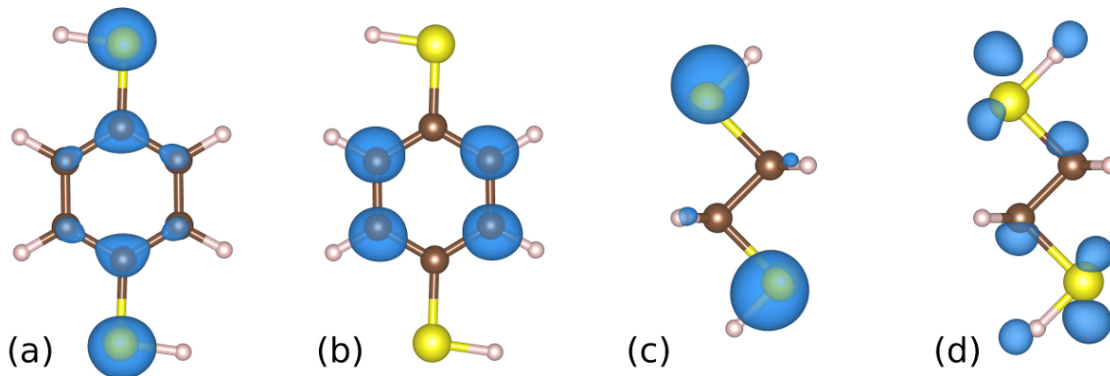
Figure 5.13.: Simulated band decomposed charge densities of the (a) HOMO and the (b) LUMO of the isolated molecule BDT and simulated band decomposed charge densities of the (c) HOMO and the (d) LUMO of the isolated molecule EDT. The electron charge density is highlighted by the blue color which shows the iso-surfaces of the electron charge density.

In Section 4.4 where electron tunneling through a metal-molecule-metal interface is discussed, the importance of the HOMO and LUMO transmission channel has been pointed out (see Fig. 4.3 and Fig. 4.4). Since the bonding of the molecule on the metal surfaces can lead to hybridization, we have performed a VASP calculation in order to visualize parts of the electron charge density, e.g. the electron charge density corresponding to the LUMO of the isolated molecule.
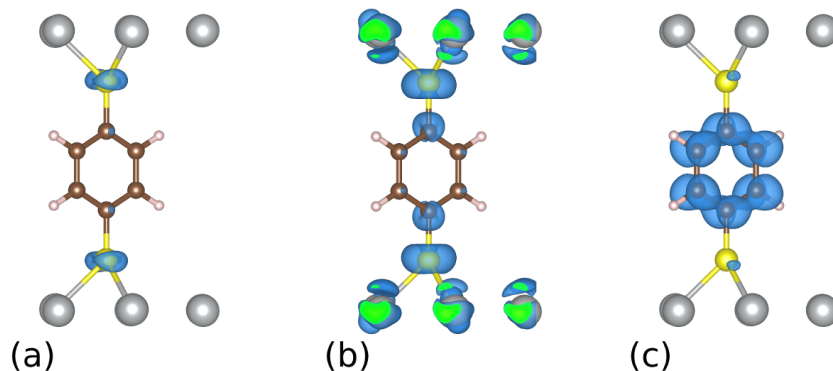
Figure 5.14.: Simulated band decomposed charge densities of the (a) former HOMO, the (b) intersection part and the (c) former LUMO of Ag(111)-BDT-Ag(111). The electron charge density is highlighted by the blue color which shows the iso-surfaces of the electron charge density.
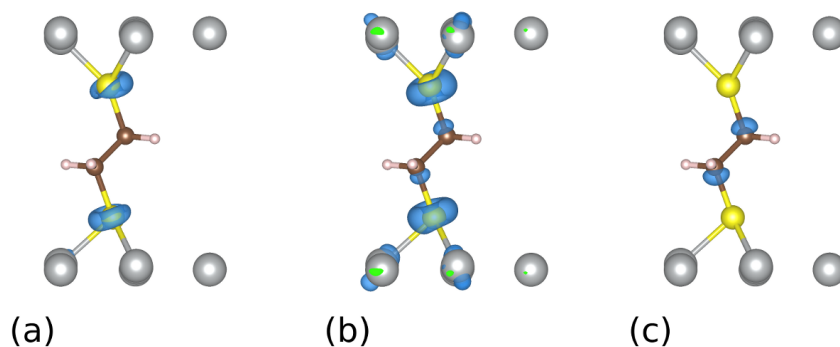
Figure 5.15.: Simulated band decomposed charge densities of the (a) former HOMO, the (b) intersection part and the (c) former LUMO of Ag(111)-EDT-Ag(111). The electron charge density is highlighted by the blue color which shows the iso-surfaces of the electron charge density.

In addition, for a comparison the electron charge density of the isolated molecule has been visualized. In Fig. 5.13 the DFT-simulated band decomposed charge densities of the HOMO and the LUMO of the isolated molecules BDT and EDT are plotted. The electron charge density is highlighted by the blue color which shows the iso-surfaces of the electron charge density. The threshold value of the iso-surfaces is set to 0.01. In Fig. 5.14 the DFT-simulated band decomposed charge density of the former HOMO and former LUMO of Ag(111)-BDT-Ag(111) is plotted. Additionally, a plot of the intersection part between the former HOMO and former LUMO is plotted. The former HOMO and former LUMO corresponds to the isolated molecule BDT.

In Fig. 5.15 the DFT-simulated band decomposed charge density of the former HOMO and former LUMO of Ag(111)-EDT-Ag(111) is plotted. As in the previous figure, the former HOMO and former LUMO corresponds to the isolated molecule EDT.

5.8.1. Discussion

While for the BDT molecule the electron charge density is most around the carbon atoms, for the EDT molecule the electron charge density is most at the sulfur atoms. Figs. 5.14 and 5.15 are plots of the simulated band decomposed charge densities of the HOMO/LUMO of the metal-molecule-metal interfaces. For BDT a small hybridization can be seen for the HOMO of the isolated molecule. The LUMO keeps widely unhybridized. For EDT it is hard to account the level of hybridization. One can state definitely that the band

decomposed charge densities of HOMO/LUMO look different for the isolated molecule compared to the interface system.

For BDT the properties of the benzene ring are expected to be reason of the lack of hybridization at the LUMO, which will lead to clearer results in further investigated physical quantities (such as the electron transmission through the molecule).

5.9. Transmission Function

The transmission function can play the connecting part between *ab-initio* quantum mechanical theories and semi-classical theories. In this part we calculate the transmission function of an electron transport through a metal-molecule-metal interface. With the Landauer-Büttiker formula, Eqn. 4.20, one can compute the electron current through the center region[1] for an applied bias. Here we calculated by using TranSIESTA the transmission function through BDT and through EDT, when each of these molecules is placed between two silver conductors.
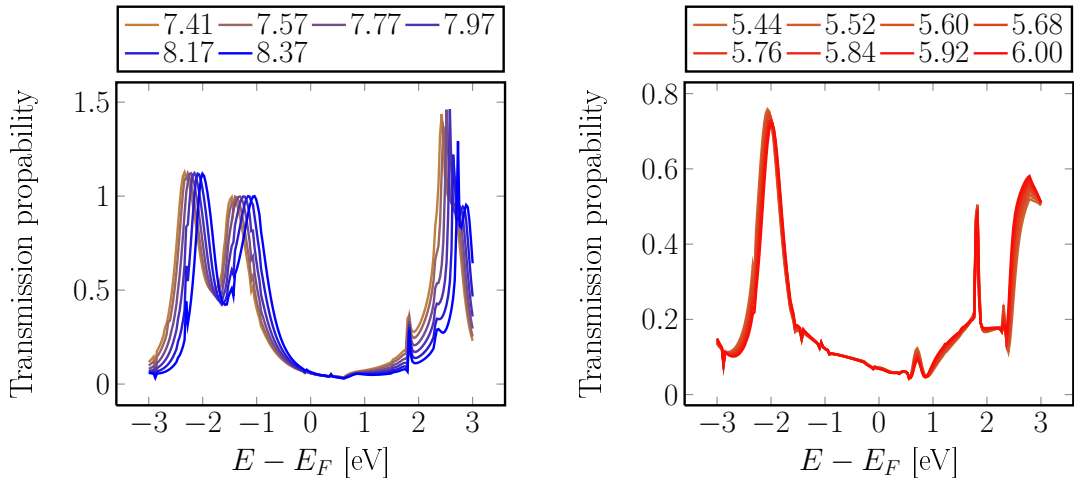
Figure 5.16.: Simulated transmission function of Ag(111)-SAM-Ag(111) for different gap widths (legends given in Å). The basis set is DZP. **Left:** BDT. **Right:** EDT.

In order to guarantee that the left and right conductors behave like bulk material, the center region does not consist of the molecule (BDT/EDT) only. Additional layers of the conductor are added into the center region to screen the molecule. Hence the number of such additional layers depends on the screening length of the molecule.

Transmission functions of Ag(111)-BDT-Ag(111) and Ag(111)-EDT-Ag(111) for different gap widths are plotted in Fig. 5.16. A GGA exchange-correlation functional and a DZP basis set has been taken. A Fermi-Dirac occupation function with an electronic temperature of 300 K has been used.

5.9.1. Discussion

According to the Landauer-Büttiker formula (Eqn. 4.20), an applied voltage is centered symmetrically around the Fermi level E_F for identical left and right electrodes. In detail, the symmetry is given by the term $f(E - \mu_L) - f(E - \mu_R)$, where f is the Fermi-Dirac distribution function, and $\mu_L = E_F + \frac{e}{2}V$ and $\mu_R = E_F - \frac{e}{2}V$ are the chemical potentials of the left and right electrode. The symmetric centering is caused by the $\pm \frac{e}{2}V$ contributions of the identical left electrodes.

---

[1] The concept of the center region has been introduced in Section 4.3.

In Fig. 5.16 transmission functions of Ag(111)-BDT-Ag(111) and Ag(111)-EDT-Ag(111) are plotted for different gap widths or molecule lengths respectively. When increasing the gap width of Ag(111)-BDT-Ag(111) the whole transmission function shifts to higher energies in the investigated gap width range. Such a trend is not visible for Ag(111)-EDT-Ag(111). The former HOMO and LUMO peaks are still present in the DOS. In contrast, the former HOMO and LUMO of Ag(111)-EDT-Ag(111) are hybridized and not clearly localized. In Fig. 5.16 the left plot shows artificial transmission probabilities above 1.

5.10. Electron Current

In Fig. 5.17 the simulated current through the center region is plotted. The currents are computed by applying the Landauer-Büttiker formula.
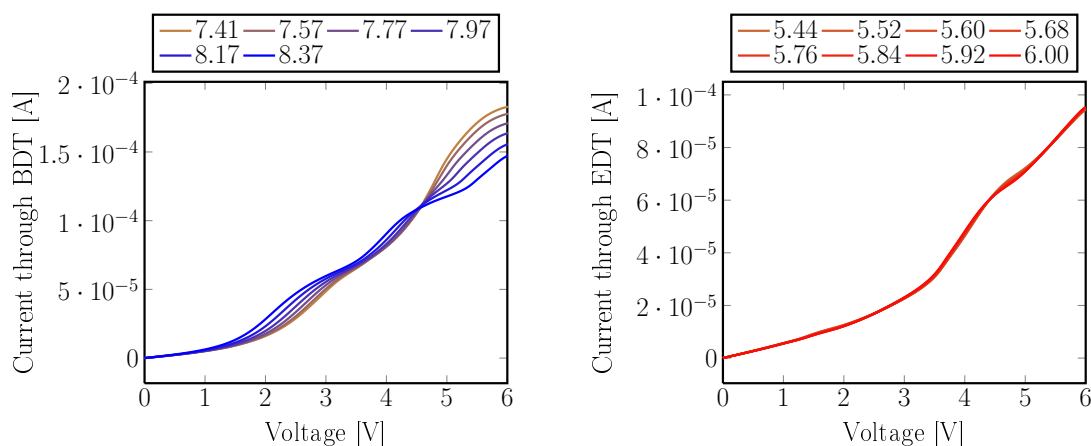
Figure 5.17.: Simulated current through BDT/EDT molecule of Ag(111)-SAM-Ag(111) interface for different gap widths (legends given in Å). The basis set is DZP. **Left:** BDT. **Right:** EDT.

5.10.1. Discussion

The simulated electron currents through the molecules of the systems Ag(111)-molecule-Ag(111), where BDT and EDT has been used for the molecule, are plotted in Fig. 5.17. However, classically one would expect an increasing electron current through the molecule for an increasing applied voltage on both ends of the molecule. Further, one would expect a decreasing electron current for increasing molecule lengths (separation distances), but there occurs a counter-intuitive result of the system Ag(111)-BDT-Ag(111). In the bias range from 0 to 4.5 Volts the electron current increases for increasing separation distances. This effect can be explained with the transmission function, plotted in Fig. 5.16. For increasing separation distances the HOMO and LUMO peaks of the transmission function shifts from left to right. This feature emerges from a shift of the HOMO energy level of the molecule towards the Fermi level for increasing separation distances. In the Landauer-Büttiker formula such a shift corresponds to an increasing current. However, there does not occur such a feature for the other system Ag(111)-EDT-Ag(111).

5.11. Electric Conductance

In Fig. 5.18 the simulated differential conductance for the center region is plotted.
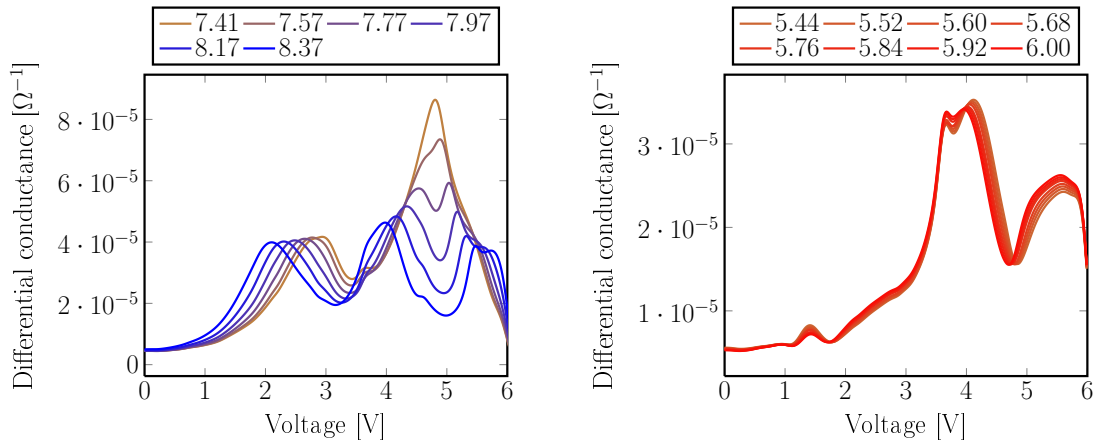
Figure 5.18.: Simulated differential conductance through BDT/EDT molecule of Ag(111)-SAM-Ag(111) interface for different gap widths (legends given in Å). The basis set is DZP. **Left:** BDT. **Right:** EDT.

5.11.1. Discussion

Clearly, as in Fig. 5.17, a counter-intuitive result for the system Ag(111)-BDT-Ag(111) is present. In the bias range from 0 to 4.5 Volts the differential conductance increases for increasing separation distances. For the differential conductance this counter-intuitive result is stronger than for the electron current. This feature does not occur for the other system, Ag(111)-EDT-Ag(111).

6. Quantum Tunneling - Theory

> Your theory is crazy, but it's not crazy enough to be true.

<div align="right">Niels Bohr</div>

In this chapter an *ab-initio* model for simulating slab geometries is described. The application of this model is motivated by finding plasmonic resonances at the surface of slab geometries by using quantum physics only. The focus is set on slab geometries, since we are interested in flat gaps between two nano-particles in a simple one-dimensional model.

First, we briefly give an overview of time-dependent current-density functional theory (TDCDFT). Next, linear response (LR) theory is introduced. Consequently, the combination of LR and TDCDFT, the so-called LR-TDCDFT, is shown. In order to keep the theory as simple as possible, we consider one-dimensional systems in a three-dimensional frame-set.

6.1. Time-Dependent Current Density Functional Theory

On the basis of Time-Dependent Current Density Functional Theory (TDCDFT) stands the invertibility[1] of mapping the scalar and vector potentials to the density and the current density, which has been shown by Ghosh and Dhara [80]. The corresponding time-dependent Schrödinger equation represented in atomic units reads [81,82]

$$i\partial_t\psi_i(\mathbf{r},t) = \left\{\frac{1}{2}\left(-i\nabla + \frac{1}{c}\mathbf{A}_s(\mathbf{r},t)\right)^2 + V_s(\mathbf{r},t)\right\}\psi_i(\mathbf{r},t) \tag{6.1}$$

where $\left(-i\nabla + \frac{1}{c}\mathbf{A}_s(\mathbf{r},t)\right)$ is the kinetic momentum operator (and $-i\nabla$ is the canonical momentum operator). The (screened) effective scalar potential is given by

$$V_s(\mathbf{r},t) = V_{ext}(\mathbf{r},t) + V_H(\mathbf{r},t) + V_{xc}(\mathbf{r},t) \tag{6.2}$$

where $V_{ext}(\mathbf{r},t)$ is the external part, $V_H(\mathbf{r},t) = \int \frac{\rho(\mathbf{r}',t)}{|\mathbf{r}-\mathbf{r}'|}d^3r'$ is the Hartree potential and $V_{xc}(\mathbf{r},t)$ is the exchange-correlation part. The effective vector potential can be written as

$$\mathbf{A}_s(\mathbf{r},t) = \mathbf{A}_{ext}(\mathbf{r},t) + \frac{1}{c}\int \frac{\mathbf{J}_T(\mathbf{r}',t_r)}{|\mathbf{r}-\mathbf{r}'|}d^3r' + \mathbf{A}_{xc}(\mathbf{r},t) \tag{6.3}$$

with $t_r = t - \frac{1}{c}|\mathbf{r}-\mathbf{r}'|$, where $\mathbf{A}_{ext}(\mathbf{r},t)$ is the external part, the second term describing the classical part using the transversal current $\mathbf{J}_T$ and $\mathbf{A}_{xc}(\mathbf{r},t)$ is the exchange-correlation part. The charge density is given by

$$\rho(\mathbf{r},t) = \sum_{i=1}^{N}|\psi_i(\mathbf{r},t)|^2 \tag{6.4}$$

---

[1]Unique up to gauge transformations.

and the current density is given by

$$\mathbf{J}(\mathbf{r},t) = -\frac{i}{2}\sum_{i=1}^{N}\left\{\psi_i^*(\mathbf{r},t)\nabla\psi_i(\mathbf{r},t) - \left(\nabla\psi_i^*(\mathbf{r},t)\right)\psi_i(\mathbf{r},t)\right\} + \frac{1}{c}\rho(\mathbf{r},t)\mathbf{A}_s(\mathbf{r},t) \qquad (6.5)$$

By choosing Coulomb gauge, $\nabla\cdot\mathbf{A}=0$, the transversal current reads (see A.2)

$$\mathbf{J}_T(\mathbf{r},t) = \frac{1}{4\pi}\nabla\times\left(\nabla\times\int\frac{\mathbf{J}(\mathbf{r}',t)}{|\mathbf{r}-\mathbf{r}'|}d^3r'\right) \qquad (6.6)$$

Further it can also be expressed by

$$\mathbf{J}_T(\mathbf{r},t) = \mathbf{J}(\mathbf{r},t) - \mathbf{J}_L(\mathbf{r},t) = \mathbf{J}(\mathbf{r},t) + \frac{i\omega}{4\pi}\nabla V_H(\mathbf{r},t) \qquad (6.7)$$

6.2. Linear Response Theory

Let us consider a perturbed system described by the Hamiltonian

$$H = H_0 + H' = H_0 - AK(t) \qquad (6.8)$$

where H_0 is the Hamiltonian of the stationary unperturbed system, K is an applied force corresponding to the perturbation and A is a quantity associated to the applied force [83].

Let $B(t)$ be a physical quantity of the considered system. The expectation value $\langle B(t)\rangle$ of the perturbed system can be expressed by using the correlation function [84]

Correlation Function

$$\chi_{AB}(t,t') \equiv i\theta(t-t')\mathrm{tr}\Big\{\rho_0[A_I(t),B_I(t')]\Big\}. \qquad (6.9)$$

The linear response of the quantity B is given by

$$\delta\langle B(t)\rangle = \langle B(t)\rangle - \langle B(t)\rangle_0 = \int_{t_0}^{t}\chi_{BA}(t-t')K(t')dt'. \qquad (6.10)$$

The Fourier-transform of the correlation function reads

Fourier-transform of the Correlation Function

$$\chi_{AB}(\omega) = \lim_{\eta\to 0^+}\sum_{m,n}\frac{f_m - f_n}{\omega + E_m - E_n + i\eta}\langle m|A|n\rangle\langle n|B|m\rangle. \qquad (6.11)$$

An orthonormal eigenstate basis set $\big\{|n\rangle\big|n\in\mathbb{N}_0\big\}$ is used. f_n is the occupation number given by the (Fermi-Dirac) distribution function. Adiabatic turn-on is considered by inserting an infinitesimal $\eta\to 0^+$. For more details see Appendix A.3.

6.3. Linear Response - Time-Dependent Current Density Functional Theory

For small external perturbations it is possible to solve the TDCDFT by applying Linear Response Theory [82]. In this application only terms which are linear in the perturbation are taken into account while terms of higher orders are neglected. Consequently the physical quantities are determined by a set of linear equations being the idea of combining LR and TDCDFT.

From Eqn. 6.2 one obtains an expression for the variation of the scalar potential

$$\delta V_s(\mathbf{r}, t) = \delta V_{ext}(\mathbf{r}, t) + \int \frac{\delta\rho(\mathbf{r}', t)}{|\mathbf{r} - \mathbf{r}'|} d^3 r' + \delta V_{xc}(\mathbf{r}, t) \tag{6.12}$$

and from Eqn. 6.3 one obtains an expression for the variation of the vector potential

$$\delta\mathbf{A}_s(\mathbf{r}, t) = \delta\mathbf{A}_{ext}(\mathbf{r}, t) + \frac{1}{c} \int \frac{\delta\mathbf{J}_T(\mathbf{r}', t_r)}{|\mathbf{r} - \mathbf{r}'|} d^3 r' + \delta\mathbf{A}_{xc}(\mathbf{r}, t). \tag{6.13}$$

In detail the exchange correlation parts read

$$\delta V_{xc}(\mathbf{r}, t) = \int_{t_0}^{t} dt' \int d^3 r' f_{xc}(\mathbf{r}, \mathbf{r}', t - t') \delta\rho(\mathbf{r}', t') \tag{6.14}$$

and

$$\delta\mathbf{A}_{xc}(\mathbf{r}, t) = \int_{t_0}^{t} dt' \int d^3 r' \overleftrightarrow{\mathbf{f}}_{xc}(\mathbf{r}, \mathbf{r}', t - t') \delta\mathbf{J}(\mathbf{r}', t'). \tag{6.15}$$

The linear response of the density reads

$$\delta\rho(\mathbf{r}, \omega) = \int \left\{ \chi_{\rho\rho}(\mathbf{r}, \mathbf{r}', \omega) \delta V_s(\mathbf{r}', \omega) + \frac{1}{c} \chi_{\rho\mathbf{J}}(\mathbf{r}, \mathbf{r}', \omega) \delta\mathbf{A}_s(\mathbf{r}', \omega) \right\} d^3 r' \tag{6.16}$$

and of the current density it reads

$$\delta\mathbf{J}(\mathbf{r}, \omega) = \int \left\{ \chi_{\mathbf{J}\rho}(\mathbf{r}, \mathbf{r}', \omega) \delta V_s(\mathbf{r}', \omega) + \right.$$
$$\left. + \frac{1}{c} \left[\chi_{\mathbf{J}\mathbf{J}}(\mathbf{r}, \mathbf{r}', \omega) + \rho_0 \delta(\mathbf{r} - \mathbf{r}') \right] \delta\mathbf{A}_s(\mathbf{r}', \omega) \right\} d^3 r'. \tag{6.17}$$

where $\frac{1}{c}\chi_{\mathbf{J}\mathbf{J}}(\mathbf{r}, \mathbf{r}', \omega)\delta\mathbf{A}_s(\mathbf{r}', \omega)$ is the paramagnetic and $\frac{1}{c}\rho_0\delta(\mathbf{r} - \mathbf{r}')\delta\mathbf{A}_s(\mathbf{r}', \omega)$ is the diamagnetic [2] current density contribution.

6.3.1. Linear Response and TDCDFT - Matrix Equation

In this subsection we express the variation of the scalar potential and the variation of the vector potential using a matrix equation.

Using LR one can write the change of the density and of the current density as

$$\delta\rho = \chi_{\rho\rho}\delta V_s + \frac{1}{c}\chi_{\rho\mathbf{J}} \cdot \delta\mathbf{A}_s \tag{6.18}$$

$$\delta\mathbf{J} = \chi_{\mathbf{J}\rho}\delta V_s + \frac{1}{c}(\chi_{\mathbf{J}\mathbf{J}} + \rho_0)\delta\mathbf{A}_s. \tag{6.19}$$

---

[2] The current density can be written as $\mathbf{j}(\mathbf{r}) = -\frac{e}{2m}\psi^+(\mathbf{r})(\mathbf{p}+e\mathbf{A})\psi(\mathbf{r})+h.c. = \frac{ie\hbar}{2m}\left(\psi^+(\nabla\psi) - (\nabla\psi^+)\psi\right) - \frac{e^2}{m}\psi^+\psi\mathbf{A} = \mathbf{j}_p(\mathbf{r}) + \mathbf{j}_d(\mathbf{r})$ where $\mathbf{j}_p$ is the paramagnetic part and $\mathbf{j}_d$ is the diamagnetic part [85].

Using TDCDFT one can write the variation of the scalar potential and the variation of the vector potential as

$$\delta V_s = \delta V_{ext} + G_H \delta\rho + f_{xc}\delta\rho \tag{6.20}$$

$$\delta\mathbf{A}_s = \delta\mathbf{A}_{ext} + \frac{1}{c}G_H\delta\mathbf{J}_T + \overset{\leftrightarrow}{\mathbf{f}}_{xc} \cdot \delta\mathbf{J} \tag{6.21}$$

where G_H is the Green function of the Hartree potential. The variation of the transversal current reads

$$\delta\mathbf{J}_T = \delta\mathbf{J} + \frac{i\omega}{4\pi}(\nabla G_H)\delta\rho. \tag{6.22}$$

Inserting Eqs. 6.18 and 6.19 into Eqs. 6.20 and 6.21 gives

$$\delta V_s = \delta V_{ext} + (G_H + f_{xc})\left(\chi_{\rho\rho}\delta V_s + \frac{1}{c}\chi_{\rho\mathbf{J}}\cdot\delta\mathbf{A}_s\right) \tag{6.23}$$

$$\delta\mathbf{A}_s = \delta\mathbf{A}_{ext} + \left(\frac{1}{c}G_H + \overset{\leftrightarrow}{\mathbf{f}}_{xc}\right) \cdot \left(\chi_{\mathbf{J}\rho}\delta V_s + \frac{1}{c}(\chi_{\mathbf{J}\mathbf{J}} + \rho_0)\delta\mathbf{A}_s\right) +$$

$$+ \frac{i\omega}{4\pi c}G_H(\nabla G_H)\left(\chi_{\rho\rho}\delta V_s + \frac{1}{c}\chi_{\rho\mathbf{J}}\cdot\delta\mathbf{A}_s\right). \tag{6.24}$$

In order to summarize the LR-TDCDFT the four quantities $\delta\rho$, $\delta\mathbf{J}$, δV_s and $\delta\mathbf{A}_s$ describe the full system.

Linear Response - TDCDFT

$$\delta\rho = \chi_{\rho\rho}\delta V_s + \frac{1}{c}\chi_{\rho\mathbf{J}}\cdot\delta\mathbf{A}_s \tag{6.25}$$

$$\delta\mathbf{J} = \chi_{\mathbf{J}\rho}\delta V_s + \frac{1}{c}(\chi_{\mathbf{J}\mathbf{J}} + \rho_0)\delta\mathbf{A}_s \tag{6.26}$$

$$\delta V_s = \delta V_{ext} + (G_H + f_{xc})\left(\chi_{\rho\rho}\delta V_s + \frac{1}{c}\chi_{\rho\mathbf{J}}\cdot\delta\mathbf{A}_s\right) \tag{6.27}$$

$$\delta\mathbf{A}_s = \delta\mathbf{A}_{ext} + \left(\frac{1}{c}G_H + \overset{\leftrightarrow}{\mathbf{f}}_{xc}\right) \cdot \left(\chi_{\mathbf{J}\rho}\delta V_s + \frac{1}{c}(\chi_{\mathbf{J}\mathbf{J}} + \rho_0)\delta\mathbf{A}_s\right) +$$

$$+ \frac{i\omega}{4\pi c}G_H(\nabla G_H)\left(\chi_{\rho\rho}\delta V_s + \frac{1}{c}\chi_{\rho\mathbf{J}}\cdot\delta\mathbf{A}_s\right) \tag{6.28}$$

Rewriting the last two equations into a matrix equation can be helpful.

$$\begin{pmatrix} m_{11} & m_{12} & m_{13} & m_{14} \\ m_{21} & m_{22} & m_{23} & m_{24} \\ m_{31} & m_{32} & m_{33} & m_{34} \\ m_{41} & m_{42} & m_{43} & m_{44} \end{pmatrix} \cdot \begin{pmatrix} \delta V_s \\ \delta A_{s,x} \\ \delta A_{s,y} \\ \delta A_{s,z} \end{pmatrix} = \begin{pmatrix} \delta V_{ext} \\ \delta A_{ext,x} \\ \delta A_{ext,y} \\ \delta A_{ext,z} \end{pmatrix} \tag{6.29}$$

The matrix elements are

$$m_{11} = 1 - (G_H + f_{xc})\chi_{\rho\rho} \tag{6.30}$$

$$m_{12} = -(G_H + f_{xc})\frac{1}{c}\chi_{\rho j_x} \tag{6.31}$$

$$m_{13} = -(G_H + f_{xc})\frac{1}{c}\chi_{\rho j_y} \tag{6.32}$$

$$m_{14} = -(G_H + f_{xc})\frac{1}{c}\chi_{\rho j_z} \tag{6.33}$$

$$m_{21} = -\left(\frac{1}{c}G_H + \overleftrightarrow{f}_{xc}\right)\chi_{j_x\rho} - \frac{i\omega}{4\pi c}G_H(\partial_x G_H)\chi_{\rho\rho} \tag{6.34}$$

$$m_{22} = 1 - \left(\frac{1}{c}G_H + \overleftrightarrow{f}_{xc}\right)\frac{1}{c}(\chi_{j_xj_x} + \rho_0) - \frac{i\omega}{4\pi c}G_H(\partial_x G_H)\chi_{\rho j_x} \tag{6.35}$$

$$m_{23} = -\left(\frac{1}{c}G_H + \overleftrightarrow{f}_{xc}\right)\frac{1}{c}\chi_{j_xj_y} - \frac{i\omega}{4\pi c}G_H(\partial_x G_H)\chi_{\rho j_y} \tag{6.36}$$

$$m_{24} = -\left(\frac{1}{c}G_H + \overleftrightarrow{f}_{xc}\right)\frac{1}{c}\chi_{j_xj_z} - \frac{i\omega}{4\pi c}G_H(\partial_x G_H)\chi_{\rho j_z} \tag{6.37}$$

$$m_{31} = -\left(\frac{1}{c}G_H + \overleftrightarrow{f}_{xc}\right)\chi_{j_y\rho} - \frac{i\omega}{4\pi c}G_H(\partial_y G_H)\chi_{\rho\rho} \tag{6.38}$$

$$m_{32} = -\left(\frac{1}{c}G_H + \overleftrightarrow{f}_{xc}\right)\frac{1}{c}\chi_{j_yj_x} - \frac{i\omega}{4\pi c}G_H(\partial_y G_H)\chi_{\rho j_x} \tag{6.39}$$

$$m_{33} = 1 - \left(\frac{1}{c}G_H + \overleftrightarrow{f}_{xc}\right)\frac{1}{c}(\chi_{j_yj_y} + \rho_0) - \frac{i\omega}{4\pi c}G_H(\partial_y G_H)\chi_{\rho j_y} \tag{6.40}$$

$$m_{34} = -\left(\frac{1}{c}G_H + \overleftrightarrow{f}_{xc}\right)\frac{1}{c}\chi_{j_yj_z} - \frac{i\omega}{4\pi c}G_H(\partial_y G_H)\chi_{\rho j_z} \tag{6.41}$$

$$m_{41} = -\left(\frac{1}{c}G_H + \overleftrightarrow{f}_{xc}\right)\chi_{j_z\rho} - \frac{i\omega}{4\pi c}G_H(\partial_z G_H)\chi_{\rho\rho} \tag{6.42}$$

$$m_{42} = -\left(\frac{1}{c}G_H + \overleftrightarrow{f}_{xc}\right)\frac{1}{c}\chi_{j_zj_x} - \frac{i\omega}{4\pi c}G_H(\partial_z G_H)\chi_{\rho j_x} \tag{6.43}$$

$$m_{43} = -\left(\frac{1}{c}G_H + \overleftrightarrow{f}_{xc}\right)\frac{1}{c}\chi_{j_zj_y} - \frac{i\omega}{4\pi c}G_H(\partial_z G_H)\chi_{\rho j_y} \tag{6.44}$$

$$m_{44} = 1 - \left(\frac{1}{c}G_H + \overleftrightarrow{f}_{xc}\right)\frac{1}{c}(\chi_{j_zj_z} + \rho_0) - \frac{i\omega}{4\pi c}G_H(\partial_z G_H)\chi_{\rho j_z} \tag{6.45}$$

6.4. 1D-systems in a 3D frame-set

6.4.1. Electron Density

In this section we consider systems with one-dimensional external potentials $V_{ext}(x)$. The Kohn-Sham equations for the groundstate of such a system read

$$\left(-\frac{1}{2}\nabla^2 + V_{ext}(x) + V_H(x) + V_{xc}(x)\right)\phi_j(\mathbf{r}) = \epsilon_j\phi_j(\mathbf{r}) \tag{6.46}$$

where ϵ_j are the Kohn-Sham energies. Since the potentials depend only on x the Kohn-Sham orbitals ϕ_j can be factorized.

$$\phi_j(\mathbf{r}) = e^{ik_y y + ik_z z}\phi_j^\perp(x) = e^{i\mathbf{k}_\parallel\cdot\mathbf{r}}\phi_j^\perp(x) \tag{6.47}$$

Notice that for the parallel components the wavefunctions consist of plane waves. Hence in principle it is a 3D-system. The ground state density reads

$$n(x) = 2\sum_{\mathbf{k}_\parallel, j}|\phi_j^\perp(x)|^2\Theta(E_F - \epsilon_{k_\parallel} - \epsilon_j^\perp) \tag{6.48}$$

$$= \frac{2}{(2\pi)^2}\iint dk_y dk_z \sum_j |\phi_j^\perp(x)|^2\Theta(E_F - \frac{1}{2}k_\parallel^2 - \epsilon_j^\perp) \tag{6.49}$$

where $\epsilon_j = \epsilon_{k_\parallel} + \epsilon_j^\perp$ and $\epsilon_{k_\parallel} = \frac{1}{2}k_\parallel^2 = \frac{1}{2}\left(k_y^2 + k_z^2\right)$. Next we choose polar coordinates $dk_y dk_z = 2\pi k_\parallel dk_\parallel$ and substitute $\epsilon = \frac{1}{2}k_\parallel^2$. Then we have $dk_\parallel = \frac{1}{k_\parallel}d\epsilon$.

$$n(x) = \frac{2}{(2\pi)^2}2\pi \int d\epsilon \sum_j |\phi_j^\perp(x)|^2 \Theta(E_F - \epsilon - \epsilon_j^\perp) \tag{6.50}$$

The electron density of a basically 1D system in 3D reads

> **Density of a 1D system in 3D**
>
> $$n(x) = \frac{1}{\pi}\sum_j |\phi_j^\perp(x)|^2 \Theta(E_F - \epsilon_j^\perp). \tag{6.51}$$

6.4.2. Green's functions

For a 1D-system embedded in a 3D frame-set and depending on x the electron charge density can be written

$$n(x, y, z, t) = n(x)e^{i\mathbf{k}_\parallel \cdot \mathbf{r}} \tag{6.52}$$

where $\mathbf{k}_\parallel \perp \mathbf{e}_x$. When the parallel component of the wavefunction points into the y-direction the electron charge density can be written

$$n(x, y, z, t) = n(x)e^{ik_\parallel y}. \tag{6.53}$$

Then the Hartree potential $V_H(\mathbf{r})$ reads

$$V_H(x, y, z) = \int \frac{n(x')e^{ik_\parallel y'}}{|\mathbf{r} - \mathbf{r}'|}dr'^3 \tag{6.54}$$

$$= e^{ik_\parallel y} \iiint \frac{n(x')e^{ik_\parallel(y'-y)}}{|(x-x')^2 + (y-y')^2 + (z-z')^2|}dx'dy'dz'. \tag{6.55}$$

The application of a cylindrical coordinate substitution $y' - y = \rho\cos(\phi)$ and $z' - z = \rho\sin(\phi)$ results in

$$V_H(x, y) = e^{ik_\parallel y} \iint_{\rho=0}^{\infty}\int_{\phi=0}^{2\pi} \frac{n(x')e^{ik_\parallel\rho\cos(\phi)}}{|(x-x')^2 + \rho^2|}dx'\rho d\rho d\phi. \tag{6.56}$$

By using Bessel functions of first kind [86]

$$J_0(z) = \frac{1}{\pi}\int_0^\pi e^{iz\cos(\theta)}d\theta \tag{6.57}$$

and $J_0(-z) = J_0(z)$ the integral over ϕ can be solved.

$$\int_{\phi=0}^{2\pi} e^{ik_\parallel\rho\cos(\phi)}d\phi = 2\pi J_0(k_\parallel\rho) \tag{6.58}$$

Finally, by using

$$\int_0^\infty \rho(b^2 + \rho^2)^{-\frac{1}{2}}J_0(\rho)d\rho = e^{-|b|} \tag{6.59}$$

and substitution one has

$$V_H(x, y) = 2\pi e^{ik_\parallel y} \int n(x') \frac{1}{|k_\parallel|} e^{-|k_\parallel|(x-x')|} dx' \qquad (6.60)$$

$$= \int n(x') G_H(x, x', y) dx'. \qquad (6.61)$$

The Green's function then reads

> **Greens function for a 1D system in 3D**
>
> $$G_H(x, x', y) = \frac{2\pi}{|k_\parallel|} e^{ik_\parallel y} e^{-|k_\parallel|(x-x')|}. \qquad (6.62)$$

The gradient of the Greens function reads

$$\nabla_\mathbf{r} G_H(x, x', y) = \mathbf{a}(x, x') G_H(x, x', y) \qquad (6.63)$$

where

$$\mathbf{a}(x, x') \equiv \begin{pmatrix} -|k_\parallel|\mathrm{sign}(x - x') \\ ik_\parallel \\ 0 \end{pmatrix} \qquad (6.64)$$

using the sign-function.

An alternative derivation of the Hartree potentials is given in appendix A.4.

6.4.3. Transversal Magnetic Wave

Let us consider a simple system on that LR-TDCDFT can be applied. In Fig. 6.1 a transversal magnetic (TM) plane wave and the chosen coordinate system is sketched. For
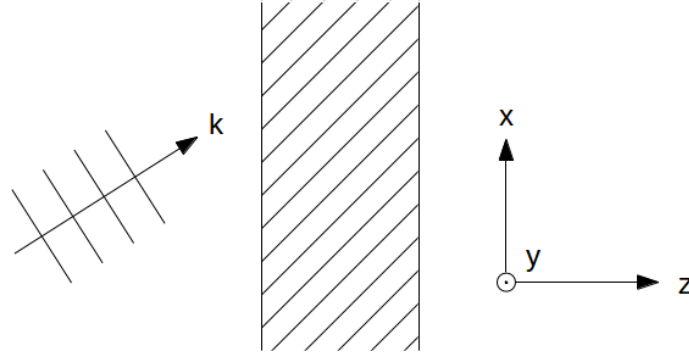
Figure 6.1.: TM-excitation of a slab geometry.

the coordinate system defined in the figure the magnetic induction of the **incident plane wave** reads

$$\mathbf{B} = B_0 e^{i(k_\parallel x + k_\perp z)} \hat{y} \qquad (6.65)$$

The magnetic induction **B** and the electric field **E** can be represented by the vector and scalar potentials, **A** and ϕ, respectively [32].

$$\mathbf{E} = -\frac{\partial}{\partial t}\mathbf{A} - \nabla\phi \qquad (6.66)$$

$$\mathbf{B} = \nabla \times \mathbf{A} \qquad (6.67)$$

Using Coulomb gauge

$$\nabla \cdot \mathbf{A} = 0, \tag{6.68}$$

assuming

$$\mathbf{A} = \mathbf{A}_0 e^{i(\mathbf{k}\cdot\mathbf{r}-\omega t)} \tag{6.69}$$

and

$$\mathbf{k} = \begin{pmatrix} k_\parallel \\ 0 \\ k_\perp \end{pmatrix} = k \begin{pmatrix} \sin(\theta) \\ 0 \\ \cos(\theta) \end{pmatrix} \tag{6.70}$$

where $k = |\mathbf{k}| = \frac{\omega}{c}\sqrt{\epsilon\mu}$, with ϵ being the electric permittivity and μ being the magnetic permeability of the corresponding material [1]. The vector potential of the incoming plane wave then reads

$$\mathbf{A} = \frac{iB_0 c}{\omega\sqrt{\epsilon\mu}} \begin{pmatrix} -\cos(\theta) \\ 0 \\ \sin(\theta) \end{pmatrix} e^{i(\mathbf{k}\cdot\mathbf{r}-\omega t)}. \tag{6.71}$$

A detailed derivation of the latter equation is given in Appendix A.5.

Further the equation

$$\mathbf{k} \times \mathbf{B} = \epsilon k_0 \mathbf{E} \tag{6.72}$$

is fulfilled for any electromagnetic wave [32]. By inserting Eqn. 6.65 into Eqn. 6.72 and using a wave vector $\mathbf{k}$ that lies in the xz-plane one has

$$\begin{pmatrix} k_\parallel \\ 0 \\ k_\perp \end{pmatrix} \times \begin{pmatrix} 0 \\ B_0 \\ 0 \end{pmatrix} = B_0 \begin{pmatrix} -k_\perp \\ 0 \\ k_\parallel \end{pmatrix} = \epsilon k_0 \mathbf{E}_0 \tag{6.73}$$

where $\mathbf{E} = \mathbf{E}_0 e^{i\left(k_\parallel x + k_\perp z\right)}$.

7. Quantum Tunneling - Results

> There are two possible outcomes: if
> the result confirms the hypothesis,
> then you've made a measurement. If
> the result is contrary to the
> hypothesis, then you've made a
> discovery.
>
> Enrico Fermi

In order to investigate tunneling charge plasmon resonances, the LR-TDCDFT has been implemented in a Matlab program. In this chapter the results of applying this program on different setups are shown. The chosen setups are sodium slabs and sodium double slabs. The choice of the setups is justified by the Kretschmann and Otto configurations, both being constructed using a metal-slab and an additional glass layer. These configurations show plasmon polariton resonances on their surface of the metal-slab. By setting up a double slab, a gap is present between both slabs. The aim of investigating such a system, is to observe quantum tunneling at the gap region and detecting a tunneling plasmon resonance. We concentrate on the Otto configuration, since we take the glass layer into account by using evanescent waves.

First, we start with plotting the ground state densities of the investigated setups. Then, the results of few feasibility studies are shown. Finally, the Otto configuration is simulated by the program, plots are shown and the results are discussed.

7.1. Ground State

First, we show plots of the ground state densities of the investigated systems, a sodium slab and a sodium double-slab, calculated using a DFT solver.
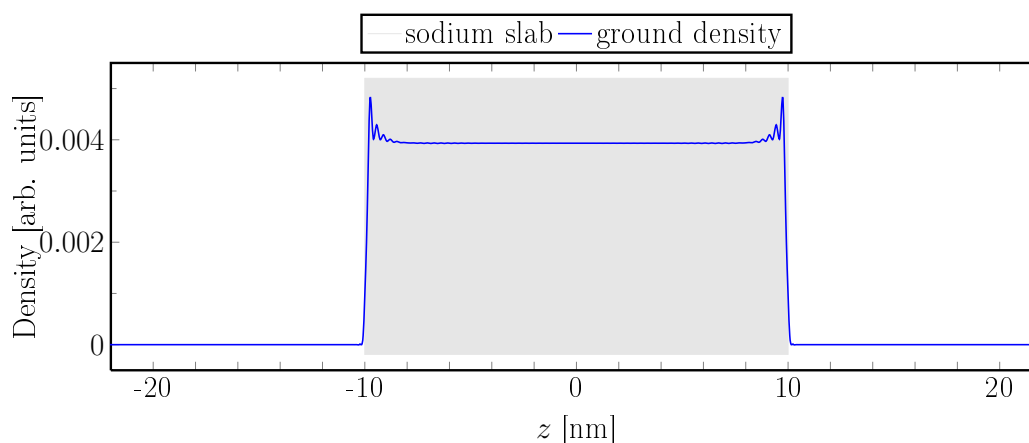
Figure 7.1.: DFT-simulated ground density of a sodium slab with 20 nm width. For sodium a Wigner-Seitz radius of $r_s = 3.93$ Bohr has been used.

7.1.1. Sodium Slab

In Fig. 7.1 the ground density of a 20 nm thick sodium slab, sketched in Fig. 6.1, is plotted. The location of the sodium slab relative to the z-position is represented by the gray area in the plot. For the DFT calculation the local density approximation (LDA) has been implemented. For sodium a Wigner-Seitz radius of $r_s = 3.93$ Bohr has been used.

7.1.2. Sodium Double-Slab

In Fig. 7.2 the ground density of a sodium double-slab is plotted. As in the single-slab calculation the gray areas represent the locations of the slabs. Again, LDA and $r_s = 3.93$ Bohr has been used.
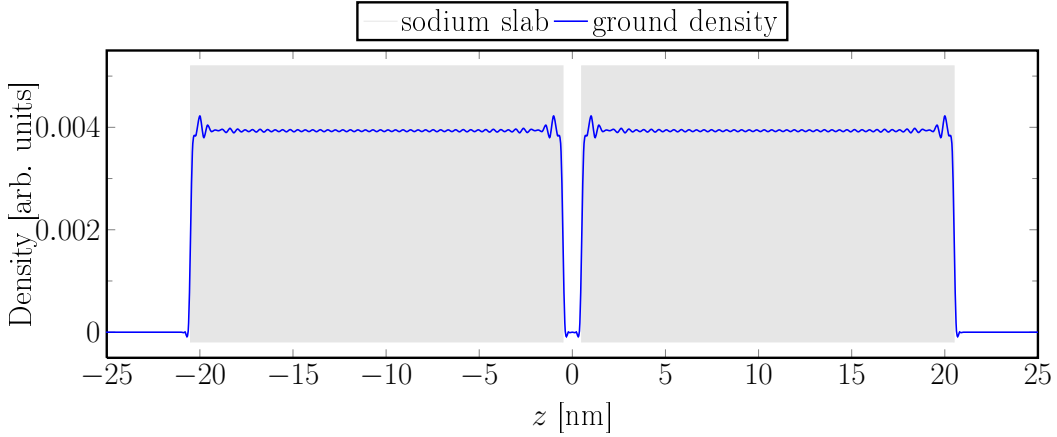
Figure 7.2.: DFT-simulated ground density of a sodium double slab, each with 20 nm width, separated by a 1 nm gap. For sodium a Wigner-Seitz radius of $r_s = 3.93$ Bohr has been used.

7.2. Testing Scenarios Using Plane-wave Excitation

In this section a brief feasibility study is given to validate the results as a verification of the implemented LR-TDCDFT by the fact that metals are usually transparent for hard UV light.

7.2.1. Sodium Slab

First a plane electromagnetic wave transmitting a sodium slab geometry, sketched in Fig. 6.1, is plotted. For waves with sufficiently high photon energies, only a tiny negligible part of the wave will be reflected at the slab and hence the slab will be transparent. In Fig. 7.3 a comparison of the z-components of the used external vector potential (see Appendix A.5) and the LR-TDCDFT-simulated vector potential of the sodium slab (20 nm width) is shown. The incoming plane wave has a wavelength of 14.14 nm, which is in the hard UV range. Due to the 45° incident angle the wavelength in z-direction will be stretched by a factor of $\sin(45°) = \sqrt{2}$. The external vector potential and the screened vector potential are in a good agreement. Hence the sodium slab is in a good approximation transparent to the applied incident wave. In Fig. 7.4 the angle of the incident wave is $45° + 180° = 225°$. Compared to Fig.7.3 the amplitude of the vector potential is multiplied by the factor minus one.
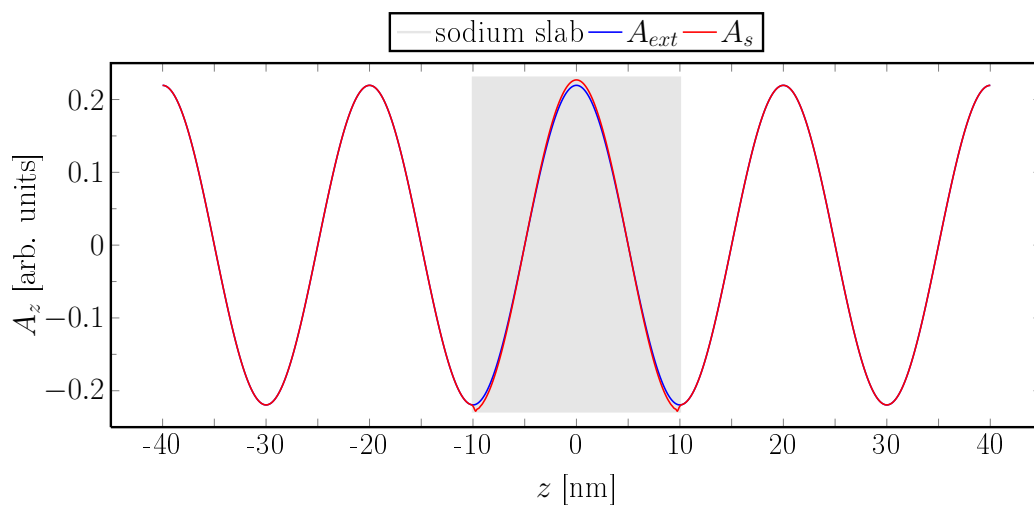
Figure 7.3.: LR-TDCDFT-simulated z-component of the screened vector potential of a sodium slab compared to the z-component of the external vector potential of the corresponding incident plane wave with an incident angle of 45° and a wavelength of 14.14 nm.
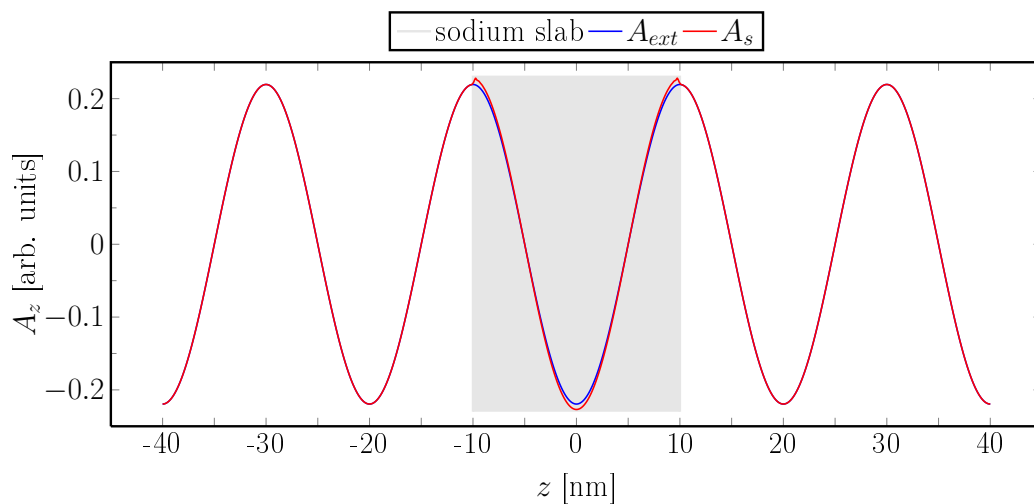
Figure 7.4.: Same as Fig.7.3, but with an incident angle of $45° + 180° = 225°$.

7.2.2. Sodium Double-Slab

We also applied the hard UV tests on the sodium double slab.
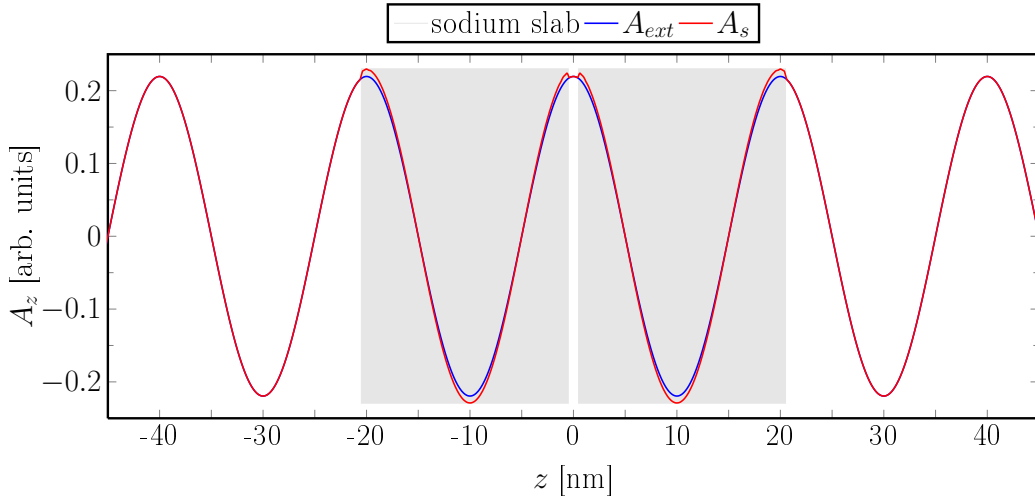
Figure 7.5.: LR-TDCDFT-simulated z-component of the screened vector potential of a sodium double-slab compared to the z-component of the external vector potential of the corresponding incident plane wave with an incident angle of 45° and a wavelength of 14.14 nm.

7.3. Vector potential

In this section we excite the investigated Otto geometries by applying light with wavelengths between 150 nm and 450 nm. In Fig. 7.6 the LR-TDCDFT-simulated absolute value of the z-component of the screened vector potential of a TM-excited Otto geometry containing a sodium slab is plotted. The external TM-wave enters the sodium slab with an incident angle of 45°. The sodium slab has a thickness of 20 nm. The surfaces of the slab are located at $z = -10$ nm and at $z = 10$ nm. The glass layer of the Otto geometry is taken into account by setting up the external vector potential as an evanescent wave (see Appendix A.6). In Fig. 7.7 a density-plot of the LR-TDCDFT-simulated absolute value of the z-component of the screened vector potential of a sodium slab is plotted. The air layer of the Otto geometry has a thickness of 200 nm.
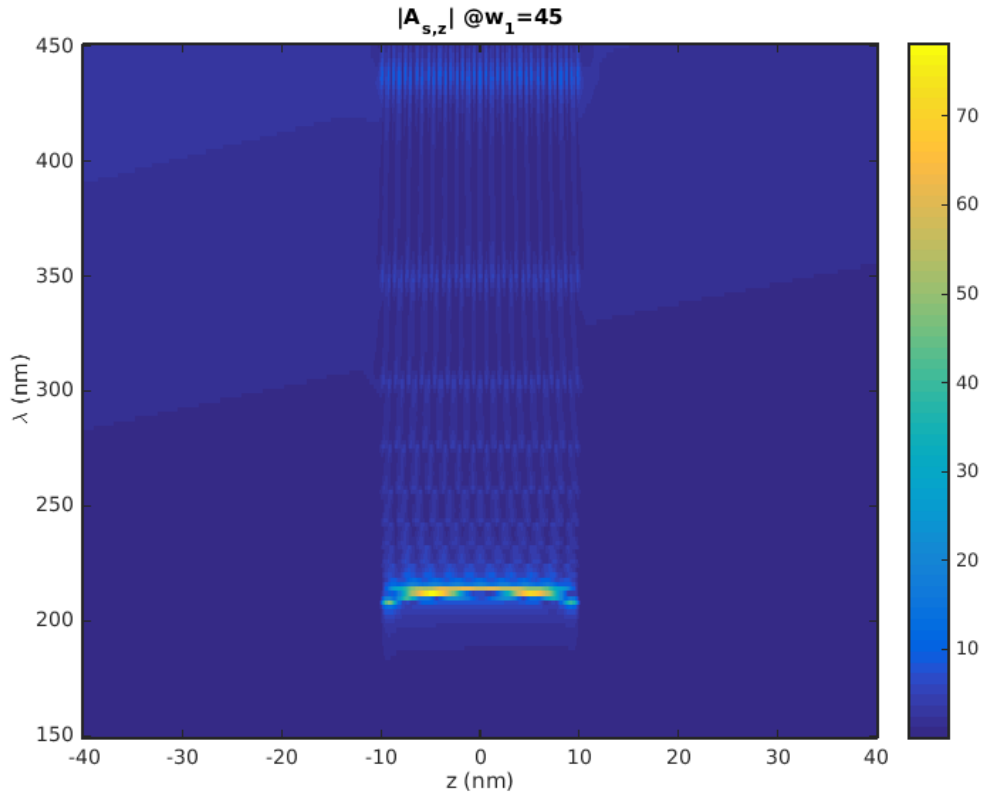
Figure 7.6.: LR-TDCDFT-simulated z-component of the screened vector potential of a sodium slab. The glass layer is indirectly taken into account by evanescent waves. A plane wave with an incident angle of 45° is taken.
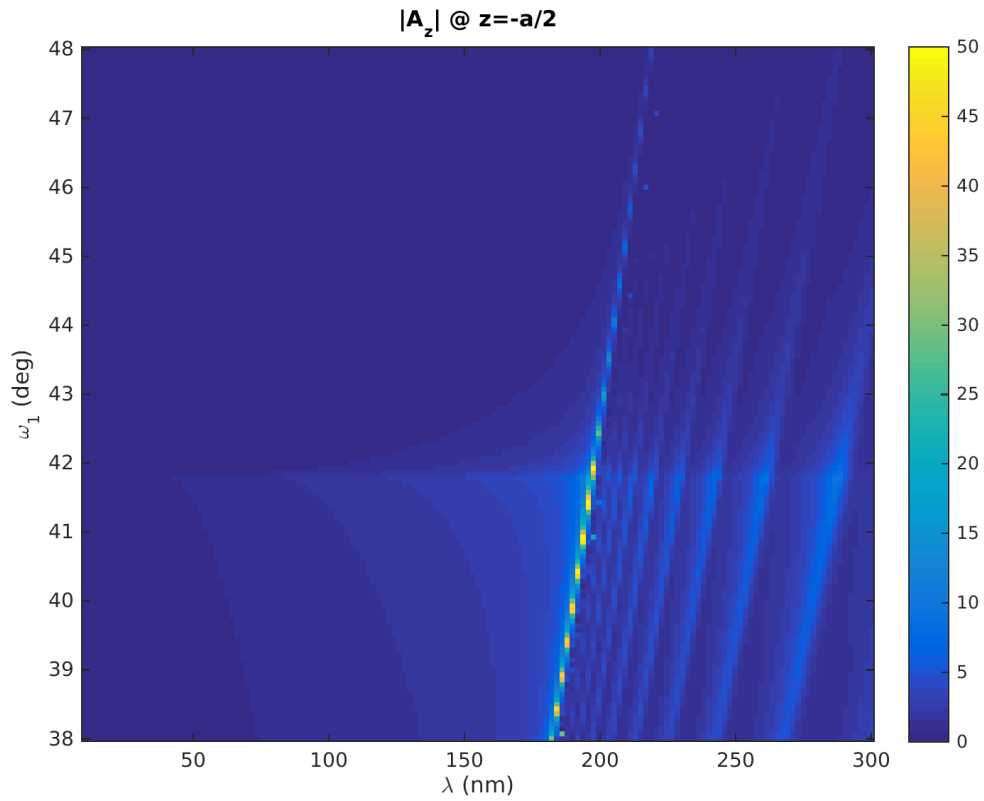
Figure 7.7.: LR-TDCDFT-simulated z-component of the screened vector potential of a sodium slab. The glass layer is indirectly taken into account by evanescent waves.

7.3.1. Discussion and Outlook

In the feasibility studies of the implemented LR-TDCDFT we have applied hard-UV light for testing the transparency of the sodium slab. The results of the simulations confirm the expected transparency of the slab for hard-UV light. Additionally we have performed calculations, where the exciting plane-wave is coming from the opposite site. This has been achieved by rotating the incident angle of the plane wave by 180°. The results of an incoming plane wave and the results of the same wave rotated by 180°, both exciting a sodium slab, show no difference, except the amplitudes of the z-component of the vector potential of Fig. 7.4 and Fig.7.3. They differ by the factor minus one.

However, detecting plasmon modes within the LR-TDCDFT simulations seems to be a quite challenging investigation. There has been no agreement by comparing the results of the transfer matrix method with that of the LR-TDCDFT.

We also have simulated sodium slabs for a different slab thickness of 5 nm, 2 nm and 1 nm. The resulting spectra showed all the same characteristics of the spectrum corresponding to a slab thickness of 20 nm.

In order to find possible reasons why the simulation using LR-TDCDFT does not give the results we have expected, we first discuss the simulation of the glass layer. The investigated system consists of an incoming plane wave partially transmitting a glass layer followed by an air and a metal layer. The glass layer of the Otto configuration has been simulated implicitly by setting the incident waves as evanescent waves. If there was a glass layer it would cause an incoming plane wave to appear as an evanescent wave in the air layer between the glass and metal layer (appendix A.6). It can not be excluded that there is an impact to the results by using such an implementation. A next step could be to control if unexpected results occur even without using evanescent waves, by comparing a transfer matrix method calculation of a simple sodium slab/layer without a glass layer with a LR-TDCDFT calculation of the same slab. For both simulations an incident plane wave excitation should be used.

One of the main differences could concern the energy levels which occur at the LR-TDCDFT calculations but not for transfer matrix method calculations. A next step could be to investigate the impact of the energy levels on the simulated spectra.

In Fig.7.6 one can recognize energy levels of higher intensities of the z-component of the screened vector potential. These levels correspond to the energy levels of the underlying DFT calculation of the sodium slab. It is possible that they dramatically change the results of the simulations.

Further progress could be achieved by analyzing the correlation functions of the investigated systems. They depend on the Green functions which have been calculated in Chapter 6.4.2. The used Green functions have one spatial dimension embedded in three spatial dimensions. A detailed investigation of the correlation functions could be one of the next steps.

A. Appendix

A.1. Landauer-Büttiker Formalism

This section is based on Paulsson's 'Introduction to the One Particle NEGF equations' [87].

The Landauer-Büttiker Formalism can be established from a Non-Equilibrium-Green's-Function (NEGF) method [88]. In this method the corresponding system is divided into three parts: two half-infinity leads which are connected via a center region (see Fig. 4.2). The NEGF provides to calculate the current through the center region. That could be for example the current through a molecule layer or the tunneling current through a small vacuum gap. With the division into these three parts the stationary Schrödinger equation of the system can be written

$$\begin{pmatrix} H_1 & H_{12} & H_{13} \\ H_{21} & H_2 & H_{23} \\ H_{31} & H_{32} & H_3 \end{pmatrix} \begin{pmatrix} |\psi_1\rangle \\ |\psi_2\rangle \\ |\psi_3\rangle \end{pmatrix} = E \begin{pmatrix} |\psi_1\rangle \\ |\psi_2\rangle \\ |\psi_3\rangle \end{pmatrix} \tag{A.1}$$

The indices $1, 2, 3$ denote the left electrode ($=1$), center region ($=2$) and the right electrode ($=3$). Furthermore H_1 is the Hamiltonian matrix and $|\psi_1\rangle$ is the wavefunction for the left electrode and so forth. The non diagonal Hamiltonian H_{12} describes the interaction between the left electrode and the center region and so forth. For sufficient large center regions the interactions between the left and right electrodes can be neglected $H_{13} = H_{31}^\dagger \approx 0$. By rewriting $\tau_1 \equiv H_{12} = H_{21}^\dagger$ and $\tau_3 \equiv H_{32} = H_{23}^\dagger$ Equ. A.1 becomes

$$\begin{pmatrix} H_1 & \tau_1 & 0 \\ \tau_1^\dagger & H_2 & \tau_3^\dagger \\ 0 & \tau_3 & H_3 \end{pmatrix} \begin{pmatrix} |\psi_1\rangle \\ |\psi_2\rangle \\ |\psi_3\rangle \end{pmatrix} = E \begin{pmatrix} |\psi_1\rangle \\ |\psi_2\rangle \\ |\psi_3\rangle \end{pmatrix} \tag{A.2}$$

Usually one defines the Green's function $G(E)$ for the full system

$$(E - H)G(E) = \mathbb{1} \tag{A.3}$$

Also, one can define the Green's function of each isolated subsystem

$$\forall i \in \{1, 2, 3\} : (E - H_i)g_i(E) = \mathbb{1} \tag{A.4}$$

For all Green's functions there is a retarded and an advanced solution. Both solutions can be obtained by adding an imaginary part to the energy.

$$E^R = E^+ = E + i\epsilon \tag{A.5}$$

$$E^A = E^- = E - i\epsilon \tag{A.6}$$

For the retarded (advanced) Green's function a positive (negative) imaginary part has to be added to the energy.

Using the retarded solution and rewriting Equ. A.3 with the use of Equ. A.2 leads to

$$\begin{pmatrix} E^+ - H_1 & -\tau_1 & 0 \\ -\tau_1^\dagger & E^+ - H_2 & -\tau_3^\dagger \\ 0 & -\tau_3 & E^+ - H_3 \end{pmatrix} \begin{pmatrix} G_1^+ & G_{12}^+ & G_{13}^+ \\ G_{21}^+ & G_2^+ & G_{23}^+ \\ G_{31}^+ & G_{32}^+ & G_3^+ \end{pmatrix} = \begin{pmatrix} \mathbb{1} & 0 & 0 \\ 0 & \mathbb{1} & 0 \\ 0 & 0 & \mathbb{1} \end{pmatrix} \tag{A.7}$$

Using the equations of the second column allows to calculate the Green's function G_2 of the center region without calculating the full Green's function.

$$(E^+ - H_1)G_{12}^+ - \tau_1 G_2^+ = 0 \tag{A.8}$$

$$-\tau_1^\dagger G_{12}^+ + (E^+ - H_2)G_2^+ - \tau_3^\dagger G_{32}^+ = \mathbb{1} \tag{A.9}$$

$$-\tau_3 G_2^+ + (E^+ - H_3)G_{32}^+ = 0 \tag{A.10}$$

Eqs. A.8 and A.10 can be rewritten

$$G_{12}^+ = g_1^+ \tau_1 G_2^+ \tag{A.11}$$

$$G_{32}^+ = g_3^+ \tau_3 G_2^+ \tag{A.12}$$

Equ. A.9 reads then

$$-\tau_1^\dagger g_1^+ \tau_1 G_2^+ + (E^+ - H_2)G_2^+ - \tau_3^\dagger g_3^+ \tau_3 G_2^+ = \mathbb{1} \tag{A.13}$$

The Green's function of the center region is

$$G_2^+ = (E^+ - H_2 - \Sigma_1^+ - \Sigma_3^+)^{-1} \tag{A.14}$$

where $\Sigma_1^+ \equiv \tau_1^\dagger g_1^+ \tau_1$ and $\Sigma_3^+ \equiv \tau_3^\dagger g_3^+ \tau_3$ are the self-energies of the left and right electrode respectively.

A.1.1. Spectral function

The expansion of G in the eigenbasis of the Hamiltonian H reads

$$G = \frac{1}{E^+ - H} = \frac{1}{E + i\epsilon - H} = \sum_n \frac{|n\rangle\langle n|}{E + i\epsilon - E_n} \tag{A.15}$$

The spectral function can be defined

$$
\begin{aligned}
A &\equiv i\left(G - G^\dagger\right) \\
&= i\left(\frac{1}{E + i\epsilon - H} - \frac{1}{E - i\epsilon - H}\right) \\
&= \sum_n |n\rangle\langle n| \frac{2\epsilon}{(E - E_n)^2 + \epsilon^2}
\end{aligned} \tag{A.16}
$$

The limes $\epsilon \mapsto 0$ of the Cauchy-function $\frac{1}{\pi}\frac{\epsilon}{(x-t)^2+\epsilon^2}$ is the Delta function $\delta(x - t)$. Hence the spectral function reads

$$A = 2\pi \sum_n \delta(E - E_n)|n\rangle\langle n| \tag{A.17}$$

A.1.2. Response wavefunction

Consider an incoming wave $|\psi_{in}\rangle$ from left. It will cause a retarded response of the whole system $|\psi^R\rangle$. In total the wavefunction is the sum of both parts $|\psi_{in}\rangle + |\psi^R\rangle$ and must fulfill the Schrödinger equation.

$$H\left(|\psi_{in}\rangle + |\psi^R\rangle\right) = E^+\left(|\psi_{in}\rangle + |\psi^R\rangle\right)$$

$$
\begin{pmatrix} H_1 & \tau_1 & 0 \\ \tau_1^\dagger & H_2 & \tau_3^\dagger \\ 0 & \tau_3 & H_3 \end{pmatrix}
\left(\begin{pmatrix} |\psi_{in,1}\rangle \\ |\psi_{in,2}\rangle \\ |\psi_{in,3}\rangle \end{pmatrix} + \begin{pmatrix} |\psi_1^R\rangle \\ |\psi_2^R\rangle \\ |\psi_3^R\rangle \end{pmatrix}\right)
= E^+ \left(\begin{pmatrix} |\psi_{in,1}\rangle \\ |\psi_{in,2}\rangle \\ |\psi_{in,3}\rangle \end{pmatrix} + \begin{pmatrix} |\psi_1^R\rangle \\ |\psi_2^R\rangle \\ |\psi_3^R\rangle \end{pmatrix}\right) \tag{A.18}
$$

Further one considers such incoming waves which are fully reflected at the end of the left electrode. For such an incoming wave $|\psi_{in,2}\rangle = |\psi_{in,3}\rangle = 0$. Now the Schrödinger equation is

$$\begin{pmatrix} H_1|\psi_{in,1}\rangle \\ \tau_1^\dagger|\psi_{in,1}\rangle \\ 0 \end{pmatrix} + H|\psi^R\rangle = E^+ \begin{pmatrix} |\psi_{in,1}\rangle \\ 0 \\ 0 \end{pmatrix} + E^+|\psi^R\rangle \tag{A.19}$$

The second row gives the solution of the retarded response

$$(E^+ - H)|\psi^R\rangle = \tau_1^\dagger|\psi_{in,1}\rangle$$
$$|\psi^R\rangle = G^+\tau_1^\dagger|\psi_{in,1}\rangle \tag{A.20}$$

Since the incoming wave is fully reflected, the wavefunction of the center region contains a response part only

$$|\psi_2\rangle = G_2^+\tau_1^\dagger|\psi_{in,1}\rangle \tag{A.21}$$

Using the first row of Equ. A.2 one gets

$$|\psi_1\rangle = g_1^+\tau_1|\psi_2\rangle \tag{A.22}$$

and for the third row of Equ. A.2 one gets

$$|\psi_3\rangle = g_3^+\tau_3|\psi_2\rangle \tag{A.23}$$

With Eqs. A.22 and A.23 one can obtain the wavefunction of the left and the wavefunction of the right part

$$|\psi_1\rangle = \left(1 + g_1^+\tau_1 G_2^+\tau_1^\dagger\right)|\psi_{in,1}\rangle \tag{A.24}$$

$$|\psi_3\rangle = g_3^+\tau_3 G_2^+\tau_1^\dagger|\psi_{in,1}\rangle \tag{A.25}$$

Notice, that to the left part the incoming wave has been added.

A.1.3. Electric current through center region

The probability to find an electron at the center region is given by the sum

$$P = \sum_j |\psi_j|^2 \tag{A.26}$$

where j labels the energy levels of the center region. For a system in equilibrium the probability P is conserved.

$$0 = \frac{\partial P}{\partial t} = \frac{\partial}{\partial t}\sum_j |\psi_j|^2 = \sum_j \frac{\partial\langle\psi|j\rangle\langle j|\psi\rangle}{\partial t}$$

$$= \sum_j \left(\underbrace{\frac{\partial\langle\psi|j\rangle}{\partial t}}_{=\frac{i}{\hbar}\langle\psi|H|j\rangle}\langle j|\psi\rangle + \langle\psi|j\rangle \underbrace{\frac{\partial\langle j|\psi\rangle}{\partial t}}_{=-\frac{i}{\hbar}\langle j|H|\psi\rangle} \right)$$

$$= \frac{i}{\hbar}\sum_j \left(\langle\psi|H|j\rangle\langle j|\psi\rangle - \langle\psi|j\rangle\langle j|H|\psi\rangle\right)$$

$$= \frac{i}{\hbar}\left(\langle\psi|H|\psi_2\rangle - \langle\psi_2|H|\psi\rangle\right) \tag{A.27}$$

A. Appendix

The full wavefunction ψ has been projected onto the energy level expansion of the center region, which equals the center region wavefunction $|\psi_2\rangle = \sum_j |j\rangle\langle j|\psi\rangle$. The matrix element of the first expression reads

$$
\langle\psi|H|\psi_2\rangle = \begin{pmatrix} \langle\psi_1| \\ \langle\psi_2| \\ \langle\psi_3| \end{pmatrix} \begin{pmatrix} H_1 & \tau_1 & 0 \\ \tau_1^\dagger & H_2 & \tau_3^\dagger \\ 0 & \tau_3 & H_3 \end{pmatrix} \begin{pmatrix} 0 \\ |\psi_2\rangle \\ 0 \end{pmatrix}
$$
$$
= \langle\psi_1|\tau_1|\psi_2\rangle + \langle\psi_2|H_2|\psi_2\rangle + \langle\psi_3|\tau_3|\psi_2\rangle \tag{A.28}
$$

and the matrix element of the second expression reads

$$
\langle\psi_2|H|\psi\rangle = \begin{pmatrix} 0 \\ \langle\psi_2| \\ 0 \end{pmatrix} \begin{pmatrix} H_1 & \tau_1 & 0 \\ \tau_1^\dagger & H_2 & \tau_3^\dagger \\ 0 & \tau_3 & H_3 \end{pmatrix} \begin{pmatrix} |\psi_1\rangle \\ |\psi_2\rangle \\ |\psi_3\rangle \end{pmatrix}
$$
$$
= \langle\psi_2|\tau_1^\dagger|\psi_1\rangle + \langle\psi_2|H_2|\psi_2\rangle + \langle\psi_2|\tau_3^\dagger|\psi_3\rangle \tag{A.29}
$$

Substitution into the temporal derivative of the probability P gives

$$
0 = \frac{\partial P}{\partial t} = \frac{i}{\hbar}\left(\langle\psi_1|\tau_1|\psi_2\rangle - \langle\psi_2|\tau_1^\dagger|\psi_1\rangle\right) + \frac{i}{\hbar}\left(\langle\psi_3|\tau_3|\psi_2\rangle - \langle\psi_2|\tau_3^\dagger|\psi_3\rangle\right) \tag{A.30}
$$

The first part multiplied by the electron charge $(-e)$

$$
i_{3\to1} \equiv -\frac{ie}{\hbar}\left(\langle\psi_1|\tau_1|\psi_2\rangle - \langle\psi_2|\tau_1^\dagger|\psi_1\rangle\right) \tag{A.31}
$$

is the electric current for an incoming electron moving from right to left. The second part multiplied by the electron charge $(-e)$

$$
i_{1\to3} \equiv -\frac{ie}{\hbar}\left(\langle\psi_3|\tau_3|\psi_2\rangle - \langle\psi_2|\tau_3^\dagger|\psi_3\rangle\right) \tag{A.32}
$$

is the electric current for an incoming electron moving from left to right. Further one can rewrite the current $i_{1\to3}$ by using Eqs. A.21 and A.25

$$
\begin{aligned}
i_{1\to3} &= -\frac{ie}{\hbar}\left(\langle\psi_3|\tau_3|\psi_2\rangle - \langle\psi_2|\tau_3^\dagger|\psi_3\rangle\right) \\
&= -\frac{ie}{\hbar}\left(\langle\psi_{in,1}|\tau_1 G_2^{+\dagger}\tau_3^\dagger g_3^{+\dagger}\tau_3 G_2^+\tau_1^\dagger|\psi_{in,1}\rangle - \right. \\
&\qquad\qquad \left. \langle\psi_{in,1}|\tau_1 G_2^{+\dagger}\tau_3^\dagger g_3^+\tau_3 G_2^+\tau_1^\dagger|\psi_{in,1}\rangle\right) \\
&= -\frac{ie}{\hbar}\left(\langle\psi_{in,1}|\tau_1 G_2^{+\dagger}\tau_3^\dagger(g_3^{+\dagger} - g_3^+)\tau_3 G_2^+\tau_1^\dagger|\psi_{in,1}\rangle\right) \\
&= \frac{e}{\hbar}\langle\psi_{in,1}|\tau_1 G_2^{+\dagger}\Gamma_3^+ G_2^+\tau_1^\dagger|\psi_{in,1}\rangle \tag{A.33}
\end{aligned}
$$

where $\Gamma_3^+ = -i\tau_3^\dagger(g_3^{+\dagger} - g_3^+)\tau_3$. The current from left to right can be obtained by summarising over all incoming waves $|\psi_{in,1,n}\rangle$ which are reflected at the end of the left part.

$$
\begin{aligned}
I_{1\to3} &= 2\frac{e}{\hbar}\sum_n f(E_n,\mu_1)\langle\psi_{in,1,n}|\tau_1 G_2^{+\dagger}\Gamma_3^+ G_2^+\tau_1^\dagger|\psi_{in,1,n}\rangle \\
&= 2\frac{e}{\hbar}\int f(E,\mu_1)\sum_n \delta(E-E_n)\langle\psi_{in,1,n}|\tau_1 G_2^{+\dagger}\Gamma_3^+ G_2^+\tau_1^\dagger|\psi_{in,1,n}\rangle dE \tag{A.34}
\end{aligned}
$$

The factor 2 describes the spin of the electron. In order to write the current as a useful expression, one can use the partition of the unit and Equ. A.17.

$$I_{1\to 3} = 2\frac{e}{\hbar} \int f(E - \mu_L) \sum_n \delta(E - E_n)\langle \psi_{in,1,n}|\tau_1 \mathbb{1} G_2^{+\dagger}\Gamma_3^+ G_2^+ \tau_1^\dagger|\psi_{in,1,n}\rangle dE$$

$$= 2\frac{e}{\hbar} \int f(E - \mu_L) \sum_{m,n} \delta(E - E_n)\langle \psi_{in,1,n}|\tau_1|m\rangle\langle m|G_2^{+\dagger}\Gamma_3^+ G_2^+ \tau_1^\dagger|\psi_{in,1,n}\rangle dE$$

$$= 2\frac{e}{\hbar} \int f(E - \mu_L) \sum_{m} \langle m|G_2^{+\dagger}\Gamma_3^+ G_2^+ \tau_1^\dagger \cdot$$

$$\left(\sum_n \delta(E - E_n)|\psi_{in,1,n}\rangle\langle \psi_{in,1,n}| \right) \tau_1|m\rangle dE$$

$$= 2\frac{e}{\hbar} \int f(E - \mu_L) \sum_{m} \langle m|G_2^{+\dagger}\Gamma_3^+ G_2^+ \tau_1^\dagger \frac{a_1^+}{2\pi}\tau_1|m\rangle dE$$

$$= \frac{2e}{h} \int f(E - \mu_L)\mathrm{Tr}\left(G_2^{+\dagger}\Gamma_3^+ G_2^+ \Gamma_1 \right) dE \tag{A.35}$$

where $f(x) = \frac{1}{1+\exp\{\frac{x}{k_B T}\}}$ and $\Gamma_1^+ = \tau_1^\dagger a_1^+ \tau_1 = -i\tau_1^\dagger(g_1^{+\dagger} - g_1^+)\tau_1$. For the current from right to left one considers an incoming wave from the right side. One can set $|\psi_{in,1}\rangle = |\psi_{in,2}\rangle = 0$ and rewrite the second row of Equ. A.18. Further the total wavefunction reads

$$\begin{pmatrix} |\psi_1\rangle \\ |\psi_2\rangle \\ |\psi_3\rangle \end{pmatrix} = \begin{pmatrix} g_1^+\tau_1 G_2^+ \tau_3^\dagger|\psi_{in,3}\rangle \\ G_2^+ \tau_3^\dagger|\psi_{in,3}\rangle \\ g_3^+\tau_3 G_2^+ \tau_3^\dagger|\psi_{in,3}\rangle \end{pmatrix} \tag{A.36}$$

and one can write

$$i_{3\to 1} = -\frac{ie}{\hbar}\left(\langle\psi_1|\tau_1|\psi_2\rangle - \langle\psi_2|\tau_1^\dagger|\psi_1\rangle \right)$$

$$= -\frac{ie}{\hbar}\left(\langle\psi_{in,3}|\tau_3 G_2^{+\dagger}\tau_1^\dagger g_1^{+\dagger}\tau_1 G_2^+ \tau_3^\dagger|\psi_{in,3}\rangle - \langle\psi_{in,3}|\tau_3 G_2^{+\dagger}\tau_1^\dagger g_1^+ \tau_1 G_2^+ \tau_3^\dagger|\psi_{in,3}\rangle \right)$$

$$= -\frac{ie}{\hbar}\left(\langle\psi_{in,3}|\tau_3 G_2^{+\dagger}\tau_1^\dagger (g_1^{+\dagger} - g_1^+)\tau_1 G_2^+ \tau_3^\dagger|\psi_{in,3}\rangle \right)$$

$$= \frac{e}{\hbar}\langle\psi_{in,3}|\tau_3 G_2^{+\dagger}\Gamma_1^+ G_2^+ \tau_3^\dagger|\psi_{in,3}\rangle \tag{A.37}$$

The current from right to left is

$$I_{3\to 1} = 2\frac{e}{\hbar} \int f(E - \mu_R) \sum_n \delta(E - E_n)\langle \psi_{in,3,n}|\tau_3 G_2^{+\dagger}\Gamma_1^+ G_2^+ \tau_3^\dagger|\psi_{in,3,n}\rangle dE$$

$$= \frac{2e}{h} \int f(E - \mu_R)\mathrm{Tr}\left(G_2^{+\dagger}\Gamma_3^+ G_2^+ \Gamma_1 \right) dE \tag{A.38}$$

The total current from left to right is the difference

$$I = I_{1\to 3} - I_{3\to 1}$$

$$= \frac{2e}{h} \int \left(f(E - \mu_L) - f(E - \mu_R) \right)\mathrm{Tr}\left(G_2^{+\dagger}\Gamma_3^+ G_2^+ \Gamma_1 \right) dE \tag{A.39}$$

A comparison with Eqn. 4.20 gives an expression for the transmission function

$$T(E) = \mathrm{Tr}\left(G_2^{+\dagger}\Gamma_3^+ G_2^+ \Gamma_1 \right) \tag{A.40}$$

A.2. Longitudinal and Transversal Current

A current $\mathbf{J}(\mathbf{r}, t)$ can be separated into a longitudinal and a transversal part [32].

$$\mathbf{J}(\mathbf{r}, t) = \mathbf{J}_L(\mathbf{r}, t) + \mathbf{J}_T(\mathbf{r}, t) \tag{A.41}$$

The longitudinal part reads

$$\mathbf{J}_L(\mathbf{r}, t) = -\frac{1}{4\pi}\nabla \int \frac{\nabla \cdot \mathbf{J}(\mathbf{r}', t)}{|\mathbf{r} - \mathbf{r}'|} d\tau' \tag{A.42}$$

and the transversal part reads

$$\mathbf{J}_T(\mathbf{r}, t) = \frac{1}{4\pi}\nabla \times \left(\nabla \times \int \frac{\mathbf{J}(\mathbf{r}', t)}{|\mathbf{r} - \mathbf{r}'|} d\tau' \right) \tag{A.43}$$

By applying the continuity equation

$$\nabla \cdot \mathbf{J}(\mathbf{r}, t) = -\frac{\partial \rho(\mathbf{r}, t)}{\partial t} = i\omega \rho(\mathbf{r}, t) \tag{A.44}$$

where $\rho(\mathbf{r}, t) = \rho(\mathbf{r})e^{-i\omega t}$ has been used, the longitudinal part can be expressed by

$$\mathbf{J}_L(\mathbf{r}, t) = -\frac{1}{4\pi}\nabla \int \frac{i\omega \rho(\mathbf{r}', t)}{|\mathbf{r} - \mathbf{r}'|} d\tau' = -\frac{i\omega}{4\pi}\nabla V_H(\mathbf{r}, t) \tag{A.45}$$

and further the transversal current can be expressed by

$$\mathbf{J}_T(\mathbf{r}, t) = \mathbf{J}(\mathbf{r}, t) - \mathbf{J}_L(\mathbf{r}, t) = \mathbf{J}(\mathbf{r}, t) + \frac{i\omega}{4\pi}\nabla V_H(\mathbf{r}, t) \tag{A.46}$$

A.3. Linear Response Theory

First, we start with a stationary system. Let H_0 be the Hamiltonian of the stationary system. The stationary Schrödinger equation reads $H_0\psi = E\psi$. The density reads then $\rho_0 = |\psi\rangle\langle\psi|$. Let E_n be the energy eigenvalues and let $|n\rangle$ be the eigenstates forming an orthonormal basis set $\{|n\rangle \big| n \in \mathbb{N}_0\}$. Then for a pure state $|n\rangle$ it follows $H_0|n\rangle = E_n|n\rangle$.

Now, let us consider a perturbed system

$$H = H_0 + H' = H_0 - AK(t) \tag{A.47}$$

where K is the force corresponding to the perturbation [84]. The density can be separated into two parts $\rho = \rho_0 + \delta\rho$, the stationary part ρ_0 and the response part caused by H'. The time evolution of the density ρ is given by the von Neumann[1] equation

$$i\dot{\rho} = [H, \rho] = H\rho - \rho H \tag{A.48}$$

For the stationary system the von Neumann equation reads $i\dot{\rho}_0 = [H_0, \rho_0]$. We assume that the perturbation is small and keep only linear terms. All terms of higher orders are neglected, e.g. $[H', \delta\rho] \simeq 0$. The time evolution of ρ reads

$$i\dot{\rho} = [H, \rho] \tag{A.49}$$
$$i(\dot{\rho}_0 + \delta\dot{\rho}) = [H_0 + H', \rho_0 + \delta\rho] \tag{A.50}$$
$$= \underbrace{[H_0, \rho_0]}_{=i\dot{\rho}_0} + [H', \rho_0] + [H_0, \delta\rho] + \underbrace{[H', \delta\rho]}_{\simeq 0} \tag{A.51}$$
$$i\delta\dot{\rho} = [H', \rho_0] + [H_0, \delta\rho] \tag{A.52}$$

where $[H', \rho_0]$ describes the propagation of $\delta\rho$.

The time-dependent Schrödinger equation reads

$$i\dot{\psi} = H_0\psi + H'\psi. \tag{A.53}$$

Switching to the interaction picture[2] one gets $\psi_I = e^{iH_0 t}\psi = U_0\psi$ and further $\psi = e^{-iH_0 t}\psi_I = U_0^+\psi_I$. Inserting the latter expression into Eqn. A.53 gives

$$i\dot{\psi} = H_0\psi + H'\psi \tag{A.54}$$
$$i\left(-iH_0 e^{-iH_0 t}\psi_I + e^{-iH_0 t}\dot{\psi}_I\right) = (H_0 + H')e^{-iH_0 t}\psi_I \tag{A.55}$$
$$i\dot{\psi}_I = e^{iH_0 t}H'e^{-iH_0 t}\psi_I \tag{A.56}$$
$$i\dot{\psi}_I = H_I'\psi_I \tag{A.57}$$

In the interaction picture the density reads $\rho_I = U_0^+\rho U_0$ and further $\rho = U_0\rho_I U_0^+$. The time evolution of $\delta\rho$ is given by

$$i\delta\dot{\rho} = i\partial_t\left(U_0\delta\rho_I U_0^+\right) \tag{A.58}$$
$$[H', \rho_0] + [H_0, \delta\rho] = H_0\delta\rho + U_0 i\delta\dot{\rho}_I U_0^+ - \delta\rho H_0 \tag{A.59}$$
$$[H', \rho_0] = U_0 i\delta\dot{\rho}_I U_0^+ \tag{A.60}$$

---

[1]John von Neumann, Hungarian mathematician, physicist and computer scientist, *1903, +1957.
[2]Be not confused with the related Heisenberg picture $\psi_H = e^{iHt}\psi$.

A. Appendix

Continuing by switching left and right hand side of the latter equation gives

$$i\delta\dot{\rho}_I = U_0^+[H',\rho_0]U_0 \tag{A.61}$$
$$= U_0^+ \left(H'U_0U_0^+\rho_0 - \rho_0U_0U_0^+H' \right) U_0 \tag{A.62}$$
$$= \left(U_0^+H'U_0U_0^+\rho_0U_0 - U_0^+\rho_0U_0U_0^+H'U_0 \right) \tag{A.63}$$
$$= \left(H_I'U_0^+\rho_0U_0 - U_0^+\rho_0U_0H_I' \right) \tag{A.64}$$
$$= \left(H_I'\rho_0 - \rho_0H_I' \right) \tag{A.65}$$
$$= [H_I',\rho_0] \tag{A.66}$$
$$\delta\rho_I(t) - \delta\rho_I(t_0) = -i\int_{t_0}^{t}[H_I'(t'),\rho_0]dt' \tag{A.67}$$

Let $B(t)$ be a physical quantity of the considered system. The expectation value $\langle B(t)\rangle$ can be written by using the trace function and the density operator

$$\langle B(t)\rangle = \text{tr}\{\rho(t)B(t)\} \tag{A.68}$$
$$= \text{tr}\{(\delta\rho(t)+\rho_0)B(t)\} \tag{A.69}$$
$$= \text{tr}\{\delta\rho(t)B(t)\} + \text{tr}\{\rho_0B(t)\} \tag{A.70}$$
$$= \text{tr}\{\delta\rho(t)B(t)\} + \langle B(t)\rangle_0 \tag{A.71}$$

Further one gets

$$\langle B(t)\rangle - \langle B(t)\rangle_0 = \text{tr}\{\delta\rho(t)B(t)\} \tag{A.72}$$
$$= \text{tr}\left\{ U_0U_0^+\delta\rho(t)U_0U_0^+B(t) \right\} \tag{A.73}$$
$$= \text{tr}\left\{ U_0^+\delta\rho(t)U_0U_0^+B(t)U_0 \right\} \tag{A.74}$$
$$= \text{tr}\left\{ \delta\rho_I(t)B_I(t) \right\} \tag{A.75}$$

By utilizing Eqn. A.67 and assuming that $\text{tr}\{\delta\rho_I(t_0)B_I(t)\} = 0$ one gets

$$\langle B(t)\rangle - \langle B(t)\rangle_0 = \text{tr}\left\{ \delta\rho_I(t)B_I(t) \right\} \tag{A.76}$$
$$= \text{tr}\{\delta\rho_I(t_0)B_I(t)\} - i\int_{t_0}^{t}\text{tr}\left\{ [H_I'(t'),\rho_0]B_I(t) \right\}dt' \tag{A.77}$$
$$= i\int_{t_0}^{t}\text{tr}\left\{ [A_I(t')K(t'),\rho_0]B_I(t) \right\}dt' \tag{A.78}$$
$$= i\int_{t_0}^{t}\text{tr}\left\{ A_I(t')K(t')\rho_0B_I(t) - \rho_0A_I(t')K(t')B_I(t) \right\}dt' \tag{A.79}$$
$$= i\int_{t_0}^{t}\text{tr}\left\{ A_I(t')\rho_0B_I(t) - \rho_0A_I(t')B_I(t) \right\}K(t')dt' \tag{A.80}$$
$$= i\int_{t_0}^{t}\text{tr}\left\{ \rho_0B_I(t)A_I(t') - \rho_0A_I(t')B_I(t) \right\}K(t')dt' \tag{A.81}$$
$$= i\int_{t_0}^{t}\text{tr}\left\{ \rho_0[B_I(t),A_I(t')] \right\}K(t')dt' \tag{A.82}$$

This leads directly to the definition of the correlation function

Correlation Function

$$\chi_{AB}(t,t') \equiv i\theta(t-t')\text{tr}\left\{ \rho_0[A_I(t),B_I(t')] \right\} \quad \text{(A.83)}$$

Further one can show that $\chi_{AB}(t,t') = \chi_{AB}(t-t')$. Additionally, the Heaviside step function $\theta(t-t') \equiv \begin{cases} 1 \text{ for } x > 0 \\ 0 \text{ for } x \le 0 \end{cases}$ has been introduced to ensure the causality principle[3].
The linear response of the quantity B is given by

$$\delta\langle B(t)\rangle = \langle B(t)\rangle - \langle B(t)\rangle_0 = \int_{t_0}^{t} \chi_{BA}(t-t')K(t')dt'. \tag{A.84}$$

Using $\tau = t - t'$ the Fourier-transform of the correlation function reads

$$\chi_{AB}(\omega) = \int_0^\infty \chi_{AB}(\tau)e^{-i\omega\tau}d\tau. \tag{A.85}$$

where the integral starts from zero instead of minus infinity because the integrand is zero for negative τ due to the Heaviside step function. Further we consider adiabatic turn-on and insert an infinitesimal $\eta \to 0^+$.

$$\chi_{AB}(\omega) = i\int_0^\infty \mathrm{tr}\Big\{\rho_0[A_I(t), B_I(t')]\}\Big\}e^{-i(\omega+i\eta)\tau}d\tau \tag{A.86}$$

$$= i\int_0^\infty \mathrm{tr}\Big\{\rho_0\Big(A_I(t)B_I(t') - B_I(t')A_I(t)\Big)\Big\}e^{-i(\omega+i\eta)\tau}d\tau \tag{A.87}$$

Next we use the orthonormal eigenstate basis set $\big\{|n\rangle\big|n \in \mathbb{N}_0\big\}$ and write the density of the stationary system as $\rho_0 = \sum_n f_n|n\rangle\langle n|$ where f is the distribution function, e.g. Fermi-Dirac distribution.

$$\chi_{AB}(\omega) = i\int_0^\infty \mathrm{tr}\Big\{\sum_m f_m|m\rangle\langle m|A_I(t)B_I(t') - \sum_n f_n|n\rangle\langle n|B_I(t')A_I(t)\Big\}e^{-i(\omega+i\eta)\tau}d\tau \tag{A.88}$$

$$= i\int_0^\infty \mathrm{tr}\Big\{\sum_m f_m\langle m|U_0^+(t)AU_0(t)U_0^+(t')BU_0(t')|m\rangle$$
$$- \sum_n f_n\langle n|U_0^+(t')BU_0(t')U_0^+(t)AU_0(t)|n\rangle\Big\}e^{-i(\omega+i\eta)\tau}d\tau \tag{A.89}$$

Inserting twice the identity $\sum_n |n\rangle\langle n| = 1$ we get

$$\chi_{AB}(\omega) = i\int_0^\infty \Big\{\sum_m f_m\langle m|U_0^+(t)AU_0(t)\sum_n |n\rangle\langle n|U_0^+(t')BU_0(t')|m\rangle$$
$$- \sum_n f_n\langle n|U_0^+(t')BU_0(t')\sum_m |m\rangle\langle m|U_0^+(t)AU_0(t)|n\rangle\Big\}e^{-i(\omega+i\eta)\tau}d\tau \tag{A.90}$$

$$= i\int_0^\infty \sum_{m,n} \Big\{f_m\langle m|U_0^+(t)AU_0(t)|n\rangle\langle n|U_0^+(t')BU_0(t')|m\rangle$$
$$- f_n\langle n|U_0^+(t')BU_0(t')|m\rangle\langle m|U_0^+(t)AU_0(t)|n\rangle\Big\}e^{-i(\omega+i\eta)\tau}d\tau \tag{A.91}$$

$$= i\int_0^\infty \sum_{m,n} (f_m - f_n)\langle m|U_0^+(t)AU_0(t)|n\rangle\langle n|U_0^+(t')BU_0(t')|m\rangle e^{-i(\omega+i\eta)\tau}d\tau \tag{A.92}$$

---

[3]The response to the perturbation is not before it has been turned on.

Using $U_0(t)|n\rangle = e^{iH_0 t}|n\rangle = e^{iE_n t}|n\rangle$ gives

$$\chi_{AB}(\omega) = i\int_0^\infty \sum_{m,n} \left(f_m - f_n\right)\langle m|e^{-iE_m t}Ae^{iE_n t}|n\rangle\langle n|e^{-iE_n t'}Be^{iE_m t'}|m\rangle e^{-i(\omega+i\eta)\tau}d\tau$$

$$\text{(A.93)}$$

$$= i\int_0^\infty \sum_{m,n} \left(f_m - f_n\right)\langle m|A|n\rangle\langle n|B|m\rangle e^{-i(\omega+E_m-E_n+i\eta)\tau}d\tau \tag{A.94}$$

$$= i\sum_{m,n} \frac{e^{-i(\omega+E_m-E_n+i\eta)\tau}}{-i(\omega+E_m-E_n+i\eta)}\Bigg|_{\tau=0}^{\tau=\infty} \left(f_m - f_n\right)\langle m|A|n\rangle\langle n|B|m\rangle \tag{A.95}$$

Finally we have

> **Fourier-transform of the Correlation Function**
>
> $$\chi_{AB}(\omega) = \lim_{\eta\to 0^+} \sum_{m,n} \frac{f_m - f_n}{\omega + E_m - E_n + i\eta}\langle m|A|n\rangle\langle n|B|m\rangle \tag{A.96}$$

A.4. Hartree potentials for 1D in 3D

The scalar Hartree potential is given in Equ. 6.60 which can be written as

$$V_H(x, y) = \int n(x') G_H(x, x', y) dx' \tag{A.97}$$

where $G_H(x, x', y) = \frac{2\pi}{k_\parallel} e^{ik_\parallel y} e^{-|k_\parallel| \cdot |x - x'|}$. The effective scalar potential reads

$$V_s(x, y) = V_{ext}(x) + V_H(x, y) + V_{xc}(x) \tag{A.98}$$

The effective vector potential reads

$$\mathbf{A}_s(x, y) = \mathbf{A}_{ext}(x) + \mathbf{A}_H(x, y) + \mathbf{A}_{xc}(x) \tag{A.99}$$

In a first approximation the exchange-correlation part can be neglected. The vector Hartree potential needs a little more work.

$$\mathbf{A}_H(\mathbf{r}, t) = \frac{1}{c} \int \frac{\mathbf{J}_T(\mathbf{r}', t_r)}{|\mathbf{r} - \mathbf{r}'|} d\tau' \tag{A.100}$$

For the transversal current we can use (see A.2)

$$\mathbf{J}_T(\mathbf{r}, t) = \mathbf{J}(\mathbf{r}, t) - \mathbf{J}_L(\mathbf{r}, t) = \mathbf{J}(\mathbf{r}, t) + \frac{i\omega}{4\pi} \nabla_\mathbf{r} V_H(\mathbf{r}, t). \tag{A.101}$$

The gradient of the scalar Hartree potential $V_H(x, y)$ reads

$$\nabla_\mathbf{r} V_H(x, y) = \mathbf{e}_x \left(\partial_x \int n(x') G_H(x, x', y) dx' \right) \tag{A.102}$$

$$+ \mathbf{e}_y \left(\partial_y \int n(x') G_H(x, x', y) dx' \right) \tag{A.103}$$

$$= \mathbf{e}_x \left(-|k_\parallel| \int n(x') \text{sign}(x - x') G_H(x, x', y) dx' \right) \tag{A.104}$$

$$+ \mathbf{e}_y \left(ik_\parallel V_H(x, y) \right) \tag{A.105}$$

where the sign-function has been used. The transversal current is then

$$\mathbf{J}_T(x, y) = \mathbf{J}(x, y) + \frac{i\omega}{4\pi} \int n(x') \mathbf{a}(x, x') G_H(x, x', y) dx' \tag{A.106}$$

where the previously defined $\mathbf{a}(x, x')$ has been used. The vector Hartree potential consequently reads

$$\mathbf{A}_H(x, y, z) = \frac{1}{c} \iint \left[\frac{\mathbf{J}(x', y')}{|(x - x')^2 + (y - y')^2 + (z - z')^2|} \right. \tag{A.107}$$

$$\left. + \frac{i\omega}{4\pi} \int \frac{n(x'') \mathbf{a}(x', x'') G_H(x', x'', y')}{|(x - x')^2 + (y - y')^2 + (z - z')^2|} dx'' \right] dx' dy' dz'. \tag{A.108}$$

Applying cylindrical coordinate substitution $y' - y = \rho \cos(\phi)$ and $z' - z = \rho \sin(\phi)$ results

$$\mathbf{A}_H(x, y) = \frac{1}{c} e^{ik_\parallel y} \int \int_{\rho=0}^\infty \int_{\phi=0}^{2\pi} \left[\frac{\mathbf{J}(x') e^{ik_\parallel \rho \cos(\phi)}}{|(x - x')^2 + \rho^2|} \right. \tag{A.109}$$

$$\left. + \frac{i\omega}{4\pi} \int \frac{n(x'') 2\pi \mathbf{a}(x', x'') e^{ik_\parallel y'} e^{-k_\parallel |x' - x''|}}{|k_{\parallel\parallel}|(x - x')^2 + \rho^2|} dx'' \right] dx' \rho d\rho d\phi \tag{A.110}$$

$$= \frac{1}{c} e^{ik_\parallel y} \int \int_{\rho=0}^\infty \int_{\phi=0}^{2\pi} \left[\frac{\mathbf{J}(x') e^{ik_\parallel \rho \cos(\phi)}}{|(x - x')^2 + \rho^2|} \right. \tag{A.111}$$

$$\left. + \frac{i\omega}{4\pi} \int \frac{n(x'') 2\pi \mathbf{a}(x', x'') e^{ik_\parallel \rho \cos(\phi)} e^{-k_\parallel |x' - x''|}}{|k_\parallel| \cdot |(x - x')^2 + \rho^2|} dx'' \right] dx' \rho d\rho d\phi \tag{A.112}$$

A. Appendix

By using the Bessel function of first kind J_0 [86] one gets

$$\mathbf{A}_H(x,y) = \frac{1}{c} e^{ik_{\|}y} \int \int_{\rho=0}^{\infty} 2\pi J_0(k_{\|}\rho) \Big[\frac{\mathbf{J}(x')}{|(x-x')^2 + \rho^2|} \tag{A.113}$$

$$+ \frac{i\omega}{4\pi} \int \frac{n(x'')2\pi\mathbf{a}(x',x'')e^{-k_{\|}|x'-x''|}}{|k_{\|}| \cdot |(x-x')^2 + \rho^2|} dx'' \Big] dx' \rho d\rho. \tag{A.114}$$

The integration over ρ (by substituting $u = k_{\|}\rho$) results in

$$\mathbf{A}_H(x,y) = \frac{1}{c} e^{ik_{\|}y} \frac{2\pi}{|k_{\|}|} \int e^{-|k_{\|}(x-x')|} \Big[\mathbf{J}(x') + \frac{i\omega}{4\pi} \frac{2\pi}{|k_{\|}|} \int n(x'')\mathbf{a}(x',x'')e^{-|k_{\|}(x'-x'')|}dx'' \Big] dx'. \tag{A.115}$$

Finally, the vector Hartree potential reads

Vector Hartree potential for a 1D system in 3D

$$\mathbf{A}_H(x,y) = \frac{1}{c} \int \Big[\mathbf{J}(x') + \frac{i\omega}{4\pi} \Big(\int n(x'')\mathbf{a}(x',x'')G_H(x',x'',0)dx'' \Big) \Big] G_H(x,x',y)dx'. \tag{A.116}$$

A.5. Vector Potential of a Transverse Magnetic Wave

A transverse magnetic (TM) plane wave has a magnetic induction pointing perpendicular to the direction of propagation of the electromagnetic wave and perpendicular to the electric field. It is also known as a p-polarized wave. Without loss of generality one can define the coordinate system such that the magnetic induction reads

$$\mathbf{B} = B_0 e^{i(\mathbf{k}\cdot\mathbf{r}-\omega t)} \begin{pmatrix} 0 \\ 1 \\ 0 \end{pmatrix} \tag{A.117}$$

Assuming

$$\mathbf{A} = \mathbf{A}_0 e^{i(\mathbf{k}\cdot\mathbf{r}-\omega t)} \tag{A.118}$$

where $\mathbf{A}_0$ does not depend on $\mathbf{r}$ and

$$\mathbf{k} = \begin{pmatrix} k_\parallel \\ 0 \\ k_\perp \end{pmatrix} = k \begin{pmatrix} \sin\theta_1 \\ 0 \\ \cos\theta_1 \end{pmatrix} \tag{A.119}$$

where $k = |\mathbf{k}| = \frac{\omega}{c}\sqrt{\epsilon\mu}$ and θ_1 is the incident angle [1]. Using Coulomb gauge one has

$$\nabla \cdot \mathbf{A} = 0 \tag{A.120}$$
$$i\mathbf{k} \cdot \mathbf{A} = 0 \tag{A.121}$$
$$k_\parallel A_{0,x} + k_\perp A_{0,z} = 0 \tag{A.122}$$

Further utilizing the connection of the magnetic induction and the vector potential gives

$$\mathbf{B} = \nabla \times \mathbf{A} \tag{A.123}$$
$$= \begin{pmatrix} \partial_y A_z - \partial_z A_y \\ \partial_z A_x - \partial_x A_z \\ \partial_x A_y - \partial_y A_x \end{pmatrix} \tag{A.124}$$
$$= B_0 e^{i(\mathbf{k}\cdot\mathbf{r}-\omega t)} \begin{pmatrix} 0 \\ 1 \\ 0 \end{pmatrix} \tag{A.125}$$

We take a look on the first component $\partial_y A_z - \partial_z A_y = 0$. Since $A_z \propto e^{i(k_\parallel x + k_\perp z - \omega t)}$ does not depend on y one has $\partial_y A_z = 0$ and further $\partial_z A_y = 0$ what states that A_y does not depend on z. Analogously the third component concludes that A_y does not depend on x, hence A_y is constant and consequently $A_{0,y} = 0$. The second component reads

$$\partial_z A_x - \partial_x A_z = B_0 e^{i(\mathbf{k}\cdot\mathbf{r}-\omega t)} \tag{A.126}$$
$$ik_\perp A_{0,x} - ik_\parallel A_{0,z} = B_0 \tag{A.127}$$

Together with Equ. A.122 one has a linear system to determine the components of $\mathbf{A}_0$.

$$k_\parallel A_{0,x} + k_\perp A_{0,z} = 0 \tag{A.128}$$
$$ik_\perp A_{0,x} - ik_\parallel A_{0,z} = B_0 \tag{A.129}$$

by using matrix representation one gets

$$\begin{pmatrix} 0 \\ B_0 \end{pmatrix} = \begin{pmatrix} k_\parallel & k_\perp \\ ik_\perp & -ik_\parallel \end{pmatrix} \begin{pmatrix} A_{0,x} \\ A_{0,z} \end{pmatrix} = \hat{M} \begin{pmatrix} A_{0,x} \\ A_{0,z} \end{pmatrix} \tag{A.130}$$

A. Appendix

The inverse of $\hat{M}$ is

$$\hat{M}^{-1} = \frac{1}{k^2} \begin{pmatrix} k_\parallel & -ik_\perp \\ k_\perp & ik_\parallel \end{pmatrix} \tag{A.131}$$

The x and z components of $\mathbf{A}_0$ reads

$$\begin{pmatrix} A_{0,x} \\ A_{0,z} \end{pmatrix} = \hat{M}^{-1} \begin{pmatrix} 0 \\ B_0 \end{pmatrix} = \frac{iB_0 c}{\omega\sqrt{\epsilon\mu}} \begin{pmatrix} -\cos\theta_1 \\ \sin\theta_1 \end{pmatrix}. \tag{A.132}$$

A.6. Vector Potential of Evanescent Fields

In this appendix section we consider a two-half infinite layer system, e.g. glass layer and air/vacuum layer. The surface boundary between both layers is located at $z = 0$. The glass layer is given at the left side ($z < 0$). Assuming an incident p-polarized plane wave coming from the left side ($z < 0$). Depending on the indicent angle, parts of the wave are reflected and transmitted. We denote the left layer ($z < 0$) as medium 1, and the right layer ($z > 0$) as medium 2. The wave vector of the incident wave in medium 1 reads

$$\mathbf{k}_1 = k_1 \begin{pmatrix} \sin \theta_1 \\ 0 \\ \cos \theta_1 \end{pmatrix} \tag{A.133}$$

where θ_1 is the incident angle (For $\theta_1 = 0$ the incident wave is perpendicular to the layer boundary). The amplitude is given by $k_1 = \frac{\omega}{c} \sqrt{\epsilon_1 \mu_1}$ [1]. Since the incident wave is p-polarized, the magnetic induction points in y-direction only

$$\mathbf{B}_1 = \hat{\mathbf{y}} B_0 e^{i(\mathbf{k_1} \cdot \mathbf{r} - \omega t)} \tag{A.134}$$

Using $\mathbf{k}_1 \times \mathbf{B}_1 = \epsilon_1 k_1 \mathbf{E}_1$ the electric field of the incident wave can be computed

$$\mathbf{E}_1 = \frac{B_0}{\epsilon_1} e^{i(\mathbf{k_1} \cdot \mathbf{r} - \omega t)} \begin{pmatrix} -\cos \theta_1 \\ 0 \\ \sin \theta_1 \end{pmatrix} \tag{A.135}$$

The amplitude of the wave vector in the second medium is given by $k_2 = \frac{\omega}{c} \sqrt{\epsilon_2 \mu_2}$ [1]. The wave vector reads

$$\mathbf{k}_2 = \begin{pmatrix} k_1 \sin \theta_1 \\ 0 \\ k_2 \sqrt{1 - \tilde{n}^2 \sin^2 \theta_1} \end{pmatrix} \tag{A.136}$$

where $\tilde{n} = \frac{\sqrt{\epsilon_1 \mu_1}}{\sqrt{\epsilon_2 \mu_2}}$ and by using $k_{2,z}^2 = k_2^2 - k_{2,x}^2$. The amplitude of the transmitted electric field can be obtained by the usage of the Fresnel coefficients. The electric field in medium 2 reads

$$\mathbf{E}_2 = \frac{B_0}{\epsilon_1} \frac{2\epsilon_2 k_{1z}}{\epsilon_2 k_{1,z} + \epsilon_1 k_{2,z}} e^{i(\mathbf{k_2} \cdot \mathbf{r} - \omega t)} \begin{pmatrix} -\sqrt{1 - \tilde{n}^2 \sin^2 \theta_1} \\ 0 \\ \tilde{n} \sin \theta_1 \end{pmatrix} \tag{A.137}$$

By using $\mathbf{E} = -\frac{\partial}{\partial t} \mathbf{A} - \nabla \phi$ and $\frac{\partial}{\partial t} \mathbf{E}_2 = -i\omega \mathbf{E}_2$ one can write the vector potential in the second medium as

$$\mathbf{A}_2 = \frac{i}{\omega} \mathbf{E}_2. \tag{A.138}$$

In the case that medium 1 is glass (e.g. $\epsilon_1 = 2.25$) and medium 2 is air ($\epsilon_2 = 1$) a critical angle θ_c exists, where for $\theta > \theta_c$ total reflection occurs ($\theta_c = 41.8°$) [1]. For such angles the wavenumber k_2 becomes a negative imaginary number and as a result the wave decays exponentially into the second medium. Such a decaying wave is called **evanescent wave** and it can excite a plasmon polariton in a near located metal layer surface (Otto- or Kretschmann geometry) [1].

A.7. Correlation Functions in 1D

By using Kohn-Sham wavefunctions

$$|n\rangle = e^{i\mathbf{p}\cdot\mathbf{r}}\phi_n(x) \tag{A.139}$$

where $\mathbf{p}$ is the parallel momentum, the Fourier-transform of the correlation function reads

$$\chi_{A,B}(\omega) = \sum_{m,n}\sum_{\mathbf{p},\mathbf{p}'} \frac{f_m - f_n}{\omega + \omega_{mn} + i0^+} \cdot \left(e^{-i\mathbf{p}\cdot\mathbf{r}}\phi_m^*(x)A(\mathbf{r})e^{i\mathbf{p}'\cdot\mathbf{r}}\phi_n(x)\right) \cdot$$

$$\cdot \left(e^{-i\mathbf{p}'\cdot\mathbf{r}'}\phi_n^*(x')B(\mathbf{r}')e^{i\mathbf{p}\cdot\mathbf{r}'}\phi_m(x')\right). \tag{A.140}$$

A useful integral could be

$$\int e^{-ik_\|(y-y')}e^{-i(p-p')(y-y')}d(y-y') = \delta_{p+k_\|-p'} \tag{A.141}$$

The different wavevectors are important for the derivatives (J-operators) but not for the distribution functions and energies.

$$\chi_{A,B,\mathbf{k}_\|}(\omega) = \sum_{m,n}\sum_{\mathbf{p}} \frac{f_m - f_n}{\omega + \omega_{mn} + i0^+} \cdot \left(e^{-i\mathbf{p}\cdot\mathbf{r}}\phi_m^*(x)A(\mathbf{r})e^{i(\mathbf{p}+\mathbf{k}_\|)\cdot\mathbf{r}}\phi_n(x)\right) \cdot$$

$$\cdot \left(e^{-i(\mathbf{p}+\mathbf{k}_\|)\cdot\mathbf{r}'}\phi_n^*(x')B(\mathbf{r}')e^{i\mathbf{p}\cdot\mathbf{r}'}\phi_m(x')\right) \tag{A.142}$$

Current operator: $\mathbf{j} = -\frac{i}{2}\left(\nabla - \nabla^+\right)$, where ∇^+ is the differentiation w.r.t. left hand side. Density operator: $r = \delta(\mathbf{r}-\mathbf{r}')$

$$r_{mn} = \langle p,m|r|p+k_\|,n\rangle \simeq \phi_m^*(x)\phi_n(x) \tag{A.143}$$

$$j_{mn} = \langle p,m|j_x|p+k_\|,n\rangle \simeq -\frac{i}{2}\{\phi_m^*(x)\frac{\partial\phi_n(x)}{\partial x} - \frac{\partial\phi_m^*(x)}{\partial x}\phi_n(x)\}$$

$$\langle p,m|j_y|p+k_\|,n\rangle \simeq -\frac{i}{2}i(p+k_\|+p)r_{mn} = (p+\frac{k_\|}{2})r_{mn}$$

$$\langle p+k_\|,m|j_y|p,n\rangle \simeq -\frac{i}{2}i(p+p+k_\|)r_{mn} = (p+\frac{k_\|}{2})r_{mn} \tag{A.144}$$

For the correlation functions we have

$$\chi_{\rho,\rho} \simeq \sum_{m,n,p} \frac{f_{m,p} - f_{n,p}}{\omega + \omega_{m,n} + i0^+}r_{m,n}(x)r_{n,m}(x') \tag{A.145}$$

$$\chi_{\rho,x} \simeq \sum_{m,n,p} \frac{f_{m,p} - f_{n,p}}{\omega + \omega_{m,n} + i0^+}r_{m,n}(x)j_{n,m}(x') \tag{A.146}$$

$$\chi_{\rho,y} \simeq \frac{k_\|}{2}\chi_{\rho,\rho} \tag{A.147}$$

$$\chi_{x,\rho} \simeq \sum_{m,n,p} \frac{f_{m,p} - f_{n,p}}{\omega + \omega_{m,n} + i0^+}j_{m,n}(x)r_{n,m}(x') = \chi_{\rho,x}^+ \tag{A.148}$$

$$\chi_{y,\rho} \simeq \frac{k_\|}{2}\chi_{\rho,\rho} \tag{A.149}$$

$$\chi_{x,x} \simeq \sum_{m,n,p} \frac{f_{m,p} - f_{n,p}}{\omega + \omega_{m,n} + i0^+}j_{m,n}(x)j_{n,m}(x') \tag{A.150}$$

$$\chi_{x,y} \simeq \frac{k_\|}{2}\chi_{x,\rho} = \frac{k_\|}{2}\chi_{\rho,x}^+ \tag{A.151}$$

$$\chi_{y,x} \simeq \frac{k_\|}{2}\chi_{\rho,x} = \frac{k_\|}{2}\chi_{x,\rho}^+ \tag{A.152}$$

$$\chi_{y,y} \simeq \frac{k_\|^2}{4}\chi_{\rho,\rho} + \sum_{m,n,p} \frac{f_{m,p} - f_{n,p}}{\omega + \omega_{m,n} + i0^+}r_{m,n}(x)r_{n,m}(x')p^2 \tag{A.153}$$

To the lowest order of approximation we only keep $\chi_{\rho,\rho}, \chi_{\rho,x}, \chi_{x,\rho}, \chi_{x,x}$ with $k_{\parallel} \ll 1$ in atomic units.

Applying this approximation onto matrix equation Equ. 6.29, one yields the simplified matrix equation

$$\begin{pmatrix} m_{11} & m_{12} \\ m_{21} & m_{22} \end{pmatrix} \cdot \begin{pmatrix} \delta V_s \\ \delta A_{s,x} \end{pmatrix} = \begin{pmatrix} \delta V_{ext} \\ \delta A_{ext,x} \end{pmatrix} \tag{A.154}$$

where for x one can substitute any other direction.

A.8. Polarization Function

$$P(\mathbf{r}, \mathbf{r}', \tau) = -i\Theta(\tau)\langle[n(\mathbf{r}, \tau), n(\mathbf{r}', \tau)]\rangle \tag{A.155}$$

For a homogeneous electron gas the polarization function depends on relative spatial coordinates.

$$P(\mathbf{r}, \mathbf{r}', \tau) \longmapsto P(\mathbf{r} - \mathbf{r}', \tau) \tag{A.156}$$

The Fourier-transformed polarization function reads

$$P_{\mathbf{q}, \mathbf{q}'}(\tau) = \int e^{-i(\mathbf{q}\cdot\mathbf{r} - \mathbf{q}'\cdot\mathbf{r}')} P(\mathbf{r} - \mathbf{r}', \tau) d^3r d^3r' =$$

$$= \underbrace{\int e^{-i(\mathbf{q} - \mathbf{q}')\cdot\mathbf{R}} d^3R}_{\delta_{\mathbf{q}, \mathbf{q}'}} \int e^{-i(\mathbf{q} + \mathbf{q}')\cdot\frac{\mathbf{D}}{2}} P(\mathbf{D}, \tau) d^3D$$

$$= \int e^{-i\mathbf{q}\cdot\mathbf{D}} P(\mathbf{D}, \tau) d^3D$$

$$P_{\mathbf{q}}(\tau) = \int e^{-i\mathbf{q}\cdot\mathbf{D}} P(\mathbf{D}, \tau) d^3D \tag{A.157}$$

where a coordinate transformation with a center of mass coordinate $\mathbf{R} = \frac{1}{2}(\mathbf{r} + \mathbf{r}')$ and a relative coordinate $\mathbf{D} = \mathbf{r} - \mathbf{r}'$ has been used.

$$P(x, x', \tau) = -i\Theta(\tau) \int P(\mathbf{r}, \mathbf{r}', \tau) d^2r_\| d^2r_\|'$$

$$= -i\Theta(\tau) \int d^2r_\| d^2r_\|' \sum_{\mathbf{q}} e^{i\mathbf{q}\cdot(\mathbf{r} - \mathbf{r}')} P_{\mathbf{q}}(\tau)$$

$$= -i\Theta(\tau) \sum_{q_x} e^{iq_x\cdot(x - x')} P_{\mathbf{q}}(\tau) \tag{A.158}$$

$$P(x - x', \tau) = -i\Theta(\tau) \int e^{iq\cdot(x - x')} P_{\mathbf{q}}(\tau) \frac{dq}{2\pi} \tag{A.159}$$

The static polarization function is given by

$$P(q, 0) = \frac{k_F}{2\pi^2}\left\{ -1 + \frac{1}{q}\left(1 - \frac{q^2}{4}\right)\ln\left(\left|\frac{1 - \frac{q}{2}}{1 + \frac{q}{2}}\right|\right) \right\} \tag{A.160}$$

where q is in units of k_F.

$$P(x, \tau) = -i\Theta(\tau) \int e^{iqx} P_q(\tau) \frac{dq}{2\pi}$$

$$= -i\Theta(\tau) k_F \int e^{i\tilde{q}k_F x} P_{\tilde{q}k_F}(\tau) \frac{d\tilde{q}}{2\pi} \tag{A.161}$$

where $\tilde{q} = k_F q$ and hence $d\tilde{q} = k_F dq$.

Bibliography

[1] L. Novotny and B. Hecht. *Principles of Nano-Optics*. Cambridge University Press, 2006.

[2] S. A. Maier. *Plasmonics: Fundamentals and Applications*. Springer, 2007.

[3] Franz Aussenegg and Harald Ditlbacher. Plasmonen als lichttransporter: Nanooptik. *Physik in unserer Zeit*, 37(5):220–226, 2006.

[4] Andreas Trügler. *Optical Properties of Metallic Nanoparticles: Basic Principles and Simulation*. Springer International Publishing, 2016.

[5] Ekmel Ozbay. Plasmonics: Merging photonics and electronics at nanoscale dimensions. *Science*, 311(5758):189–193, 2006.

[6] Kevin J. Savage, Matthew M. Hawkeye, Ruben Esteban, Andrei G. Borisov, Javier Aizpurua, and Jeremy J. Baumberg. Revealing the quantum regime in tunnelling plasmonics. *Nature*, 491(7425):577, 2012.

[7] C. Ciracì, R. T. Hill, J. J. Mock, Y. Urzhumov, A. I. Fernández-Domínguez, S. A. Maier, J. B. Pendry, A. Chilkoti, and D. R. Smith. Probing the Ultimate Limits of Plasmonic Enhancement. *Science*, 337(6098):1072–1074, 2012.

[8] Jonathan A. Scholl, Aitzol García-Etxarri, Ai Leen Koh, and Jennifer A. Dionne. Observation of Quantum Tunneling between Two Plasmonic Nanoparticles. *Nano Letters*, 13(2):564–569, 2013. PMID: 23245286.

[9] Shu Fen Tan, Lin Wu, Joel K.W. Yang, Ping Bai, Michel Bosman, and Christian A. Nijhuis. Quantum Plasmon Resonances Controlled by Molecular Tunnel Junctions. *Science*, 343(6178):1496–1499, 2014.

[10] Pieter G. Kik and Mark L. Brongersma. *Surface Plasmon Nanophotonics*, chapter SURFACE PLASMON NANOPHOTONICS, pages 1–9. Springer Netherlands, Dordrecht, 2007.

[11] R W Wood. On a remarkable case of uneven distribution of light in a diffraction grating spectrum. *Proceedings of the Physical Society of London*, 18(1):269, 1902.

[12] J. C. Maxwell Garnett. Colours in metal glasses and in metallic films. *Philosophical Transactions of the Royal Society of London A: Mathematical, Physical and Engineering Sciences*, 203(359-371):385–420, 1904.

[13] Gustav Mie. Beiträge zur optik trüber medien, speziell kolloidaler metallösungen. *Annalen der Physik*, 330(3):377–445, 1908.

[14] David Pines. Collective energy losses in solids. *Rev. Mod. Phys.*, 28:184–198, Jul 1956.

[15] R. H. Ritchie. Plasma losses by fast electrons in thin films. *Phys. Rev.*, 106:874–881, Jun 1957.

[16] R. H. Ritchie, E. T. Arakawa, J. J. Cowan, and R. N. Hamm. Surface-plasmon resonance effect in grating diffraction. *Phys. Rev. Lett.*, 21:1530–1533, Nov 1968.

[17] Andreas Otto. Excitation of nonradiative surface plasma waves in silver by the method of frustrated total reflection. *Zeitschrift für Physik*, 216(4):398–410, 1968.

[18] E Kretschmann and H Raether. Radiative decay of non radiative surface plasmons excited by light. *Zeitschrift Naturforschung Teil A*, 23:2135–2136, 1968.

[19] Uwe Kreibig and Peter Zacharias. Surface plasma resonances in small spherical silver and gold particles. *Zeitschrift für Physik*, 231(2):128–143, 1970.

[20] S. L. Cunningham, A. A. Maradudin, and R. F. Wallis. Effect of a charge layer on the surface-plasmon-polariton dispersion curve. *Phys. Rev. B*, 10:3342–3355, Oct 1974.

[21] M. Fleischmann, P.J. Hendra, and A.J. McQuillan. Raman spectra of pyridine adsorbed at a silver electrode. *Chemical Physics Letters*, 26(2):163 – 166, 1974.

[22] Junichi Takahara, Suguru Yamagishi, Hiroaki Taki, Akihiro Morimoto, and Tetsuro Kobayashi. Guiding of a one-dimensional optical beam with nanometer diameter. *Opt. Lett.*, 22(7):475–477, Apr 1997.

[23] T. W. Ebbesen, H. J. Lezec, H. F. Ghaemi, T. Thio, and P. A. Wolff. Extraordinary optical transmission through sub-wavelength hole arrays. *Nature*, 391(6668):667–669, Feb 1998.

[24] J. B. Pendry. Negative refraction makes a perfect lens. *Phys. Rev. Lett.*, 85:3966–3969, Oct 2000.

[25] Wenqi Zhu, Ruben Esteban, Andrei G. Borisov, Jeremy J. Baumberg, Peter Nordlander, Henri J. Lezec, Javier Aizpurua, and Kenneth B. Crozier. Quantum mechanical effects in plasmonic structures with subnanometre gaps. 7:11495 EP –, Jun 2016. Review Article.

[26] *Trustees of the British Museum.*

[27] Harry A. Atwater. The Promise of Plasmonics. *SIGDA Newsl.*, 37(9):1:1–1:1, May 2007.

[28] Lewi Tonks and Irving Langmuir. Oscillations in ionized gases. *Phys. Rev.*, 33:195–210, Feb 1929.

[29] Jiří Homola. *Surface Plasmon Resonance Based Sensors*, volume 4 of *Springer Series on Chemical Sensors and Biosensors*. Springer Berlin Heidelberg, 2006.

[30] C. J. Powell and J. B. Swan. Origin of the characteristic electron energy losses in aluminum. *Phys. Rev.*, 115:869–875, Aug 1959.

[31] George Green. *An Essay on the Application of mathematical Analysis to the theories of Electricity and Magnetism*. Nottingham, July 1828.

[32] John David Jackson. *Classical electrodynamics*. Wiley, New York, NY, 3rd ed. edition, 1999.

[33] Ulrich Hohenester and Joachim Krenn. Surface plasmon resonances of single and coupled metallic nanoparticles: A boundary integral method approach. *Phys. Rev. B*, 72:195429, Nov 2005.

[34] F. J. García de Abajo and J. Aizpurua. Numerical simulation of electron energy loss near inhomogeneous dielectrics. *Phys. Rev. B*, 56:15873–15884, Dec 1997.

[35] F. J. García de Abajo and A. Howie. Retarded field calculation of electron energy loss in inhomogeneous dielectrics. *Phys. Rev. B*, 65:115418, Mar 2002.

[36] F. J. García de Abajo. Optical excitations in electron microscopy. *Rev. Mod. Phys.*, 82:209–275, Feb 2010.

[37] M. Born and E. Wolf. *Principles of Optics: Electromagnetic Theory of Propagation, Interference and Diffraction of Light*. Pergamon Press, 1964.

[38] Max Born and Emil Wolf. *Principles of Optics: Electromagnetic Theory of Propagation, Interference and Diffraction of Light (7th Edition)*. Cambridge University Press, 7th edition, 1999.

[39] P. Drude. Zur elektronentheorie der metalle. *Annalen der Physik*, 306(3):566–613, 1900.

[40] A. Sommerfeld and H. Bethe. *Elektronentheorie der Metalle*, pages 333–622. Springer Berlin Heidelberg, Berlin, Heidelberg, 1933.

[41] N.W. Ashcroft and N.D. Mermin. *Solid State Physics*. Saunders College, Philadelphia, 1976.

[42] P. B. Johnson and R. W. Christy. Optical Constants of the Noble Metals. *Phys. Rev. B*, 6:4370–4379, Dec 1972.

[43] Jonathan A. Scholl, Ai Leen Koh, and Jennifer A. Dionne. Quantum plasmon resonances of individual metallic nanoparticles. *Nature*, 483(7390):421–427, Mar 2012.

[44] Ruben Esteban, Andrei G. Borisov, Peter Nordlander, and Javier Aizpurua. Bridging quantum and classical plasmonics with a quantum-corrected model. *Nat. Commun.*, 3:825, 2012.

[45] Peng Zhang. Scaling for quantum tunneling current in nano- and subnano-scale plasmonic junctions. *Sci Rep*, 5:9826, 2015. 25988951[pmid].

[46] Ulrich Hohenester. Quantum corrected model for plasmonic nanoparticles: A boundary element method implementation. *Phys. Rev. B*, 91:205436, May 2015.

[47] Ruben Esteban, Asier Zugarramurdi, Pu Zhang, Peter Nordlander, Francisco J. Garcia-Vidal, Andrei G. Borisov, and Javier Aizpurua. A classical treatment of optical tunneling in plasmonic gaps: extending the quantum corrected model to practical situations. *Faraday Discuss.*, 178:151–183, 2015.

[48] Ulrich Hohenester and Claudia Draxl. Ab initio approach for gap plasmonics. *Phys. Rev. B*, 94:165418, Oct 2016.

[49] Ulrich Hohenester and Andreas Trügler. MNPBEM – A Matlab toolbox for the simulation of plasmonic nanoparticles. *Computer Physics Communications*, 183(2):370 – 381, 2012.

[50] Ulrich Hohenester. Simulating electron energy loss spectroscopy with the MNPBEM toolbox. *Computer Physics Communications*, 185(3):1177 – 1187, 2014.

[51] Jürgen Waxenegger, Andreas Trügler, and Ulrich Hohenester. Plasmonics simulations with the MNPBEM toolbox: Consideration of substrates and layer structures. *Computer Physics Communications*, 193:138 – 150, 2015.

[52] Franz P. Schmidt, Harald Ditlbacher, Ferdinand Hofer, Joachim R. Krenn, and Ulrich Hohenester. Morphing a plasmonic nanodisk into a nanotriangle. *Nano Letters*, 14(8):4810–4815, 2014. PMID: 25000389.

[53] Ulrich Hohenester, Harald Ditlbacher, and Joachim R. Krenn. Electron-energy-loss spectra of plasmonic nanoparticles. *Phys. Rev. Lett.*, 103:106801, Aug 2009.

[54] Dario Knebl, Anton Hörl, Andreas Trügler, Johannes Kern, Joachim R. Krenn, Peter Puschnig, and Ulrich Hohenester. Gap plasmonics of silver nanocube dimers. *Phys. Rev. B*, 93:081405, Feb 2016.

[55] Leif J. Sherry, Shih-Hui Chang, George C. Schatz, Richard P. Van Duyne, Benjamin J. Wiley, and Younan Xia. Localized surface plasmon resonance spectroscopy of single silver nanocubes. *Nano Letters*, 5(10):2034–2038, Oct 2005.

[56] Olivia Nicoletti, Francisco de la Pena, Rowan K. Leary, Daniel J. Holland, Caterina Ducati, and Paul A. Midgley. Three-dimensional imaging of localized surface plasmon resonances of metal nanoparticles. *Nature*, 502(7469):80–84, Oct 2013. Letter.

[57] Justin A. Bordley, Nasrin Hooshmand, and Mostafa A. El-Sayed. The coupling between gold or silver nanocubes in their homo-dimers: A new coupling mechanism at short separation distances. *Nano Letters*, 15(5):3391–3397, May 2015.

[58] H. Raether. *Surface plasmons on smooth and rough surfaces and on gratings*. Number v. 111 in Springer tracts in modern physics. Springer, 1988.

[59] M. Born and R. Oppenheimer. Zur Quantentheorie der Molekeln. *Annalen der Physik*, 389:457–484, 1927.

[60] E. Schrödinger. An Undulatory Theory of the Mechanics of Atoms and Molecules. *Physical Review*, 28:1049–1070, December 1926.

[61] Hans Albrecht Bethe and Roman W. Jackiw. *Intermediate Quantum Mechanics*. Lecture Notes and Supplements in Physics. Benjamin Cummings Publishing Company, Inc., Menlo Park, third edition, 1986.

[62] C. Fiolhais, F. Nogueira, and M. Marques. *A Primer in density functional theory*. Springer, Berlin [etc.], 2003.

[63] P. Hohenberg and W. Kohn. Inhomogeneous Electron Gas. *Phys. Rev.*, 136:B864–B871, Nov 1964.

[64] Mel Levy. Universal variational functionals of electron densities, first-order density matrices, and natural spin-orbitals and solution of the v-representability problem. *Proceedings of the National Academy of Sciences*, 76(12):6062–6065, 1979.

[65] W. Kohn and L. J. Sham. Self-Consistent Equations Including Exchange and Correlation Effects. *Phys. Rev.*, 140:A1133–A1138, Nov 1965.

[66] U von Barth and L Hedin. A local exchange-correlation potential for the spin polarized case. i. *Journal of Physics C: Solid State Physics*, 5(13):1629, 1972.

[67] S. H. Vosko, L. Wilk, and M. Nusair. Accurate spin-dependent electron liquid correlation energies for local spin density calculations: a critical analysis. *Canadian Journal of Physics*, 58(8):1200–1211, 1980.

[68] J. P. Perdew and Alex Zunger. Self-interaction correction to density-functional approximations for many-electron systems. *Phys. Rev. B*, 23:5048–5079, May 1981.

[69] John P. Perdew and Yue Wang. Accurate and simple analytic representation of the electron-gas correlation energy. *Phys. Rev. B*, 45:13244–13249, Jun 1992.

[70] John P. Perdew, Kieron Burke, and Matthias Ernzerhof. Generalized gradient approximation made simple [phys. rev. lett. 77, 3865 (1996)]. *Phys. Rev. Lett.*, 78:1396–1396, Feb 1997.

[71] David C. Langreth and M. J. Mehl. Beyond the local-density approximation in calculations of ground-state electronic properties. *Phys. Rev. B*, 28:1809–1834, Aug 1983.

[72] A. D. Becke. Density functional calculations of molecular bond energies. *The Journal of Chemical Physics*, 84(8):4524–4529, 1986.

[73] Chengteh Lee, Weitao Yang, and Robert G. Parr. Development of the colle-salvetti correlation-energy formula into a functional of the electron density. *Phys. Rev. B*, 37:785–789, Jan 1988.

[74] G. Kresse and J. Hafner. *Ab initio* molecular dynamics for liquid metals. *Phys. Rev. B*, 47:558–561, Jan 1993.

[75] G. Kresse and D. Joubert. From ultrasoft pseudopotentials to the projector augmented-wave method. *Phys. Rev. B*, 59:1758–1775, Jan 1999.

[76] José M Soler, Emilio Artacho, Julian D Gale, Alberto García, Javier Junquera, Pablo Ordejón, and Daniel Sánchez-Portal. The SIESTA method for ab initio order-N materials simulation. *Journal of Physics: Condensed Matter*, 14(11):2745, 2002.

[77] Mads Brandbyge, José-Luis Mozos, Pablo Ordejón, Jeremy Taylor, and Kurt Stokbro. Density-functional method for nonequilibrium electron transport. *Phys. Rev. B*, 65:165401, Mar 2002.

[78] Javier Junquera, Óscar Paz, Daniel Sánchez-Portal, and Emilio Artacho. Numerical atomic orbitals for linear-scaling calculations. *Phys. Rev. B*, 64:235111, Nov 2001.

[79] Georg Heimel, Lorenz Romaner, Jean-Luc Brédas, and Egbert Zojer. Interface Energetics and Level Alignment at Covalent Metal-Molecule Junctions: π-Conjugated Thiols on Gold. *Phys. Rev. Lett.*, 96:196806, May 2006.

[80] Swapan K. Ghosh and Asish K. Dhara. Density-functional theory of many-electron systems subjected to time-dependent electric and magnetic fields. *Phys. Rev. A*, 38:1149–1158, Aug 1988.

[81] Giovanni Vignale. Mapping from current densities to vector potentials in time-dependent current density functional theory. *Phys. Rev. B*, 70:201102, Nov 2004.

[82] P. Romaniello. *Time-Dependent Current-Density-Functional Theory for Metals*. PhD thesis, University of Groningen, 2006.

[83] Ryogo Kubo. Statistical-mechanical theory of irreversible processes. i. general theory and simple applications to magnetic and conduction problems. *Journal of the Physical Society of Japan*, 12(6):570–586, 1957.

[84] R Kubo. The fluctuation-dissipation theorem. *Reports on Progress in Physics*, 29(1):255, 1966.

[85] U. Rössler. *Solid State Theory: An Introduction*. Advanced Texts in Physics. Springer Berlin Heidelberg, 2004.

[86] M. Abramowitz and I. A. Stegun. *Handbook of Mathematical Functions, With Formulas, Graphs, and Mathematical Tables,*. Dover Publications, Incorporated, 1974.

[87] M. Paulsson. Non Equilibrium Green's Functions for Dummies: Introduction to the One Particle NEGF equations. *eprint arXiv:cond-mat/0210519*, October 2002.

[88] Supriyo Datta. *Electronic Transport in Mesoscopic Systems*. Cambridge University Press, 1995. Cambridge Books Online.

Acknowledgement

> My mom says: 'Why aren't you a
> doctor?' and I'm like, 'I am a doctor!'
> and she's all, 'No, I mean a real
> doctor.' She reads my books, but she
> says they give her a headache.
>
> Brian Greene

First of all I gratefully acknowledge my advisor Dr. Ulrich Hohenester for giving me the opportunity of performing a doctoral thesis at University of Graz. Further I want to acknowledge my colleagues and friends at University. Finally, I thank my girlfriend, parents, siblings and friends.